

**FLUTTER INSTABILITY SPEED OF GUIDED SPLINED DISKS, WITH
APPLICATIONS TO SAWING**

by

Ahmad Mohammadpanah

M.Sc, Sharif University of Technology, Iran, 2004

M.A.Sc, The University of British Columbia, Canada, 2012

A THESIS SUBMITTED IN PARTIAL FULFILLMENT OF
THE REQUIREMENTS FOR THE DEGREE OF

DOCTOR OF PHILOSOPHY

in

The Faculty of Graduate and Postdoctoral Studies

(Mechanical Engineering)

THE UNIVERSITY OF BRITISH COLUMBIA

(Vancouver)

February 2015

© Ahmad Mohammadpanah, 2015

Abstract

In this thesis the vibration characteristics of guided splined saws are studied, both analytically and experimentally. Significant insights into the complex dynamic behavior of guided splined saws are presented by analytical investigation of the dynamic behaviour of spinning splined disks and then by conducting idling and cutting experimental tests of guided splined saws. Cutting tests are conducted at different speeds, at critical, supercritical, and post flutter speeds of a guided splined saw. The cutting results are compared to determine the stable operation speeds for guided splined saws.

For the analytical studies, the governing linear equations are derived for the transverse motion of a constant speed spinning splined disk. The disk is subjected to lateral constraints and loads. Rigid body translational and tilting degrees of freedom are included in the analysis of total motion of the spinning disk. Also considered in the analyses are applied conservative in-plane edge loads at the outer and inner boundaries. The numerical solution of these equations is used to investigate the effect of the loads and constraints on the natural frequencies, critical speeds, and stability of the spinning disk. The sensitivity of the eigenvalues of the splined spinning disk to the in-plane edge loads is analyzed by taking the derivative of the spinning disk's eigenvalues with respect to the applied loads. This analysis contains an evaluation of the energy transfer from the applied loads to the disk vibrations and is used to examine the role of critical system components in the development of instability.

Experimental results are presented that support the validity of the analysis. The experimental results indicate that flutter instability occurs at speeds when a backward travelling wave of a mode meets a reflected wave of a different mode. The maximum stable operating speed of the rotating splined disk is defined as the initiation of flutter. Flutter instability speeds of splined saws of various sizes were computed and verified experimentally. Then flutter speed charts of splined saws were developed which provides primary practical guide lines for sawmills to choose optimum blade diameter, eye size, blade thickness, and a stable rotation speed.

Preface

Experimental tests results presented in chapter 4 and 5 are based on the tests conducted at FPInnovations, (Vancouver, B.C., Lumber Manufacturing Laboratory). I was responsible for conducting the idling and cutting tests of guided splined saws under the supervision of Professor Stanley G. Hutton.

Table of Contents

Abstract.....	ii
Preface.....	iii
Table of Contents	iv
List of Tables	vii
List of Figures.....	viii
List of Symbols	xi
Acknowledgements	xii
Dedication	xiii
Chapter 1: Introduction	1
1.1 Background	1
1.2 Mathematical Modeling of the System	3
1.3 Variation of Eigenvalues as a Function of Rotation Speed.....	5
1.4 Literature Review	10
1.5 Objective and Scope.....	19
Chapter 2: Modeling of a Spinning Splined Guided Disk Subjected to In-Plane Edge Loads Applied at the Outer and Inner Boundaries	22
2.1 Introduction	22
2.2 Previous Work on the Effect of Edge Loads on Clamped Disks	22
2.3 Equations of Motion for a Spinning Splined Guided Disk Subjected to In-Plane Outer and Inner Edge Loads.....	26
2.4 Sensitivity Analysis of the Eigenvalues of a Spinning Disk to In-plane Edge Loads .	28
2.4.1 Effect of Radial Load	29

2.4.2 Effect of Tangential Load.....	32
2.5 Numerical Results	33
2.5.1 Effect of In-plane Edge Loads on the Eigenvalues	33
2.5.1.1 Special Case (a Rigid Splined Disk).....	32
2.5.1.2 General Case (A Guided Splined Flexible Disk).....	37
2.5.2 Transverse Response of a Disk to In-plane Edge Loads	42
2.6 Summary	44
Chapter 3: Instability Mechanism of a Spinning Splined Guided Disk Subjected to In-	
plane Edge Loads	46
3.1 Introduction	46
3.2 Work Done by the Edge Loads (Formulation).....	46
3.3 Numerical Results of Energy Induced in the Disk by Edge Loads	49
3.4 Summary	50
Chapter 4: Experimental Investigations of Idling and Cutting Characteristics of a	
Splined Guided Saw	52
4.1 Introduction	52
4.2 Experimental Tests Results	53
4.2.1 Idling Tests	53
4.2.2 Cutting Tests.....	56
4.4 Summary	59
Chapter 5: Flutter Speeds Chart for Guided Splined-Arbor Saws.....	60
5.1 Introduction	60
5.2 Experimental Measurements of Idling Response of Guided Splined-Arbor Saws	62

5.3 Numerical Computation of Eigenvalues of Guided Splined-Arbor Saws.....	66
5.4 Verification of Numerical Results	68
5.5 The Effect of Geometrical Properties of the System on the Start of Flutter Instability Speeds	69
5.6 Flutter Instability Speeds Charts	71
5.7 Conclusion.....	74
Chapter 6: Conclusions	75
6.1 Summary and Conclusion	75
6.2 Suggestions for Further Research	78
References	79
Appendices.....	84
Appendix A: Stresses Fields in a Disk due to Centrifugal Acceleration	84
Appendix B: Mathematical Equations for Rigid Body Tilting and Translational Motions	85
Appendix C: Solution of the Equations of Motion	88
Appendix D: Stresses Fields in a Disk due to In-Plane Edge Loads	90
Appendix E: The Governing Equations of a Rigid Disk, Subjected to In-plane Edge Loads	96
Appendix F: Gullet Feed Index and Feed Speed	98
Appendix G: Derivative of Eigenvalues of Spinning Disk with Respect to In-plane Edge Loads	99
Appendix H: Idling Response of Different Blade Sizes	108
Appendix I: Mathematical Calculation of Non-Dimensional Equation of Motion	112

List of Tables

Table 4.1	Properties of the Blade under Investigation	53
Table 4.2	Cutting Tests Rotation Speed, and Feed Speed	57
Table 5.1	List of Blades under Experimental Investigations	63
Table 5.2	Properties of the disk under Investigation.....	66
Table 5.3	Start of Flutter Instability Speeds for the Blades under Investigations.....	68
Table 5.4	Flutter Speeds for Guided Splined-Arbor Saws.....	72

List of Figures

Figure 1.1 Clamped Saw vs. Guided Splined Circular Saw	2
Figure 1.2 Idealizing the Blade as a Spinning Flat, Thin Disk	3
Figure 1.3 Variation of Imaginary and Real Parts of Eigenvalues, (-- dash lines) A Free Clamped Disk, (- solid lines) Disk is Constrained by a Lateral Spring at the Outer radius	6
Figure 1.4 Variation of Imaginary and Real Parts of Eigenvalues, (-- dash lines) Free Splined Disk, (- solid lines) Splined Guided Disk.....	8
Figure 1.5 Illustrations of Divergence and Flutter Type Instabilities	9
Figure 2.1 Schematic of a Clamped Disk, Subjected to a Conservative In-Plane Compressive Edge Load	23
Figure 2.2 Variations of Eigenvalues as a Function of Rotation Speed, (-- dashed lines) Free Spinning Clamped Disk, (- solid lines) Clamped Disk Subjected to the Edge Load $F=3.5 D/b$	25
Figure 2.3 Schematic of a Splined Disk Subjected to In-Plane Edge Loads, and Their Inner Interaction Loads	26
Figure 2.4 Variation of Natural Frequencies as a Function of Rotation Speed, (-- blue dash lines) Free Spinning Splined Rigid Disk, (- blue solid lines) The Rigid Body Motions are Coupled by a Lateral Spring, (-- red dash lines) Free Spinning Splined Rigid Disk, Subjected to a Radial Load, (- red solid lines) Spinning Splined Rigid Disk, Constrained by a Lateral Spring, Subjected to a Radial Load.....	36
Figure 2.5 Variation of eigenvalues as a Function of Rotation Speed, (--blue dash lines) Free Spinning Splined Disk, (- red solid lines) Free Spinning Splined Disk, Subjected to Edge Loads.....	38

Figure 2.6 Variation of Imaginary Part of Eigenvalues as a Function of Rotation Speed, (--blue dash lines) Free Spinning Guided Splined Disk, (- red solid lines) Free Spinning Guided Splined Disk, Subjected to Edge Loads	40
Figure 2.7 Variation of Real Part of Eigenvalues as a Function of Rotation Speed, (--blue dash lines) Free Spinning Guided Splined Disk, (- red solid lines) Free Spinning Guided Splined Disk, Subjected to Edge Loads	41
Figure 2.8 Transverse Vibration of the Disk Computed for Outer Radius at $\alpha = 45^\circ$, Subjected to (a) A Concentrated Radial In-plane Edge Load (b) A Concentrated Tangential In-plane Edge Load (c) Concentrated Radial and tangential In-plane Edge Load, (blue graph) $\Omega = 42\text{Hz}$, (green graph) $\Omega = 50\text{Hz}$, (red graph) $\Omega = 53\text{Hz}$	43
Figure 3.1 Rate of Work Done by the Edge Loads, at Rotating Speed (a) 42Hz, (b) 50Hz, (c) 53Hz	49
Figure 3.2 Rate of Work Done by the Tangential and Radial Edge Loads, Disk Running at a Flutter Instability Speed ($\Omega = 53\text{Hz}$).....	50
Figure 4.1 Schematic of the Experimental Setup.....	53
Figure 4.2 Variation of Excited Frequencies with Rotation Speed for a Saw Blade with no Constraint.....	55
Figure 4.3 Variations of Excited Frequencies as a Function of Rotation Speed, Guided Spline Saw	55
Figure 4.4 Schematic of Cutting Test Setup	56
Figure 4.5 Cut Profile for Test 1, Cutting at 3200rpm (Critical Speed)	57
Figure 4.6 Cut Profile for Test 2, Cutting at 3600rpm (A Super Critical Speed)	58
Figure 4.7 Cut Profile for Test 3, Cutting at 4000rpm (A Flutter Speed).....	58

Figure 5.1 Experimental Idling Tests Setup.....	62
Figure 5.2 Deflection of Blade 28-8-0.115, during Idling Run-up from 0-3600rpm, Measured by Displacement Probe	64
Figure 5.3 Variation of Excited Frequencies of the Disk as a Function of Rotation Speed ..	65
Figure 5.4 Imaginary and Real Parts of Eigenvalues of the Guided Splined Disk	67
Figure 5.5 Non-Dimensionalized Flutter Speeds for a=3in (Eye#3) and a=4in (Eye#4)	70
Figure 5.6 Flutter Instability Speeds Charts, Eye#3	73
Figure 5.7 Flutter Instability Speeds Charts, Eye#4	73

List of Symbols

a	Inner radius of the disk
b	Outer radius of the disk
D	Disk rigidity ($Eh^3/12(1 - \nu^2)$)
E	Young's Modulus
h	Disk thickness
k	Stiffness of the spring
m	Number of nodal diameters
n	Number of nodal circles
(r, θ, z)	Space-fixed polar coordinate system
λ_{mn}	Eigenvalues for the transverse displacement of the disk
Φ_{mn}	Eigenfunction
R_{mn}	Mode shape in the radial direction for the disk deflection
S_{mn}, C_{mn}	Equilibrium solutions for the amplitude of the <i>sin</i> and <i>cos</i> waves
t	Time
w	Transverse displacement
δ_{ij}	Kronecker delta
ν	Poisson's ratio
ρ	Mass density
$\sigma_{rr}, \sigma_{\theta\theta}$	Radial and hoop stress due to rotation
σ_r, σ_θ	Radial and hoop stress due to in-plane edge loads
Ω	Rotation speed (rad/sec)

Acknowledgements

I am deeply thankful to my supervisor, Professor Stanley Hutton. I have appreciated his support, guidance and advice during my research. I also would like to thank Professor Mohamed Gadala who has provided me with significant help during my studies.

I am thankful to Professor Gary Schajer, Dr. Bruce Lehmann, and Dr. Srikantha Phani for all the great discussions on the subject we have had.

I would also like to record my gratitude to Mr. John White, from FPInnovations, for his assistance during all the experimental tests.

I am deeply indebted to my wife. Her unlimited love, patience and support have made this work possible.

Dedication

To My Lovely Wife

Chapter 1: Introduction

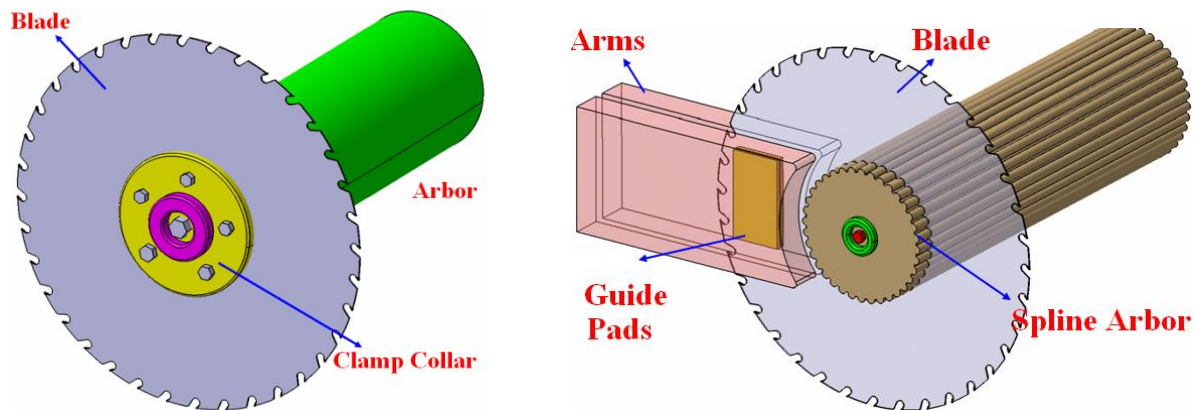
1.1. Background

Spinning disks are essential parts of many machines, and find applications in grinding wheels, turbine rotors, brake systems, fans, computer disks memory units, wafer slicing cutters, and circular saw blades.

In the wood processing industry circular saws are widely used in the breakdown of logs into boards of varying dimensions. The saws are primarily of two types: a) collared saws; and b) splined arbor saws. It has been found in practice that saws which are not constrained laterally at the inner radius interface, known as “Guided Splined Saws”, provide superior cutting performance to “clamped Saws”, where the saw is clamped to the arbor (Figure 1). The maximum cutting speed for a collared saw coincides with the lowest critical speed of the rotating disk whereas the splined saw is able to operate at speeds in excess of the lowest critical speed.

In splined guided saws, the saw fits loosely on a splined arbor and this arbor provides the driving force to the blade. The clearance between the splined arbour and the matching splined of the disk is in order of $0.25 - 0.5\text{mm}$. The lateral location of the blade is determined by the position of guide pads which are supported independently of the blade by two guide arms that are fixed to the saw frame. The clearance between the blade and the guides is in order of $0.05 - 0.1\text{mm}$. In practice this gap is filled with pressurized water.

Figure 1.1 Clamped Saw vs. Guided Splined Circular Saw



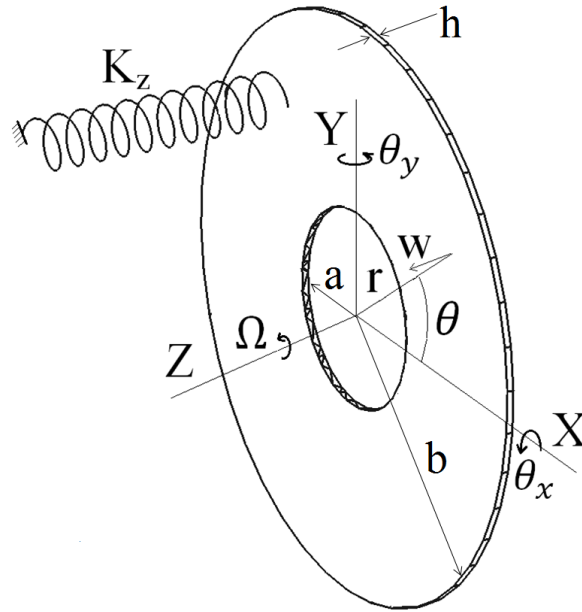
The number of variables that affect cutting performance at high speeds is large and their interaction is complex. Such factors include: blade speed, blade geometry, tooth geometry, blade flatness, depth of cut, wood characteristics, guide size and location, and temperature distribution in the blade. Blade speed is one of the primary factors. At high blade speeds vibrational instability can exist in the saw that leads to poor cutting accuracy. Saw blade vibration directly contributes to production problems such as poor cutting accuracy, and excessive raw material waste. The focus of the current study is on the vibration characteristics of guided splined disks with application to wood sawing.

Present understanding is that the critical speed defines the maximum speed at which a circular saw can be run. Experience at sawmills shows that the maximum operation speed for a clamped saw is the lowest critical speed whereas the splined saw is able to operate at speeds in excess of the lowest critical speed. It opens the question of “what is the maximum stable operation speed for a guided splined saw?”

1.2. Mathematical Modeling of the System

The first step in investigating the vibration characteristics of the system is to set up a mathematical model that captures the essential physics of the problem. In this regard, the blade is idealized as a flat, thin, circular plate. If there is a lateral constraint, it is modeled as a linear spring. Figure 1.2 shows the idealized representation of a splined guided disk. The transverse displacement of the disk is w , measured with respect to stationary coordinates (r, θ) . The rigid body modes of the disk are defined by Z , θ_x and θ_y . The lateral constraints (guides in splined saws) are represented by several linear springs of stiffness k_z located at (r_k, θ_k) .

Figure 1.2 Idealizing the Blade as a Spinning Flat, Thin Disk



The governing equation of motion for a disk, in terms of the transverse displacement w , with respect to a stationary coordinates $w(r, \theta)$, without considering any rigid body motion, is [1]:

$$\rho h (w_{,tt} + 2\Omega w_{,t\theta} + \Omega^2 w_{,\theta\theta}) + D \nabla^4 w - \frac{h}{r} (\sigma_{rr} r w_{,r})_{,r} - \frac{h}{r^2} \sigma_{\theta\theta} w_{,\theta\theta} = 0 \quad (1.1)$$

h, ρ, Ω, D, E and ν are thickness, mass density, rotating speed, flexural rigidity, Young's modulus and Poisson's ratio. σ_{rr} and $\sigma_{\theta\theta}$ are axisymmetric in-plane stresses due to centrifugal acceleration. The closed form solution of σ_{rr} and $\sigma_{\theta\theta}$ are presented in Appendix A.

Consideration of rigid body motions, a space fixed linear spring k_z and a space fixed lateral force f_z located at (r_f, θ_f) leads to the equation (1.2) [2]:

$$\begin{aligned} \rho h(w_{,tt} + 2\Omega w_{,t\theta} + \Omega^2 w_{,\theta\theta}) + D\nabla^4 w - \frac{h}{r}(\sigma_{rr} r w_{,r})_{,r} - \frac{h}{r^2} \sigma_{\theta\theta} w_{,\theta\theta} + \rho h \ddot{z} \\ + \rho h(r\ddot{\theta}_x \sin \theta - r\ddot{\theta}_y \cos \theta) + \rho h(2\Omega r \cos \theta \dot{\theta}_x + 2\Omega r \sin \theta \dot{\theta}_y) \\ = -\frac{k_z}{r}(w + Z + r_k \sin \theta_k \theta_x - r_k \cos \theta_k \theta_y) + \frac{f_z}{r} \end{aligned} \quad (1.2)$$

The equations governing rigid body tilting are [2]:

$$\rho h I(\ddot{\theta}_x + 2\Omega \dot{\theta}_y) + \int_0^{2\pi} \int_a^b \rho h \sin \theta (w_{,tt} + 2\Omega w_{,t\theta}) r^2 dr d\theta = f_s r_k \sin \theta_k + f_z r_f \sin \theta_f \quad (1.3)$$

$$\rho h I(\ddot{\theta}_y - 2\Omega \dot{\theta}_x) + \int_0^{2\pi} \int_a^b \rho h \cos \theta (w_{,tt} + 2\Omega w_{,t\theta}) r^2 dr d\theta = -f_s r_k \cos \theta_k - f_z r_f \cos \theta_f \quad (1.4)$$

Where $\rho h I$ is the moment of inertia for the disk ($I_x = I_y = \frac{\pi}{4} \rho h (b^4 - a^4) = \rho h I$).

The term $f_s = k_z(w + Z + r_k \sin \theta_k \theta_x - r_k \cos \theta_k \theta_y)$ is the spring force.

And, the rigid body translational equation in Z is:

$$m \ddot{z} + \int_0^{2\pi} \int_a^b \rho h (w_{,tt}) r dr d\theta = -k_z(w + Z + r_k \sin \theta_k \theta_x - r_k \cos \theta_k \theta_y) + f_z \quad (1.5)$$

Whereas $m = \rho h \pi (b^2 - a^2)$ is the total mass of the disk.

For mathematical details see Appendix B.

Equations (1.2-1.5) govern the dynamics motion of a splined spinning disk. Solution of the equations can be obtained by application of the Galerkin method. In this solution method the eigenfunction of the stationary disk problem in the polar coordinate system is used as the approximation functions for the Galerkin method. For mathematical details of the solution see Appendix C.

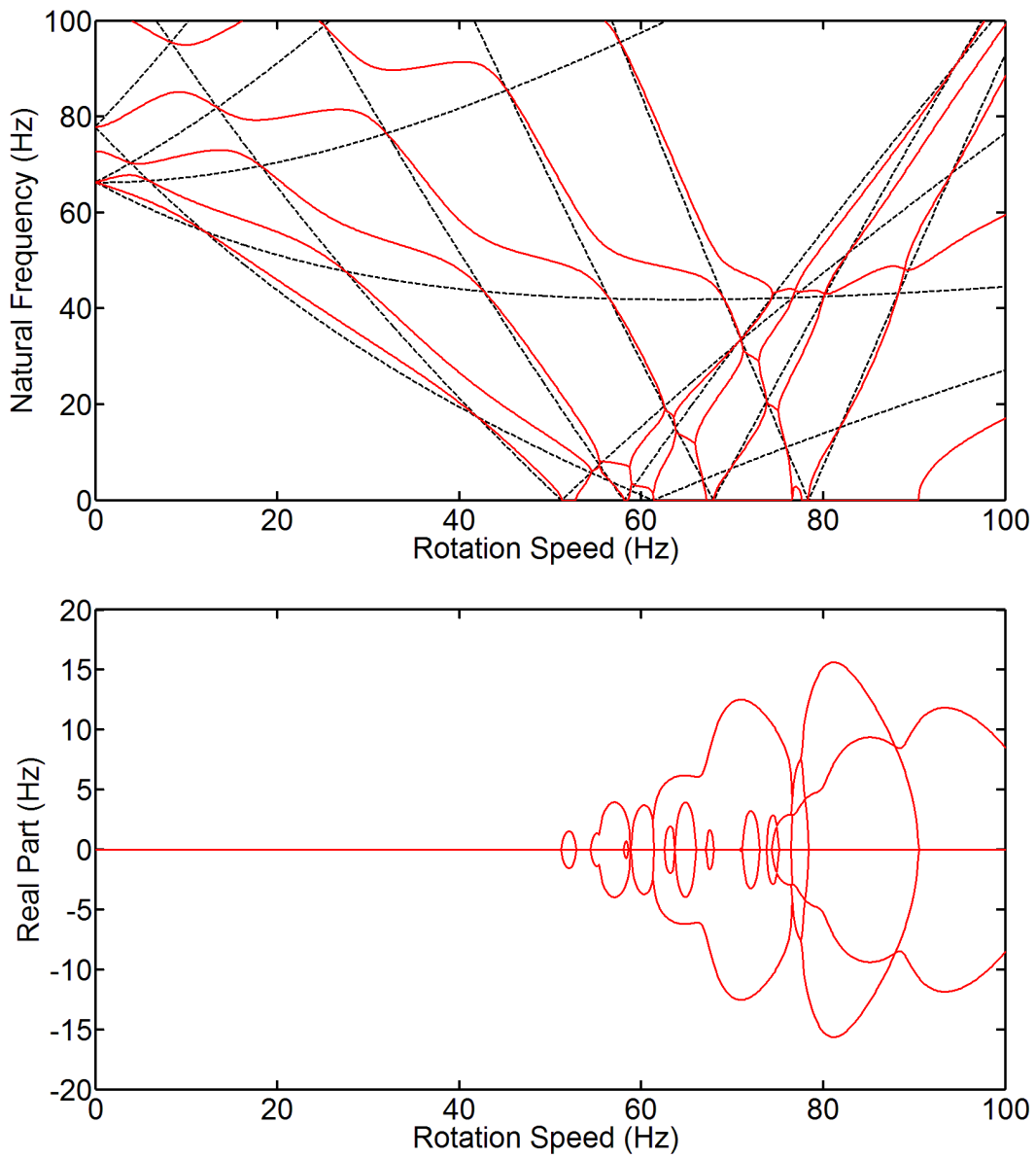
1.3 Variation of Eigenvalues as a Function of Rotation Speed

The variation of eigenvalues as function of rotation speed are computed for a disk with physical properties of inner radius $a = 75\text{mm}$ (3in), outer radius $b = 215\text{mm}$ (8.5in), thickness $h = 1.5\text{mm}$ (0.060in), $E = 2.03 \times 10^{11}\text{pa}$, $\rho = 7800\text{ kg/m}^3$, and $\nu = 0.29$.

In this thesis, the term “Clamped Disk” is defined as a disk with clamped inner radius, and “Splined Disk” as a disk with free inner radius. The term “Guided Splined Disk” refers to a splined disk which is laterally constrained over a certain area by certain number of lateral linear springs of equal stiffness.

Figure 1.3 shows the imaginary and real parts of eigenvalues as a function of rotation speed for a free clamped disk, and a clamped disk subjected to a lateral spring of $k = 10^5 \frac{\text{N}}{\text{m}}$ at outer radius.

Figure 1.3 Variation of Imaginary and Real Parts of Eigenvalues, (--dash lines) A Free Clamped Disk, (- solid lines) Disk is Constrained by a Lateral Spring at the Outer radius

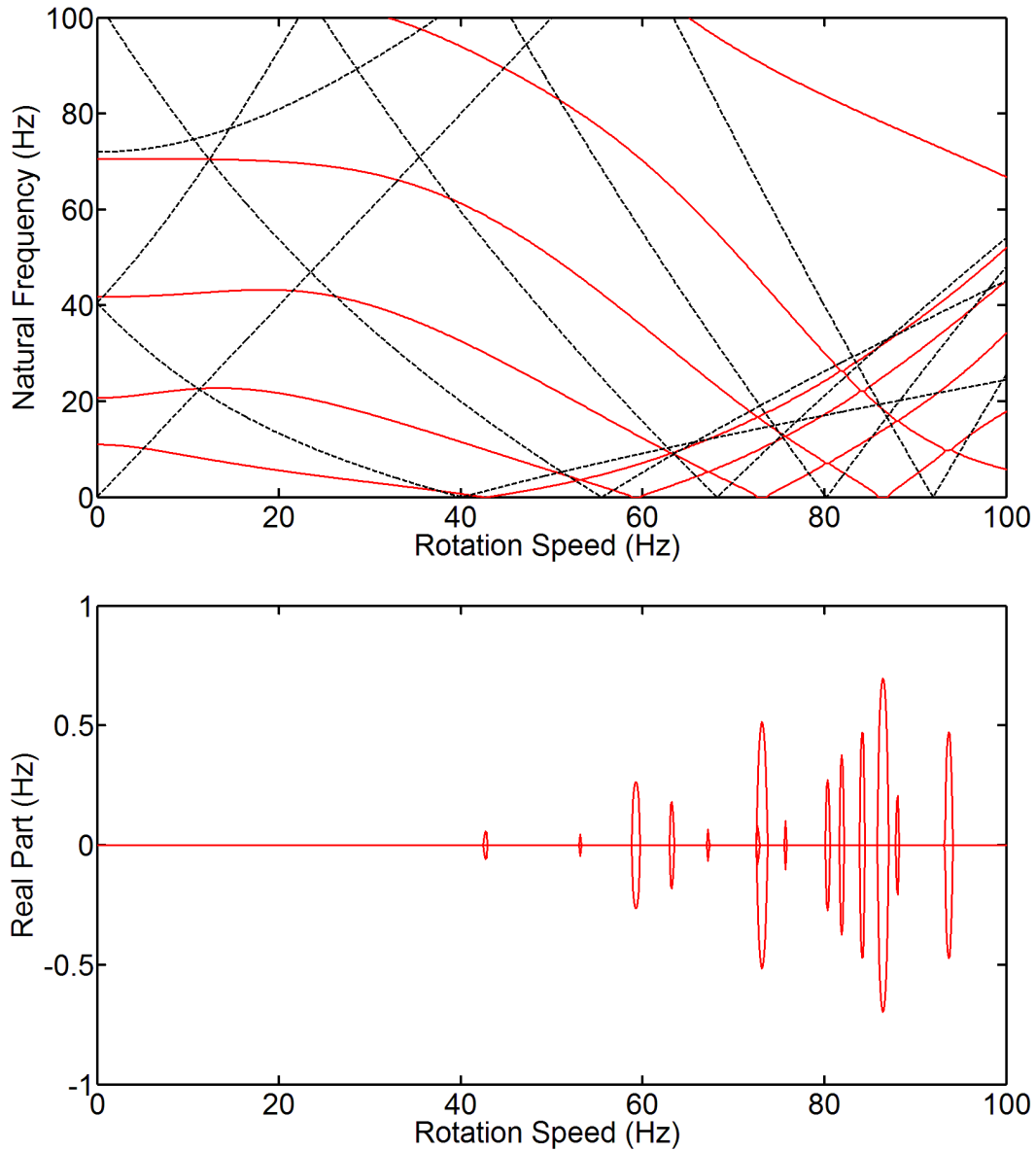


For each mode there are forward and backward waves travelling around the disk. Forward travelling waves travel in the direction of rotation, and backward waves travel in the opposite direction. The natural frequencies of the forward and backward travelling waves of each

mode are the same when the disk is stationary. Once the disk spins the natural frequencies of forward travelling waves increase and the natural frequencies of backward travelling waves decrease. Natural frequencies of the modes having more than one nodal diameter decrease until a speed at which the measured natural frequency is zero. This speed is called a “Critical Speed”. At this speed a constant force can initiate resonance in the disk.

Figure 1.4 shows the imaginary and real parts of eigenvalues as a function of rotation speed for a splined disk. The dash line indicates the eigenvalues for a free splined disk, and solid line indicates the eigenvalues of a guided splined disk, constrained by 16 lateral springs each of stiffness $k = 10^5 \frac{N}{m}$ distributed over a 100×100 mm square area which represents the guides.

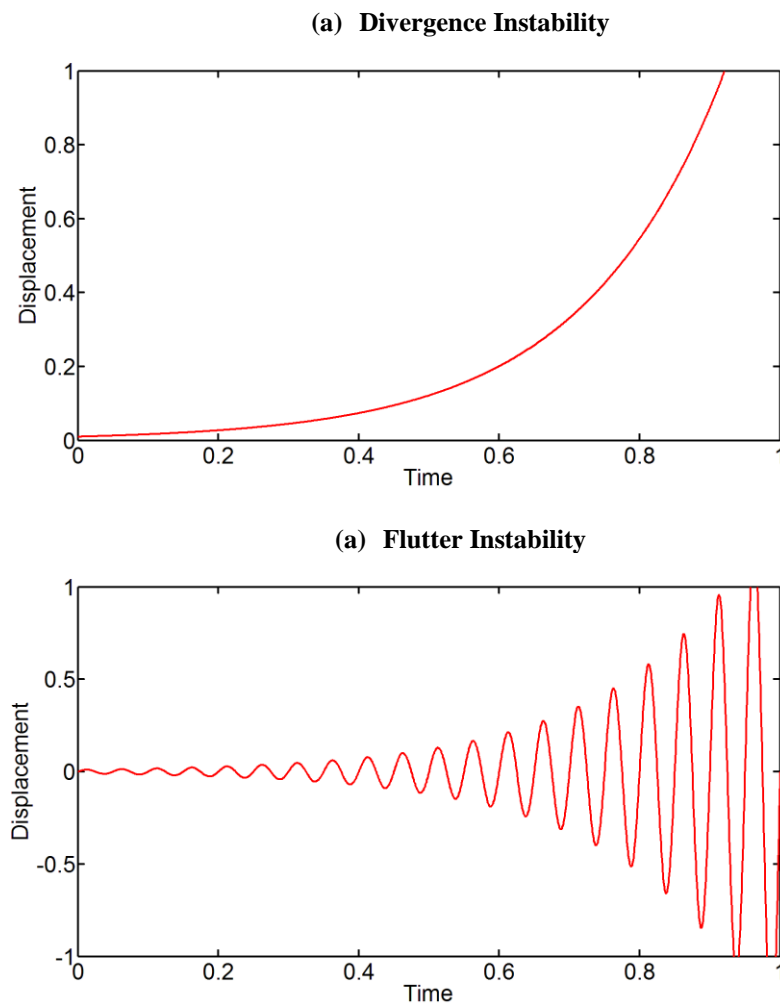
Figure 1.4 Variation of Imaginary and Real Parts of Eigenvalues, (-- dash lines) Free Splined Disk, (- solid lines) Splined Guided Disk



It is noted that with lateral constraints, the movement of the travelling waves become restricted. With the introduction of several springs the curve veering becomes very strong, and the natural frequency curves becomes smoother. Backward and forward travelling wave frequency characteristics are almost completely obliterated.

The introduction of springs leads to instability. The term “Single Mode Resonance”, also known as “Divergence Instability” is defined when the imaginary part of eigenvalues is zero and the real part positive. The term “Merged-mode Resonance”, also known as “Flutter Instability” refers to a case when the imaginary and the real part of eigenvalues are positive. The instability is induced by the presence of springs, and coupling of flexible disk modes. Figure 1.5 illustrates divergence and flutter type instabilities.

Figure 1.5 Illustrations of Divergence and Flutter Type Instabilities



In practice, the maximum operation speed for cutting in a clamped saw coincides with the lowest critical speed of the rotating disk whereas the splined saw is able to operate at speeds in

excess of the lowest critical speed. The questions arise as to “Why conducting cutting at supercritical speed by a splined saw is possible?” and “What is the maximum stable operation speed for a guided splined saw?”

1.4 Literature Review

There exists extensive literature concerning the idling and forced vibration of a spinning disk clamped at the inner radius. The number of studies relating to the dynamics behaviour of splined disks is relatively small; and a large portion of the existing literature relating to the dynamic behaviour of splined disk is concerned with the idling vibration characteristics of spinning disks.

Hutton, Chonan, and Lehmann [1] studied dynamic response characteristics of elastically constrained clamped spinning disks, subjected to excitation produced by fixed point loads. They studied the effect of spring stiffness on the frequency characteristics of the spinning clamped disk. In this study, the frequency-speed plots for different values of spring stiffness were presented. They showed the existence of invariant points on the frequency-speed graphs corresponding to modes having a node at the location of a point guide which was represented by a linear spring. They concluded that the introduction of one or two guides did not significantly change the critical speed characteristics of a spinning clamped disk. It was shown that addition of a guide close to the point of force application will reduce the resulting deflection of the disk at the load point.

Chen and Body [2] investigated the effect of rigid body tilting on the stability and natural frequency characteristics of a head disk, subjected to a rotating load system. They concluded that to an observer attaching to the tilting frame, only the natural frequencies of one nodal diameter

modes increase due to the inertial coupling between the rigid-body tilting and the bending modes, while the natural frequencies of the other modes are not affected. They proved that for a spinning disk with rigid-body tilting freedom the centrifugal force is very important in stabilizing the system. In this study they showed that the system of equations of motion is gyroscopic for a spinning disk with rigid-body tilting freedom.

Chen and Hsu [3] studied the response of a spinning disk under space-fixed couples analytically. They presented vibration and steady state response of the disk and investigated the effects of the rotation speed and external damping. In their investigation the effect of rotating and space fixed damping was considered. They found that before critical speed, both the rotating and space fixed damping suppress the transient response of a spinning disk. But, at super critical speed, the rotating damping suppresses the transient vibration while the space fixed damping destabilizes the disk.

Chen and Wong [4] investigated the effect of evenly space-fixed springs on the divergence instability of a clamped disk with translational degrees of freedom. They proved that divergence instability of the coupled system is induced only when two times the number of nodal diameters of a mode is equal to a multiple of the number of stationary springs.

Yang [5] investigated the effect of rigid body degrees of freedom on the stability of splined guided disks. He concluded that, stable operation of the splined disk beyond critical speed is possible. He used modal functions of a stationary disk to compute the elastic displacement of the spinning disk. He proved that the divergence speed is independent of the spring stiffness, however the stable speed range increases with the spring stiffness because of the coupling effects from rigid-body degree of freedom.

Mote [6] investigated the stability of a collar disk (which slides freely along the axis of symmetry), subjected to a concentrated load moving at uniform speed. In his study he considered both a harmonic transverse load and a load proportional to transverse displacement and velocity. He found that the harmonic loading case leads to a classical critical speed analysis. In his study the proportional loading case represents the transverse guides. He concluded that the number, configuration and mechanical properties of the guides determine the transverse stability of the system.

Price [7] studied the effect of a rigid body translational degree of freedom on the dynamic response of rotating disks which are free to translate along the axis of symmetry, with the inner edge constrained to be perpendicular to that axis. He concluded that at super-critical speed interaction of forward and backward frequency loci results in flutter instability. He also concluded that multiple points guides or a sector guide increase the instability range, relative to a single point guide.

Khorasany and Hutton [8] investigated the stability characteristics of a spinning disk having rigid body translational degrees of freedom, constrained with only one space fixed spring. They concluded that the interaction of a forward or backward travelling wave with the rigid body translational mode does not induce flutter type instability. They showed that if the stiffness exceeds a certain value, the flutter instability will be induced and never disappears.

Tobias and Arnold [9] experimentally investigated the vibration characteristics of imperfect spinning clamped disks. Raman and Mote [10] used experimental results to investigate the vibration response of an imperfect disk. Kang and Raman [11] measured the transverse vibration of a disk coupled to surrounding fluids in an air-filled enclosure. D' Angelo, C., Mote,

C.D. [12] investigated experimentally the aerodynamically excited supercritical disk vibration. Thomas, O. et al [13] investigated experimentally the non-linear forced vibration of circular plates due to large displacements, with the excitation frequency close to the natural frequency of an asymmetric mode.

Jana and Raman [14] conducted experiments over a wide range of rotation speeds in the post-flutter region of a flexible disk rotating in an unbounded fluid. Based on their experimental investigations, the existence of a primary instability of a reflected travelling wave of the disk, followed by a secondary instability is confirmed. They observed frequency lock-ins over certain rotation speed ranges. They showed that a non-linear Von-Karman plate theory, coupled with a linear aerodynamic load with the form of a rotating damping is capable of capturing the primary instability of the system.

Khorasany and Hutton [15] conducted experimental tests to investigate the effect of large deformations on the frequency characteristics of spinning clamped disks. They present experimental results for vibration behavior of three uniform, thin, disks of different thickness, subjected to a constant lateral force of different amplitude. In particular, they presented the amplitude-speed and frequency-speed characteristic of the disks. Based on the experimental observations, they found that the application of a space fixed lateral force caused separation of the backward and forward travelling waves when the disk is stationary. This was expected due to the lack of symmetry and imperfection in the disks.

Khorasany and Hutton [16] numerically investigated the effect of geometrical nonlinear terms on the dynamic characteristics of a spinning clamped disk. They presented an analysis of the amplitude and frequency response of the disk, subjected to geometrical non-linear

displacements. In a case of a stationary disk, subjected to a stationary load, since the stress distribution is not symmetric, the frequencies of the forward and backward travelling waves do not coincide. In a case of spinning disk, for low levels of non-linearity stationary waves form and collapse within a small speed band.

Chen and Wong [17] studied analytically the vibration and stability of a spinning disk with axial spindle displacement in contact with a number of fixed springs. They found the behaviour of divergence instability close to critical speed is different than those of a spinning disk without axial spindle displacement. They concluded divergence instability occurs in a disk with axial displacement if two times the number of nodal diameters is equal to the number of stationary lateral springs.

Chen and Bogy [18] studied the effects of different load parameters, such as friction force, transverse mass, damping, and stiffness of a stationary load system in contact with the spinning disk on the stability of the system at sub- and super-critical speeds. They found that only two-mode approximation can exhibit all the features of eigenvalue changes. However, in the case of friction force, at least a four-mode approximation is required.

Young et al [19] investigated vibration response of a rotating clamped disk under the constraint of an elastically fixed space oscillating unit. They showed that taking account of the stiffness between the oscillating unit and the disk may result in extra flutter-type instability between the oscillating-unit mode and the dominant reflected disk modes, and these extra unstable regions are much larger than those of the flutter-type instability between flexible modes of the disk.

Schajer and Wang [20] identified the workpiece interaction with the saw body as an important factor influencing guided circular saw cutting stability. In another work Schajer [21] by using a geometrical model, explained “hunting behaviour” of guided saw, where the saw blade does not remain perpendicular to the drive shaft but always shifts to one side or the other, as an important factor in analyzing the stability characteristics of guided splined saws.

During my master research (M.A.Sc. at the University of British Columbia) [22] I investigated experimentally the effect of guide size and location on stability and cutting performance of a guided splined saw. A comprehensive experimental investigation of idling tests of splined saws with different guide configurations was conducted. The frequencies and amplitudes of the blade vibrations and the mean deflections of the blades were presented. An extensive cutting tests was conducted and the effect of different guide configurations on cutting accuracy was investigated. In the experimental investigations the cutting tests were conducted at different speeds, sub-critical and super-critical speeds for different guide configurations. The cutting results were compared to determine the guide configuration which results in the best cutting accuracy. It was concluded that the guided splined saw with a small pin-guide at the outer radius (blade rim) results in a better performance in compare with a conventional bigger sector guide systems.

Although extensive research has been done in this area, the vibration and stability of circular saw blades under cutting conditions is however, not well understood.

The papers by Chen J.S. [23-26] appear to be the first thorough investigation, concerning the effect of in-plane edge- loads on the natural frequencies of a spinning clamped disk. He concluded that the effect of the in-plane edge-load on the natural frequencies and stability of the

rotating disk is through the transverse component of the edge load on the boundary, and not through the membrane stress field it produces inside the disk. He found that, compressive, and conservative in-plane edge-loads decreases the natural frequencies of forward and backward travelling waves, but increases the natural frequencies of the reflected waves. He proved that the compressive edge load induces “divergence type” instability, and “flutter type instability”. To explain the mechanism of divergence and flutter type instability induced by a compressive, conservative, in-plane edge-load (F_r), he compared the work done by the edge load over one cycle when the disk is stable, at divergence, and flutter instability situations as follow [23]:

The displacement of a disk vibrating in a backward travelling wave at a given radial and angular position of (r, θ) can be expressed as [23]:

$$w = R_{mn}(r) \cos(n\theta + \omega_{mn}t + \alpha_{mn})$$

Where $R_{mn}(r)$ is the deflection of the blade as a function of r . ω_{mn} is the natural frequency of a mode with n nodal diameters, and m nodal circles, and α_{mn} is a constant phase. Then the velocity of a point at the edge of the disk ($r = b, \theta = 0$) can be calculated as [23]:

$$\dot{w} = -(\omega_{mn}t + n\Omega)R_{mn}(b) \sin(\omega_{mn}t + \alpha_{mn})$$

The disk is subjected to a conservative radial load of F_r . The transverse component of the edge load is $F_r \cdot \frac{\partial w}{\partial r}$; So, the work done by F_r over one cycle can be expressed as [23]:

$$-\frac{1}{2}F_r(\omega_{mn}t + n\Omega)R_{mn}(b) \frac{\partial R_{mn}(b)}{\partial r} \int_{\text{cycle}} \sin 2(\omega_{mn}t + \alpha_{mn}) dt$$

This work is zero when $\omega_{mn} \neq 0$; at a divergence situation ($\omega_{mn} = 0$) depends on α_{mn} this work might be negative or positive. This can explain why instability occurs when the conservative edge-load is present and the natural frequency of the mode becomes zero.

At “flutter type instability” assume that the disk is vibrating in the combination of backward travelling wave w_{mn} and a reflected wave w_{pq} ($\omega_{mn}, \omega_{pq} > 0$):

$$w_{mn} = R_{mn}(r) \cos(n\theta + \omega_{mn}t + \alpha_{mn})$$

$$w_{pq} = R_{pq}(r) \cos(n\theta + \omega_{pq}t + \alpha_{pq})$$

The work done by $F_r \cdot \frac{\partial w_{mn}}{\partial r}$ and $F_r \cdot \frac{\partial w_{pq}}{\partial r}$ over one cycle can be calculated as [23]:

$$-\frac{1}{2} F_r (\omega_{mn}t + n\Omega) R_{mn}(b) \frac{\partial R_{pq}(b)}{\partial r} \int_{cycle} \sin((\omega_{mn} - \omega_{pq})t + \alpha_{mn} - \alpha_{pq}) dt$$

In the situation that $\omega_{mn} \neq \omega_{pq}$, the work is zero. If $\omega_{mn} = \omega_{pq}$ then the work might be negative or positive. This can explain why instability can occurs when the in-plane edge load is present, and two frequency loci merge together.

In light of Chen’s work (abovementioned), in an independent study, Shen [27] predicted the stability of a clamped spinning disk, subjected to a stationary, concentrated in-plane edge load. He reached to the same conclusion on the effect of conservative, edge-loads as Chen [23]. He found that conservative edge-loads affect the stability through transverse component of the loads on the boundary.

Young [28] extended the work by Chen [23-26] and Shen [27] by considering the rotation speed to be characterized as the sum of a constant speed and a small, periodic perturbation. (His

motivation for this study was that in practice the spin rates fluctuate within a small interval [28]). He concluded that merge type (flutter) resonance can happen between modes of different nodal diameters if the stationary edge-load is present. He also showed that, when the stationary edge load is uniformly distributed, the lowest few unstable regions, whose maximum width of instability are relatively small, tend to enlarge at first as the load distribution widens and to reach maximum as the load distributed over half a circle. A further increase in the load distribution angle tends to reduce the lowest few unstable regions.

In order to understand the wash-boarding mechanism, an analytical model for wood cutting clamped circular saws was developed by Tian and Hutton [29]. In their study, the lateral cutting forces were represented by the product of a time-dependent periodic function and the lateral displacement of the saw teeth. In another work [30] they introduced an approach which predicts the physical instability mechanism that occurs during the interaction of the blade with a space fixed constraint. To provide physical insight into the stability characteristics of the system, they used a physical energy flux equation for the blade. They derived the energy variation ΔE of the disk over a period of $[0, \tau]$ for a constant spinning speed as [30]:

$$\Delta E = \int_0^{\tau} \left\{ \iint_A [q(w, r, \theta, t)(w_{,t} + \Omega w_{,\theta})] r dr d\theta \right\} dt$$

Where $q(w, r, \theta, t)$ represents a generalized lateral force, and $w_{,t} + \Omega w_{,\theta}$ represents the transverse velocity of a particle, attached to disk, observed by disk-fixed coordinates. Under stable condition ΔE will be nonzero periodic function of time, but over a complete cycle the change of total energy will be zero. From this equation it is clear that the change of total energy ΔE will increase when $q(w, r, \theta, t)$ is in phase with $(w_{,t} + \Omega w_{,\theta})$. In this case driving energy

required to maintain constant speed will be transferred into transverse vibration and instability will occur [30].

Recently Khorasany, Mohammadpanah, and Hutton [31], conducted experimental tests on the frequency characteristics of a guided splined saw, subjected to large lateral deflection. They found that the blade frequencies show a significant change as a result of the initial lateral displacement imposed by the external force. It was also found that due to the presence of the external force, a stationary wave develops and collapses at a higher speed. For the numerical simulations, they used the nonlinear governing equations based on Von Karman plate theory. They investigated the effect of nonlinearity on the amplitude and frequency response of the guided blade.

There is not any available literature or research on the dynamic response of a splined guided disk, subjected to in-plane edge loads. Understanding the effect of in-plane loads on the stability of a splined guided disk is of paramount importance in the current research. Therefore the focus of this work is on the dynamic characteristics of a guided splined disk, subjected to edge loads.

1.5 Objective and Scope

The main objective of this research is:

“To provide primary guide lines for sawmills in choosing blade thickness, and stable operating speeds.”

To meet this objective, the main task is defined as:

“To investigate the dynamic characteristics of guided splined saws during cutting.”

In order to fulfill this task, the approach taken in this thesis consists of the following subtasks:

- To develop a mathematical model that captures the essential physics of the problem
- To study stability characteristics of splined disks, subjected to edge loads
- To Conduct Experimental Tests of Guided Splined Saws

These tasks are presented in five chapters of this thesis.

Chapter 2 is devoted to mathematical modeling of a spinning splined guided disk subjected to in-plane outer and inner edge loads. In this chapter first the previously obtained results on the effect of edge-loads on the characteristics of a clamped disk are independently verified. Then the equations of motion for a guided splined disk subjected to in-plane edge loads on outer boundary and their corresponding interaction on inner boundary of disk are derived. A technique is developed for taking the derivative of eigenvalues of a splined disk with respect to edge loads. Then sensitivity of eigenvalues to edge loads is examined. Numerical solution of the equations of motion for a splined disk is used and the effect of edge loads on the natural frequencies and stability of the system are analyzed. The transverse response of a guided splined disk, subjected to edge loads are computed numerically at sub-critical, critical, super-critical, and flutter speeds of the disk.

Chapter 3 is concerned with the mechanism of instability for a spinning splined guided disk subjected to in-plane outer and inner edge loads. In this chapter, an expression for the energy induced into the spinning disk by the in-plane loads, and their interaction at the inner radius, is derived by computation of the rate of work done by the lateral component of the edge

loads. This chapter provides physical insight into instability mechanism of a guided splined disk subjected to in-plane loads.

Chapter 4 presents the experimental results of a guided splined disk. This chapter provides insights into the dynamic behavior of spinning disk by conducting experimental studies. Experimental observations of idling and cutting tests of a splined guided saw are presented in this chapter. First idling tests results are presented for a guided splined saw blade. Then the results of cutting tests for the same blade are presented. Particular interest here is to see how the idling results can be used to predict the stable region of the blade for cutting.

In chapter 5 experimental run-up tests of several guided splined saws of different sizes are presented, and the flutter instability zones are identified. Using the equations of motion for guided splined disks, developed in chapter 1 and 2, the flutter instability zones are defined for guided splined saws of various configurations. The experimental and numerical results are compared and discussed. Then the effect of the geometrical parameters of the blade on the start of flutter instability is analyzed. To provide primary practical design guide lines for sawmills the initiation of flutter speeds are computed for different blade diameters. The start of flutter instability speeds were computed and tabulated for different blade thickness. The results are also presented in a chart format.

Chapter 6 presents the summary and conclusions. This chapter also provides suggestions for future work on this subject.

Chapter 2: Modeling of a Spinning Splined Guided Disk Subjected to In-Plane Edge Loads Applied at the Outer and Inner Boundaries

2.1 Introduction

This chapter presents analytical results of the dynamic behavior of rotating disks subjected to in-plane edge loads. The governing non-damped linear equations of transverse motion of a spinning disk with a splined inner radius and constrained from lateral motion by guide pads are derived. The disk is driven by a matching splined arbor that offers no restraint to the disk in the lateral direction. Rigid body translational and tilting degrees of freedom are included in the analysis of total motion of the spinning disk. The disk is subjected to lateral constraints and loads. Also considered are applied conservative in-plane edge loads at the outer and inner boundaries. The numerical solutions of these equations are used to investigate the effect of the loads and constraints on the natural frequencies, critical speeds, and stability of a spinning disk.

2.2 Previous Work on the Effect of Edge Loads on Clamped Disks

Chen J.S. [23] investigated the frequency characteristics of clamped spinning disk, subjected to in-plane concentrated edge loads. He found that compressive edge loads decrease the natural frequencies of the forward and backward travelling waves, but increase the natural frequencies of reflected wave. He also concluded that, the compressive edge loads induce stationary type instability (divergence) before the critical speed and merge-type instability (flutter) after the critical speed when a reflected wave meets a forward or backward wave.

In this section, the previously obtained results by Chen J.S. [23] are independently verified and his conclusions on the effect of edge-loads on the characteristics of a clamped disk are examined.

Figure 2.1 Schematic of a Clamped Disk, Subjected to a Conservative In-Plane Compressive Edge Load

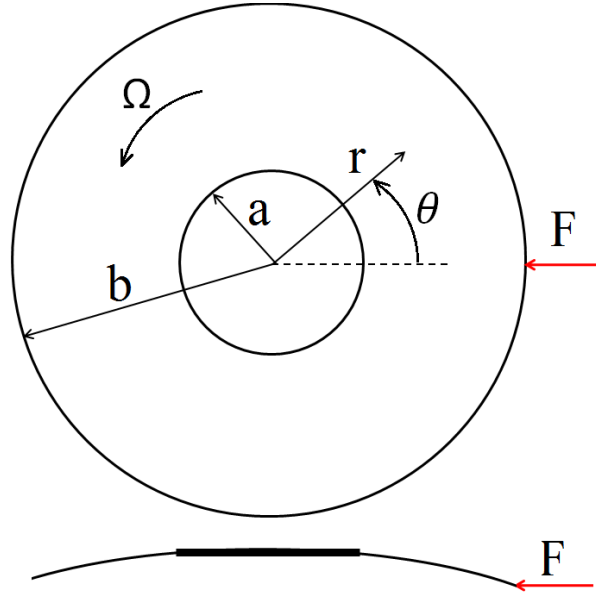


Figure 2.1 shows a schematic of a clamped disk, subjected to a conservative in-plane compressive edge load. The governing equation of motion for the disk, in terms of the transverse displacement w , with respect to a space fixed coordinates (r, θ) , is [23]:

$$\rho h(w_{,tt} + 2\Omega w_{,t\theta} + \Omega^2 w_{,\theta\theta}) + D\nabla^4 w + Lw + \hat{L}w = 0 \quad (2.1)$$

L and \hat{L} are the membrane stress field operators due to centrifugal force, and normal edge load, respectively. L and \hat{L} can be calculated by following a procedure described in Chen [23].

The boundary conditions for equation 2.1 are [23]:

$$w = 0, w_{,r} = 0 \quad \text{at } r = a \quad (2.2)$$

$$B_1 w + F B_2 w = 0, \quad B_3 w = 0 \quad \text{at } r = b \quad (2.3)$$

Whereas B_1 , B_2 and B_3 are defined as [23]:

$$B_1 = \frac{\partial}{\partial r} \left(\frac{\partial^2}{\partial r^2} + \frac{\partial}{r \partial r} + \frac{\partial^2}{r^2 \partial \theta^2} \right) + \frac{1-\nu}{r^2} \left(\frac{\partial^3}{\partial r \partial \theta^2} - \frac{\partial^2}{r \partial \theta^2} \right) \quad (2.4)$$

$$B_2 = \frac{\delta(\theta)}{bD} \frac{\partial}{\partial r} \quad (2.5)$$

$$B_3 = \frac{\partial^2}{\partial r^2} + \frac{\nu}{r} \left(\frac{\partial}{\partial r} + \frac{\partial^2}{r \partial \theta^2} \right) \quad (2.6)$$

The solution of equation 2.1 can be obtained by application of the Galerkin method. A particular solution of the equation is assumed to be:

$$w(r, \theta, t) = \sum_{m,n=0}^{\infty} [S_{mn}(t) \sin m\theta + C_{mn}(t) \cos m\theta] R_m(\lambda_{mn}r) \quad (2.7)$$

Substituting equation 2.7 into equation of motion 2.1, result in a set of simultaneous partial differential equations in $S_{mn}(t)$, and $C_{mn}(t)$, while $m, n = 0, 1, 2, \dots$. The solution of these equations determines the transverse displacement of the disk (for details see Appendix C).

The material and geometric properties of the disk under investigation in [23] are:

$$\rho = 7840 \frac{\text{kg}}{\text{m}^3}, E = 2.03 \times 10^{11} \text{Pa}, \nu = 0.27, a = 101.6 \text{mm}, b = 203.2 \text{mm}, \text{ and } h = 1.02 \text{mm}$$

Figure 2.2 shows the variation of eigenvalues as a function of speed. The dashed lines are the results for the freely spinning disk, and the solid lines indicate the results for the disk, subjected to $F = 3.5 \frac{D}{b} = 330 \text{N}$. The results are exactly matched with the results previously obtained by Chen [23].

Figure 2.2 Variations of Eigenvalues as a Function of Rotation Speed, (--dashed lines) Free Spinning Clamped Disk, (-solid lines) Clamped Disk Subjected to the Edge Load $F=3.5 D/b$

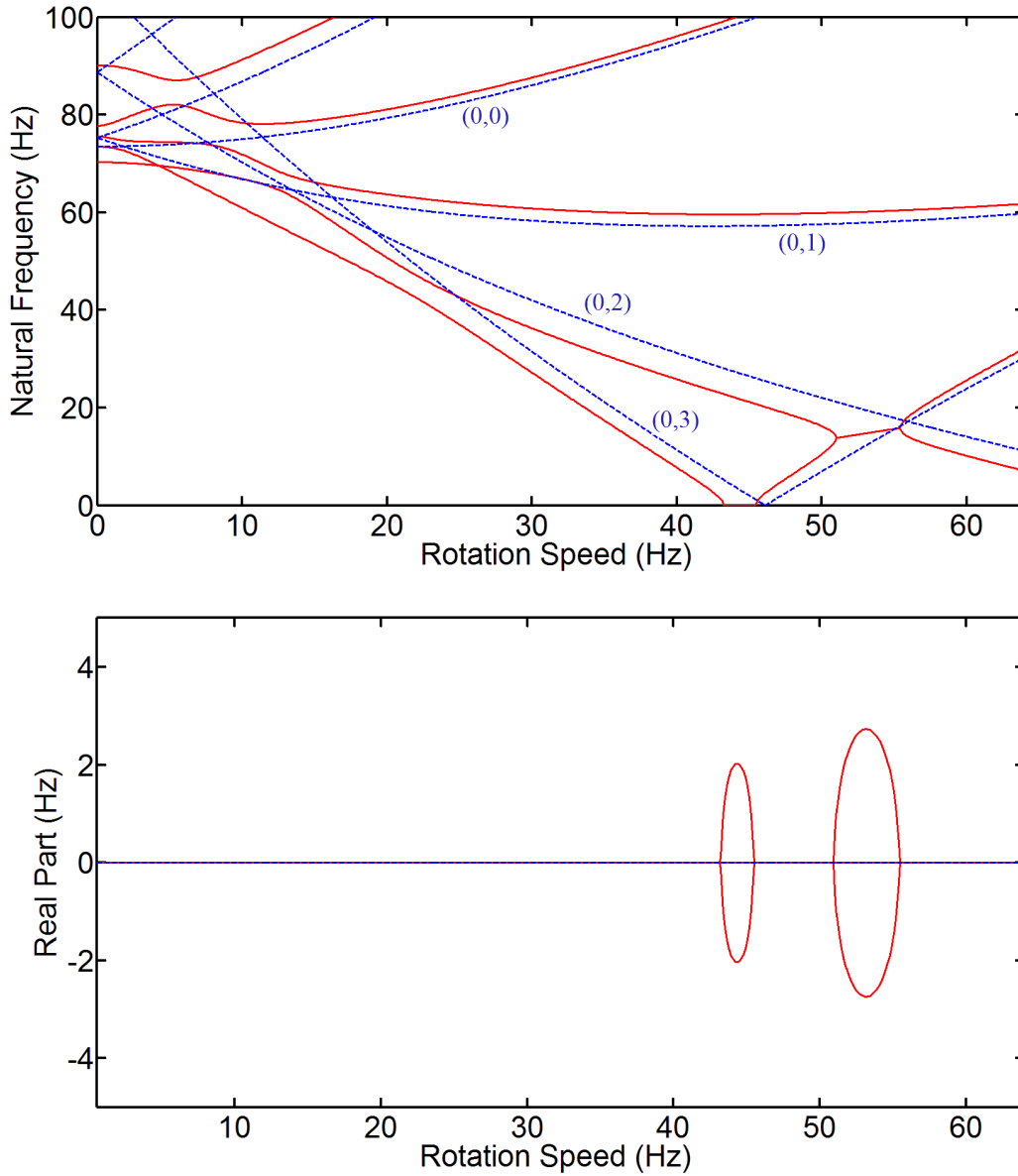


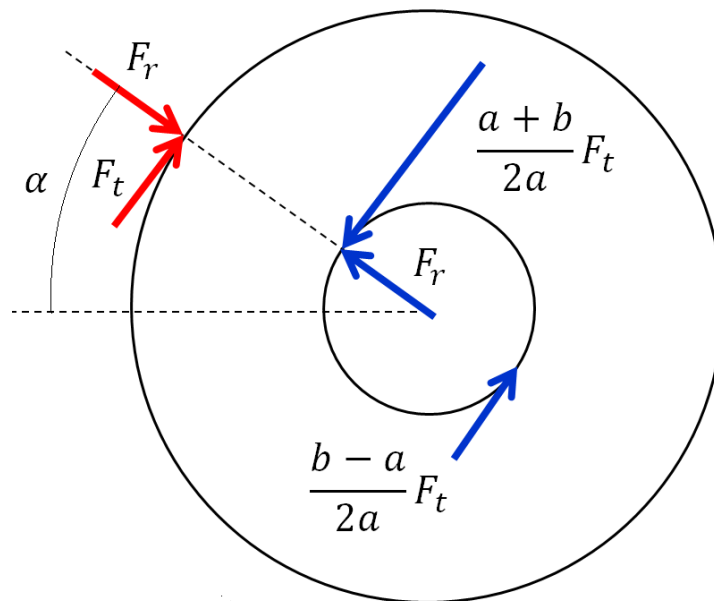
Figure 2.2 illustrates the effect of a conservative in-plane edge load. The graph indicates that the load decreases the natural frequencies of forward and backward waves, and it increases the natural frequencies of reflected waves.

The graph shows that the real part of the eigenvalue for mode (0,3) is positive when the imaginary part is zero in case the disk is subjected to the edge load. Therefore, the load induces a divergence type instability. It also induces a flutter type instability when the backward wave (0,2) intersects the reflected travelling wave of mode (0,3). These findings verified the conclusions of Chen [23] on the effect of in-plane edge load on the dynamic behaviour of a clamped disk.

2.3 Equations of Motion for a Spinning Splined Guided Disk Subjected to In-Plane Outer and Inner Edge Loads

Consider an in-plane radial force F_r and an in-plane tangential force F_t acting on the outer edge of the disk and one possible configuration for the interaction loads on the inner edge of the disk (Figure 2.3):

Figure 2.3 Schematic of a Splined Disk Subjected to In-Plane Edge Loads, and Their Inner Interaction Loads



The governing equation of motion for the disk, in terms of the transverse displacement w , with respect to a stationary coordinates system (r, θ) , considering: (i) rigid body translation Z and tilting motions θ_x and θ_y ; (ii) a space fixed linear spring k_z located at (r_k, θ_k) ; (iii) a space fixed lateral force f_z located at (r_f, θ_f) and (iv) Asymmetric membrane stress due to in-plane edge loads is:

$$\begin{aligned} \rho h (w_{,tt} + 2\Omega w_{,t\theta} + \Omega^2 w_{,\theta\theta}) + D \nabla^4 w - \frac{h}{r} (\sigma_{rr} r w_{,r})_{,r} - \frac{h}{r^2} \sigma_{\theta\theta} w_{,\theta\theta} + \rho h \ddot{Z} + \rho h (r \ddot{\theta}_x \sin \theta - \\ r \ddot{\theta}_y \cos \theta) + \rho h (2\Omega r \cos \theta \dot{\theta}_x + 2\Omega r \sin \theta \dot{\theta}_y) - \frac{h}{r} \left\{ (\sigma_r r w_{,r} + \tau_{r\theta} w_{,\theta})_{,r} + (\tau_{r\theta} w_{,r} + \right. \\ \left. \sigma_{\theta} w_{,\theta})_{,\theta} \right\} = -\frac{k_z}{r} (w + Z + r_k \sin \theta_k \theta_x - r_k \cos \theta_k \theta_y) + \frac{f_z}{r} \end{aligned} \quad (2.8)$$

σ_{rr} and $\sigma_{\theta\theta}$ are axi-symmetric in-plane stresses due to centrifugal acceleration. The closed form solution of σ_{rr} and $\sigma_{\theta\theta}$ for a disk with free inner boundary condition can be found in Appendix A.

σ_r , σ_{θ} and $\tau_{r\theta}$ are asymmetric stresses due to the edge loads; and are to be determined from the known values of F_r and F_t . The closed form solution of stresses can be found in Appendix D.

The boundary equations at the outer and inner edges respectively are:

$$\begin{aligned} \frac{F_r \delta(\theta - \alpha)}{bD} w_{,r} + \frac{F_t \delta(\theta - \alpha)}{b^2 D} w_{,\theta} + (w_{,rr} + \frac{1}{r} w_{,r} + \frac{1}{r^2} w_{,\theta\theta})_{,r} + \frac{1-\nu}{r^2} \left((w_{,\theta\theta})_{,r} - \frac{1}{r} w_{,\theta\theta} \right) = 0 \end{aligned} \quad (2.9)$$

$(r = b)$

$$\begin{aligned} -\frac{F_t(a+b)\delta(\theta - \alpha)}{2a^3 D} w_{,\theta} + \frac{F_t(b-a)\delta(\pi + \theta - \alpha)}{2a^3 D} w_{,\theta} + (w_{,rr} + \frac{1}{r} w_{,r} + \frac{1}{r^2} w_{,\theta\theta})_{,r} + \frac{1-\nu}{r^2} \left((w_{,\theta\theta})_{,r} - \right. \\ \left. \frac{1}{r} w_{,\theta\theta} \right) - \frac{F_r \delta(\theta - \alpha)}{aD} w_{,r} = 0 \end{aligned} \quad (2.10)$$

$(r = a)$

Where $\delta(\theta)$ is the Dirac delta function.

Equations (2.8-2.10) govern the dynamics motion of a splined spinning disk subjected to the edge loads shown in Figure 2.3.

2.4 Sensitivity Analysis of Eigenvalues of Spinning Splined Disk to In-plane Edge Loads

To analyze the sensitivity of the eigenvalues of the spinning disk to in-plane edge loads, the derivative of the eigenvalues of the system with respect to the in-plane edge loads is calculated. Adopting a technique used by Chen [23], the derivative of the eigenvalues with respect to the edge loads is derived.

The equation of motion of a spinning disk, without considering the membrane stress, can be written as (here for simplicity, we do not consider the membrane stress):

$$\rho h(w_{,tt} + 2\Omega w_{,t\theta} + \Omega^2 w_{,\theta\theta}) + D\nabla^4 w = 0 \quad (2.11)$$

Together with the boundary conditions of equations (2.9) and (2.10).

Defining the operators:

$$M = \rho h$$

$$G = 2\Omega \frac{\partial}{\partial \theta}$$

$$K = \Omega^2 \frac{\partial^2}{\partial \theta^2} + D\nabla^4$$

$$\nabla^4 = \nabla^2 \nabla^2 = \left(\frac{\partial^2}{\partial r^2} + \frac{1}{r} \frac{\partial}{\partial r} + \frac{1}{r^2} \frac{\partial^2}{\partial \theta^2} \right) \left(\frac{\partial^2}{\partial r^2} + \frac{1}{r} \frac{\partial}{\partial r} + \frac{1}{r^2} \frac{\partial^2}{\partial \theta^2} \right)$$

$$L_1 = \frac{\partial}{\partial r} \left(\frac{\partial^2}{\partial r^2} + \frac{\partial}{r \partial r} + \frac{\partial^2}{r^2 \partial \theta^2} \right) + \frac{1-\nu}{r^2} \left(\frac{\partial^3}{\partial r \partial \theta^2} - \frac{\partial^2}{r \partial \theta^2} \right)$$

$$L_2 = \frac{\delta(\theta-\alpha)}{D} \frac{\partial}{\partial r}$$

$$L_3 = \frac{\delta(\theta-\alpha)}{D} \frac{\partial}{\partial \theta}$$

$$L_4 = \frac{\delta(\pi+\theta-\alpha)}{D} \frac{\partial}{\partial \theta}$$

The equation and the boundary conditions become:

$$\left\{ \begin{array}{l} M\ddot{w} + G\dot{w} + Kw = 0 \\ b^2L_1w + bF_rL_2w + F_tL_3w = 0 \\ 2a^3L_1w - 2a^2F_rL_2w - (a+b)F_tL_3w + (b-a)F_tL_4w = 0 \end{array} \right. \quad \begin{array}{l} \text{(2.12)} \\ \text{at } r = b \\ \text{at } r = a \end{array}$$

For simplicity we analyze the effect of the radial and tangential loads separately.

2.4.1 Effect of Radial Load

Assume a solution in the form:

$$w = w_{mn}(r, \theta)e^{\lambda_{mn}t} \quad (2.13)$$

Where:

$$w_{mn}(r, \theta) = R_m(r)e^{\pm in\theta} \quad (2.14)$$

Substituting the solution (2.13) into the equation (2.12):

$$\lambda_{mn}^2 M w_{mn} + \lambda_{mn} G w_{mn} + K w_{mn} = 0 \quad (2.15)$$

Consider λ_{mn}^0 and w_{mn}^0 as the eigenvalues and shape functions of free spinning disk.

(When $F_r = 0$)

Then the equation (2.15) for a free spinning disk is:

$$(\lambda_{mn}^0)^2 M w_{mn}^0 + \lambda_{mn}^0 G w_{mn}^0 + K w_{mn}^0 = 0 \quad (2.16)$$

The boundary equations become (substitute $F_r = 0$ in the boundary equations)

$$L_1 w_{mn}^0 = 0 \quad \text{at } r = a \text{ and } r = b$$

Taking the derivative of equation (2.15) with respect to F_r results in (See the mathematical details in Appendix H):

$$2\lambda_{mn}^0 \frac{\partial \lambda_{mn}}{\partial F_r} M w_{mn}^0 + (\lambda_{mn}^0)^2 M \frac{\partial w_{mn}}{\partial F_r} + \frac{\partial \lambda_{mn}}{\partial F_r} G w_{mn}^0 + \lambda_{mn}^0 G \frac{\partial w_{mn}}{\partial F_r} + K \frac{\partial w_{mn}}{\partial F_r} = 0 \quad (2.17)$$

And the boundary equations become:

$$bL_1 \frac{\partial w_{mn}}{\partial F_r} + L_2 w_{mn}^0 = 0 \quad \text{at } r = b$$

$$aL_1 \frac{\partial w_{mn}}{\partial F_r} - L_2 w_{mn}^0 = 0 \quad \text{at } r = a$$

Multiplying the conjugate of equation (2.16) by $\frac{\partial w_{mn}}{\partial F_r}$ results in:

$$(\bar{\lambda}_{mn}^0)^2 \frac{\partial w_{mn}}{\partial F_r} M \bar{w}_{mn}^0 + \bar{\lambda}_{mn}^0 \frac{\partial w_{mn}}{\partial F_r} G \bar{w}_{mn}^0 + \frac{\partial w_{mn}}{\partial F_r} K \bar{w}_{mn}^0 = 0 \quad (2.18)$$

Multiplying equation (2.17) by \bar{w}_{mn}^0 , and subtracting (2.18) from it results in:

$$\begin{aligned} & 2\lambda_{mn}^0 \frac{\partial \lambda_{mn}}{\partial F_r} M \bar{w}_{mn}^0 w_{mn}^0 + \frac{\partial \lambda_{mn}}{\partial F_r} \bar{w}_{mn}^0 G w_{mn}^0 + \lambda_{mn}^0 \bar{w}_{mn}^0 G \frac{\partial w_{mn}}{\partial F_r} + \bar{w}_{mn}^0 K \frac{\partial w_{mn}}{\partial F_r} - \\ & - \bar{\lambda}_{mn}^0 \frac{\partial w_{mn}}{\partial F_r} G \bar{w}_{mn}^0 - \frac{\partial w_{mn}}{\partial F_r} K \bar{w}_{mn}^0 = 0 \end{aligned} \quad (2.19)$$

Integrating equation (2.19) over an area of a circular plate ($[0, 2\pi]$ and $[a, b]$), and considering the boundary equations results in:

$$4\pi i \omega_{mn} \rho h (\omega_{mn} \pm n\Omega) \frac{\partial \lambda_{mn}}{\partial F_r} \int_a^b R_m^2(r) r dr - \omega_{mn} \left(R_m(b) \frac{\partial R_m(b)}{\partial r} - R_m(a) \frac{\partial R_m(a)}{\partial r} \right) = 0 \quad (2.20)$$

Assume that $\lambda_{mn} = \sigma_{mn} + i\omega_{mn}$. For a free spinning disk, the real part of the eigenvalue is zero, therefore, $\lambda_{mn}^0 = i\omega_{mn}$

Rearranging the equation (2.20) results in:

$$\frac{\partial \lambda_{mn}}{\partial F_r} = - \frac{i \left(R_m(b) \frac{\partial R_m(b)}{\partial r} - R_m(a) \frac{\partial R_m(a)}{\partial r} \right)}{4\pi \omega_{mn} \rho h (\omega_{mn} \pm n\Omega) \int_a^b R_m^2(r) r dr} \quad (2.21)$$

For $a < b$:

$$R_m(b) \frac{\partial R_m(b)}{\partial r} > R_m(a) \frac{\partial R_m(a)}{\partial r} \quad \text{and} \quad \int_a^b R_m^2(r) r dr > 0$$

(See Appendix H for details)

Therefore, for forward and backward waves ($\omega_{mn} \pm n\Omega > 0$), equation (2.21) is negative. As a result, the change in λ_{mn} is negative. This means that the application of F_r decreases the eigenvalues of forward and backward waves. For reflected waves ($\omega_{mn} \pm n\Omega < 0$), equation (2.21) is positive, therefore the change in λ_{mn} is positive. This means that the application of F_r increases the eigenvalues of reflected waves. The expression (2.21) does not hold when $\omega_{mn} \pm n\Omega = 0$ (critical speeds).

2.4.2 Effect of Tangential Load

Following the same procedure as the radial loads, the derivative of eigenvalues with respect to a tangential load F_t , is obtained as: (See Appendix H for complete mathematical calculations)

$$\frac{\partial \lambda_{mn}}{\partial F_t} = - \frac{ni(bR_m(b) - aR_m(a))}{4\pi\rho h(\omega_{mn} \pm n\Omega) \int_a^b R_m^2(r) r dr} \quad (2.22)$$

For forward waves and backward waves ($\omega_{mn} \pm n\Omega > 0$), equation (2.22) is negative, therefore the change in λ_{mn} is negative. It means that the application of F_t decreases the eigenvalues of forward and backward waves. For reflected waves ($\omega_{mn} \pm n\Omega < 0$), equation (2.22) is positive, therefore the change in λ_{mn} is positive. It means that the application of F_t increases the eigenvalues of reflected waves. In addition, for $n = 0$ (modes with no nodal diameter), equation (2.22) becomes zero:

$$\frac{\partial \lambda_{mn}}{\partial F_t} = 0 \quad (2.23)$$

Therefore, tangential loads do not have an effect on modes with no nodal diameter.

Equations (2.21) and (2.22) indicate that, for a free spinning splined disk, the derivative of eigenvalues with respect to the radial and tangential loads is purely imaginary. Therefore, in-plane edge loads only affect the imaginary part of eigenvalues. In other words, the effect of in-plane edge loads on the real part of eigenvalues is zero. Since the eigenvalues of a free splined disk are purely imaginary, the real part of the eigenvalues for a free splined disk, subjected to in-plane loads, is zero. It can be concluded that in-plane edge loads do not induce any instability to the splined disk.

2.5 Numerical Results

2.5.1 Effect of In-plane Edge Loads on the Eigenvalues

2.5.1.1 Special Case (a Rigid Splined Disk)

We start with the simpler case of a rigid splined disk, subjected to the radial and tangential forces shown in Figure 2.2. The parameters which govern the motion of the disk are the rigid body tilting and translational motion θ_x, θ_y and z . Since the applied forces F_r and F_t are in balance with the inner interaction forces, and the disk is rigid the boundary equations vanish. Consider a rigid disk ($w = 0$), the equations of motion are reduced to (for mathematical details see Appendix E):

$$(\ddot{\theta}_x \sin \theta - \ddot{\theta}_y \cos \theta) + 2\Omega (\cos \theta \dot{\theta}_x + \sin \theta \dot{\theta}_y) = 0 \quad (2.24)$$

$$\ddot{\theta}_x + 2\Omega \dot{\theta}_y + \frac{(b-a) \sin \alpha F_r}{\rho h l} \theta_x = 0 \quad (2.25)$$

$$\ddot{\theta}_y - 2\Omega \dot{\theta}_x + \frac{(b-a) \cos \alpha F_r}{\rho h l} \theta_y = 0 \quad (2.26)$$

Equations (2.25) and (2.26) indicate that F_t and the interaction of F_t on the inner edge vanish from the equations. Therefore, one initial conclusion is that the tangential load has no effect on the eigenvalues of a splined rigid disk.

The solution of this system of second order differential equations can be written as:

$$\theta_x = \theta e^{i\omega_n t}, \theta_y = i\theta e^{i\omega_n t} \quad (2.27)$$

Where θ is a constant. ω_n is a real value and can be obtained from the following equation:

$$\omega_n = \frac{2\Omega + \sqrt{4\Omega^2 - 2\gamma}}{2} \quad (2.28)$$

Whereas,

$$\gamma = \frac{(b-a)}{\rho h l} F_r \quad \text{and} \quad I = \frac{\pi}{4} (b^4 - a^4) \quad (2.29)$$

Since ω_n is a real value, equation (2.28) holds if:

$$F_r \leq \frac{2\rho h l \Omega^2}{(b-a)} \quad (2.30)$$

The term $\frac{2\rho h l \Omega^2}{(b-a)}$ can be defined as the critical load of a free splined rigid disk, subjected to in-plane radial load at a given spinning speed. (Mathematical details can be found in Appendix E).

Equations (2.30) suggests that the natural frequency of a free splined spinning rigid disk ($F_r = 0$) is a function of rotation ($\omega_n = 2\Omega$). The natural frequency of a splined spinning rigid disk, subjected to a radial in-plane force ($F_r \neq 0$) is a function of rotation speed and magnitude of the load. Taking the derivative of natural frequency with respect to load (Eq. 2.31) indicates that application of F_r (for the value below the critical load at any rotation speed) decreases the natural frequency of the system. In addition, the effect of F_r decreases as the rotation speed increases.

$$\frac{\partial \omega_n}{\partial F_r} = - \frac{b-a}{\rho h l \sqrt{4\Omega^2 - 2\gamma}} \quad (2.31)$$

Now, consider a case where the rigid disk only has rigid body translational movement, and it is constrained by a lateral spring (k_z). The equation of motion is:

$$\rho h \pi (b^2 - a^2) \ddot{Z} = -k_z Z, \text{ which results in } \omega_n = \sqrt{\frac{k_z}{\rho h \pi (b^2 - a^2)}} \quad (2.32)$$

As the equations for the rigid disk indicate the in-plane forces have no effect on the frequencies of the system. Also the in-plane loads provide no coupling between the rigid body tilting and rigid body translational in the absence of lateral springs.

Figure 2.4 provides the graphical illustration of above results. The graphs indicate the variation of eigenvalues as a function of rotation speed. The dashed lines are the results for a free spinning splined rigid disk without considering the coupling effect of the spring, and the blue solid lines with considering the coupling effect of the spring. The thick dashed and solid red lines are the results for a same system, subjected to a radial load F_r , at outer edge at angular position of α , considering the coupling effect of the spring.

The results are obtained for a rigid disk of $a = 75mm$, $b = 215mm$, $h = 1.5mm$, $\rho = 7800 \text{ kg/m}^3$ subjected to a lateral spring of $k_z = 10^4 \frac{N}{m}$ at outer radius at $\alpha = 0^\circ$, $F_r = 100N = 1660 \frac{\rho h l}{b}$, at $\alpha = 45^\circ$.

Figure 2.4 Variation of Natural Frequencies as a Function of Rotation Speed, (-- blue dash lines) Free Spinning Splined Rigid Disk, (- blue solid lines) The Rigid Body Motions are Coupled by a Lateral Spring, (-- red dash lines) Free Spinning Splined Rigid Disk, Subjected to a Radial Load, (- red solid lines) Spinning Splined Rigid Disk, Constrained by a Lateral Spring, Subjected to a Radial Load

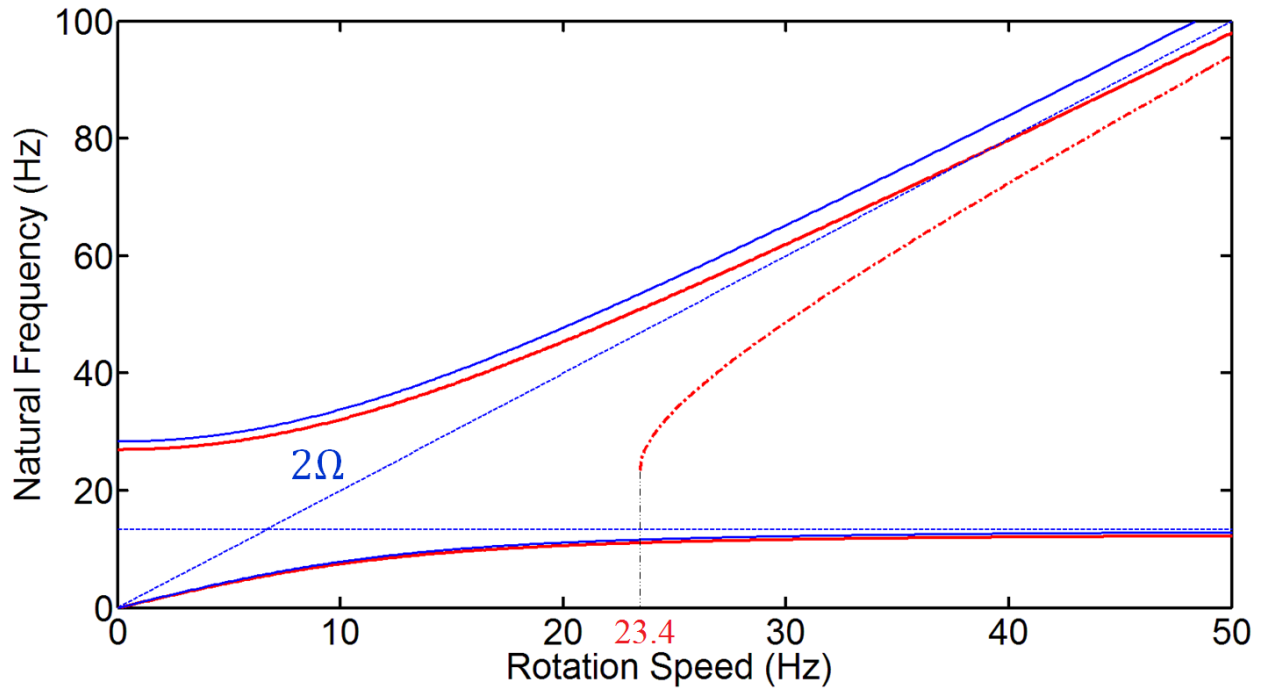


Figure 2.4 illustrates the effect of application of a radial load. For a free spinning rigid disk, the tilting natural frequency is 2Ω ; and application of $F_r = 100N = 1660 \frac{\rho h l}{b}$ decreases the natural frequency after the rotation speed of 23.4Hz. (Before this speed, since the load is higher than the critical load the tilting natural frequency vanishes). For a constrained spinning rigid disk by the lateral spring, application of radial load decreases the natural frequencies.

2.5.1.2 General Case (A Guided Splined Flexible Disk)

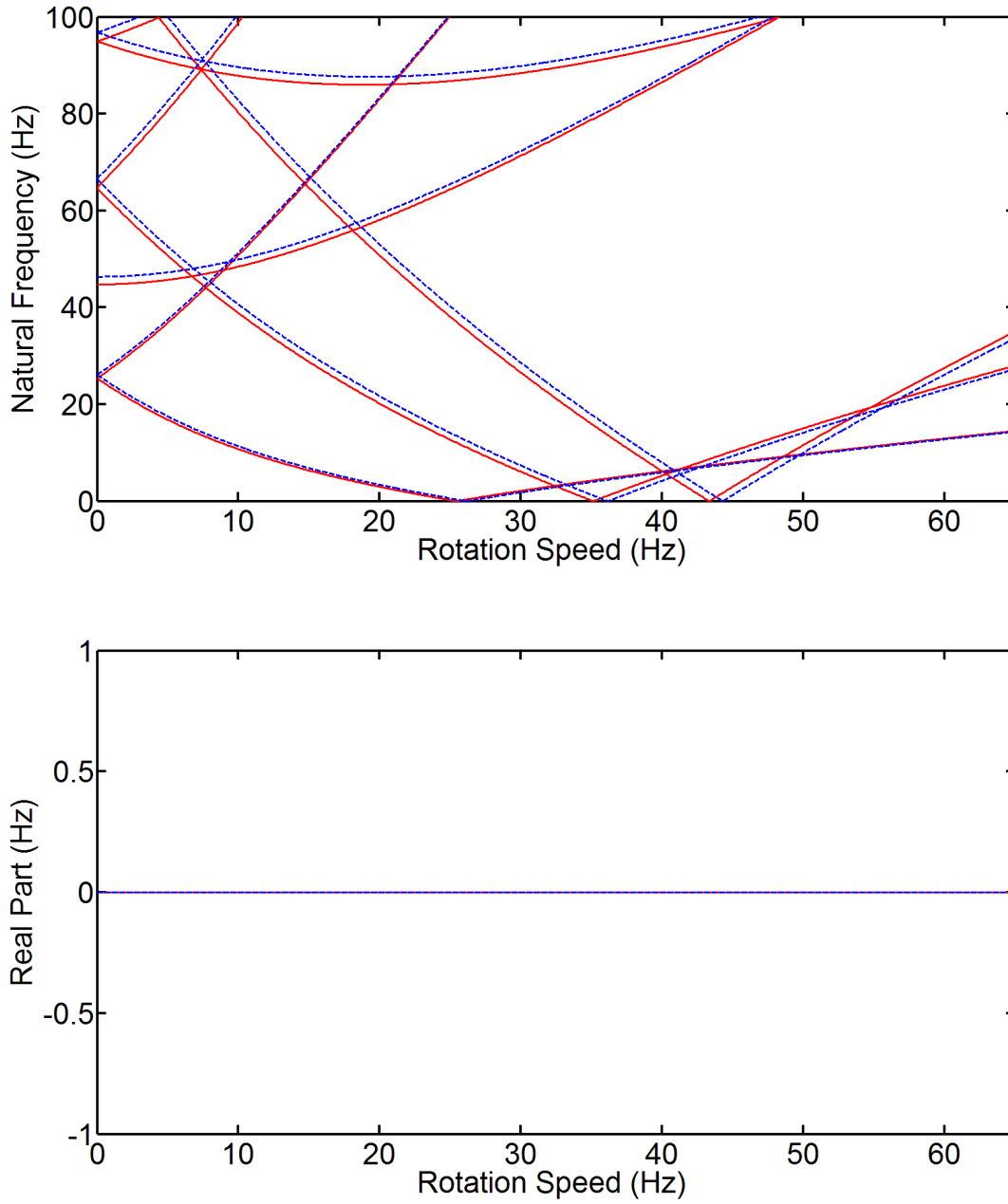
Consider a flexible disk with the following physical properties:

$$a = 75\text{mm}, b = 215\text{mm}, h = 1.5\text{mm}, E = 2.03 \times 10^{11}\text{pa}, \rho = 7800 \text{ kg/m}^3, \text{ and } \nu = 0.29.$$

First, to examine the effect of the in-plane edge loads on the bending frequencies of a free splined spinning disk, the eigenvalues are computed numerically for the disk subjected to a radial load of $F_r = 3.6 \frac{D}{b} = 1000N$, and a tangential load of $F_t = 3.6 \frac{D}{b} = 1000N$.

Figure 2.5 shows the variation of eigenvalues as a function of rotation speed for the flexible disk without considering the rigid body motions. The dashed lines are the results for a free spinning splined disk, and the solid lines are the results for the disk, subjected to in-plane loads.

Figure 2.5 Variation of eigenvalues as a Function of Rotation Speed, (--blue dash lines) Free Spinning Splined Disk, (- red solid lines) Free Spinning Splined Disk, Subjected to Edge Loads



The results from Figure 2.5 indicate that the edge load decreases the natural frequencies of forward, and backward travelling waves and increases the natural frequencies of reflected waves. However the effect of the loads on the natural frequencies is not significant.

The results also indicate that, unlike clamped disks, in-plane edge loads do not have any coupling effect on the bending modes. The in-plane loads thus do not induce any single or merged type resonance in the disk (the real parts are zero).

Now, to examine the effect of the in-plane edge loads on the bending frequencies of a guided splined spinning disk (The disk is constrained by 9 lateral springs of stiffness $k = 10^5 \frac{N}{m}$ distributed in a 100×100 mm square area which represents the guide) the eigenvalues of the system are computed numerically. Figure 2.6 presents the results for a guided splined disk. The disk is subjected to the edge loads ($F_r = F_t = 3.6 \frac{D}{b} = 1000N$, at $\alpha = 45^\circ$). Figure 2.6 indicates the effect of the in-plane loads on the eigenvalues. The results indicate that the loads decrease the natural frequencies of backward waves, but increase the natural frequencies of reflected waves. However, the effect is not significant (less than 0.5% for the 4th frequency path), and for the first two frequency paths is almost zero.

Figure 2.7 (which present the real part of the eigenvalues) indicates that there are two minor divergence instabilities at about 42Hz and 59Hz rotation speeds (the real part of eigenvalues is positive, while the imaginary part is zero). The application of edge loads slightly decreases the real part of the eigenvalues at these speeds. It also indicates that the span of rotation speeds at which the real part is positive is smaller for the disk subjected to edge loads. In other word, the edge loads decrease both the level and width of divergence instability zone. But the edge loads, increases the level and width of the flutter instability zone.

Figure 2.6 Variation of Imaginary Part of Eigenvalues as a Function of Rotation Speed, (--blue dash lines) Free Spinning Guided Splined Disk, (- red solid lines) Free Spinning Guided Splined Disk, Subjected to Edge Loads

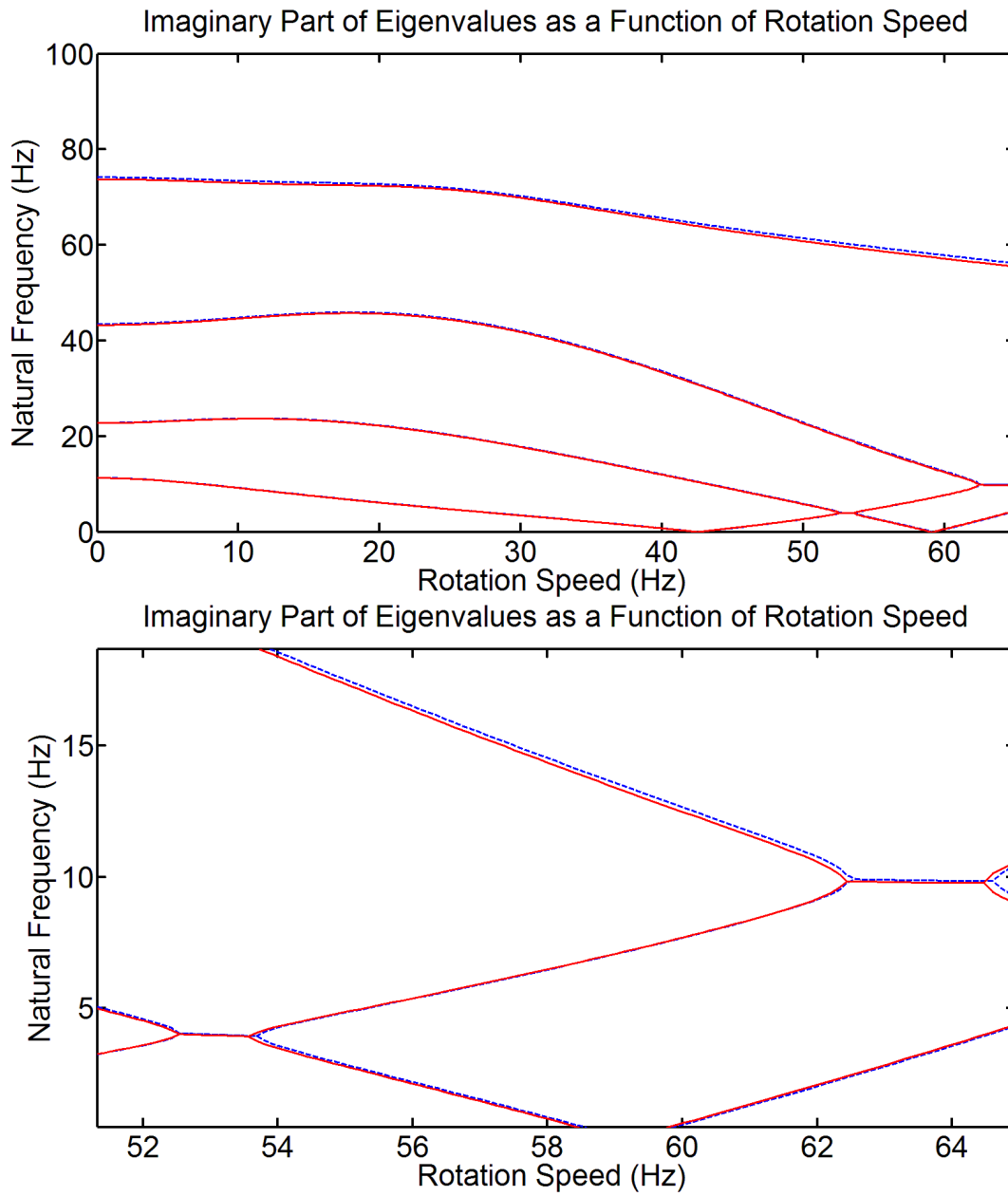
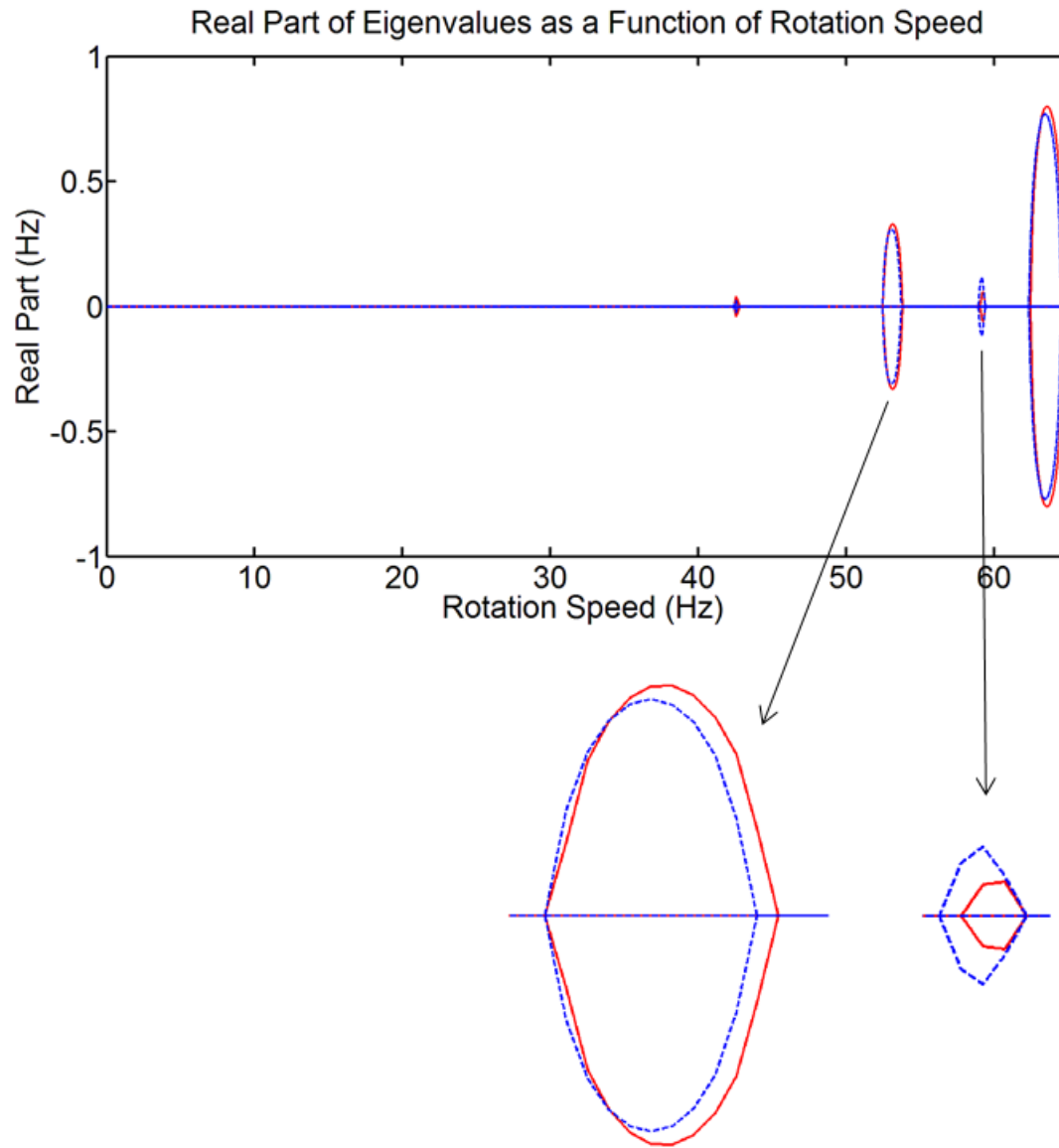


Figure 2.7 Variation of Real Part of Eigenvalues as a Function of Rotation Speed, (--blue dash lines) Free Spinning Guided Splined Disk, (- red solid lines) Free Spinning Guided Splined Disk, Subjected to Edge Loads

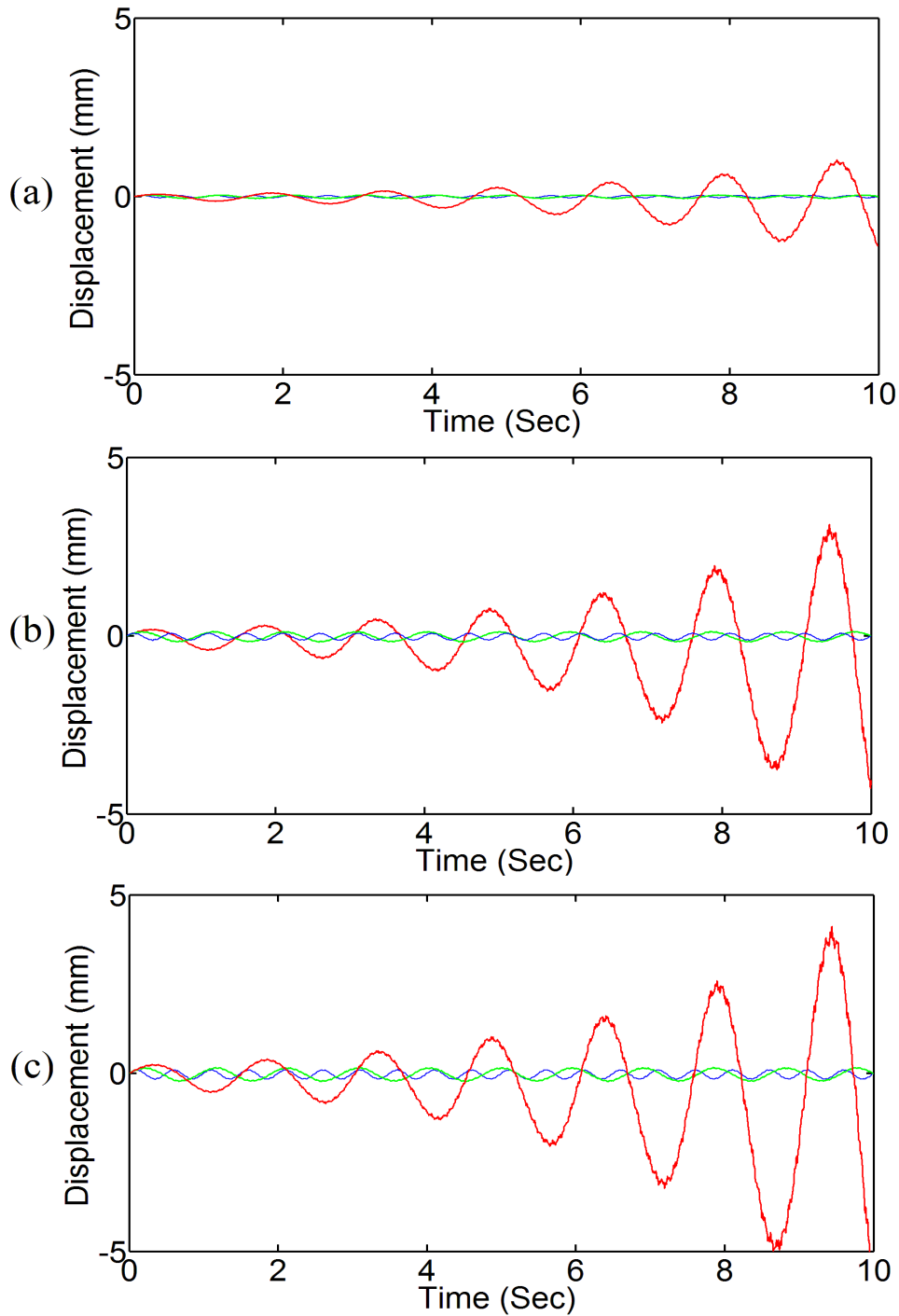


2.5.2 Transverse Response of a Disk to In-plane Edge Loads

For further analysis on the effect of the in-plane loads the transverse vibration of the guided splined disk, subjected to the edge loads, is computed in the time domain at different speeds. The results are computed for three different speeds: a) At first minor critical speed (42Hz), b) At a super critical speed (50Hz), c) At a flutter instability speed (53Hz). Figures 2.8 shows the transverse vibration of the outers rim of the disk at $\alpha = 45^\circ$, subjected to a radial load of $F_r = 3.6 \frac{D}{b} = 1000N$, and a tangential load of $F_t = 3.6 \frac{D}{b} = 1000N$. A small lateral force $F_l = 5N$ is applied at the same position as the radial and tangential loads as a source of lateral perturbation for the system.

Figure 2.8 shows the transverse response of the guided splined disk subjected to different load configurations at three different speeds. Figure (2.8 a) is the result for the system subjected only to the radial load. Figure (2.8 b) is the result for the system subjected only to the tangential load. And, Figure (2.8 c) is the result for the system subjected to both the radial and tangential loads.

Figure 2.8 Transverse Vibration of the Disk Computed for Outer Radius at $\alpha = 45^\circ$, Subjected to (a) A Concentrated Radial In-plane Edge Load (b) A Concentrated Tangential In-plane Edge Load (c) Concentrated Radial and tangential In-plane Edge Load, (blue graph) $\Omega = 42\text{Hz}$, (green graph) $\Omega = 50\text{Hz}$, (red graph) $\Omega = 53\text{Hz}$, For All Cases, the Lateral Load is $F_l = 5\text{N}$



As the results indicate, the disk is unstable only at the flutter instability speed (53Hz). It also can be concluded from the results (Figure 2.8 a, b, and c) that the effect of tangential load is much more pronounced than the radial load. (This issue will be analyzed with more depth in the next chapter through comparing the work done in one cycle by the tangential and radial loads.)

2.6 Summary

The effect of in-plane edge loads on the vibration characteristics of a spinning disk was investigated. Analytical investigations show that in-plane edge loads affect the dynamic behaviour of spinning disks through membrane stress and boundary conditions. Analysis indicates that in-plane edge loads tend to decrease the natural frequencies of forward and backward waves, and increase the natural frequencies of reflected waves. Comparing the effect of loads on clamped disks and splined disks reveal that the loads have a weak effect on eigenvalues of a splined disk in comparison with a clamped disk. It is also concluded that in-plane loads tend to merge two frequency paths in the neighborhood of “degenerate points” (in which two eigenvalues of the freely spinning disk are almost equal) for a clamped disk. However, for a free spinning disk, subjected to the same loads, the frequency loci cross over each other with no coupling. Therefore, the in-plane edge loads do not induce merge-type or flutter instability for a free splined disk, unlike a clamped disk. It was also found that the in-plane loads induce divergence instability in clamped disk, while it is not the case for a free splined disk. Numerical investigations of guided splined disks (a free splined disk is constrained by several springs over a certain area to represent the guides) show that the disk, subjected to edge loads, only suffers the flutter type instability. In other words, the disk is stable at minor critical speeds, and it only goes into instability when a forward wave and reflected wave merge

together due to presence of lateral constraints. This will be investigated in more depth in the next chapter by analyzing the energy induced into the disk by the in-plane edge loads.

Chapter 3: Instability Mechanism of a Spinning Splined Guided Disk Subjected to In-plane Edge Loads

3.1 Introduction

In order to provide physical insight into the effect of in-plane edge loads on the stability of a splined spinning disk, the rate of work done by the applied loads is considered. An expression for the rate of work done by the transverse components of the applied in-plane loads, and their interaction at the inner radius, is derived. The energy transfer from the in-plane edge loads to the transverse vibration of the disk is equal to the work done by the transverse components of the in-plane loads. If the total work in one cycle is zero, no energy transfers to the disk and system is stable. If the work done is positive, then since the system is constrained to maintain its constant speed, then the positive energy is transferred into lateral vibration and instability occurs.

3.2 Work Done by the Edge Loads (Formulation)

Consider an in-plane radial force F_r and an in-plane tangential force F_t acting on the outer edge of the disk and their interaction loads on the inner edge of the disk according to the Figure 2.3.

If we assume the transverse displacement of the disk with respect to a stationary coordinate system in polar coordinate as $w(r, \theta, t)$, and the rigid body tilting motions defined by θ_x and θ_y then the transverse velocity of point (r, θ) can be calculated as:

$$V(r, \theta, t) = \frac{\partial w}{\partial t} + \Omega \frac{\partial w}{\partial \theta} + r \left(\frac{\partial \theta_x}{\partial t} + \Omega \theta_x \right) - r \left(\frac{\partial \theta_y}{\partial t} + \Omega \theta_y \right) \quad (3.1)$$

Then the rate of work done by the edge forces in Figure 2.3 can be calculated as:

$$P_{F_r \text{ at Outer Edge}} = F_r \frac{\partial w}{\partial r}(b, \alpha, t). V(b, \alpha, t) \quad (3.2)$$

$$P_{F_t \text{ at Outer Edge}} = F_t \frac{\partial w}{b.\partial\theta}(b, \alpha, t). V(b, \alpha, t) \quad (3.3)$$

Note that the terms $F_r \frac{\partial w}{\partial r}(b, \alpha, t)$ and $F_t \frac{\partial w}{b.\partial\theta}(b, \alpha, t)$ define the transverse component of the F_r and F_t at the point of application (b, α) at time t .

The rate of work done by the inner edge loads can also be calculated as:

$$P_{F_r \text{ at Inner Edge}} = F_r \frac{\partial w}{\partial r}(a, \alpha, t). V(a, \alpha, t) \quad (3.4)$$

$$P_{\frac{a+b}{2a}F_t \text{ at Outer Edge}} = \frac{a+b}{2a} F_t \frac{\partial w}{a.\partial\theta}(a, \alpha, t). V(a, \alpha, t) \quad (3.5)$$

$$P_{\frac{b-a}{2a}F_t \text{ at Outer Edge}} = \frac{b-a}{2a} F_t \frac{\partial w}{a.\partial\theta}(a, \alpha + \pi, t). V(a, \alpha + \pi, t) \quad (3.6)$$

To calculate the work done in one revolution, the integration of the rate of the work is taken in one complete revolution as:

$$W_{F_r \text{ at Outer Edge}} = F_r \int_{\text{One Complete Revolution}} \left(\frac{\partial w}{\partial r}(b, \alpha, t). V(b, \alpha, t) \right) dt \quad (3.7)$$

$$W_{F_t \text{ at Outer Edge}} = F_t \int_{\text{One Complete Revolution}} \left(\frac{\partial w}{b.\partial\theta}(b, \alpha, t). V(b, \alpha, t) \right) dt \quad (3.8)$$

$$W_{F_r \text{ at Inner Edge}} = F_r \int_{\text{One Complete Revolution}} \left(\frac{\partial w}{\partial r}(a, \alpha, t). V(a, \alpha, t) \right) dt \quad (3.9)$$

$$W_{\frac{a+b}{2a}F_t \text{ at Outer Edge}} = \frac{a+b}{2a}F_t \int_{\text{One Complete Revolution}} \left(\frac{\partial w}{a \cdot \partial \theta} (a, \alpha, t) \cdot V(a, \alpha, t) \right) dt \quad (3.10)$$

$$W_{\frac{b-a}{2a}F_t \text{ at Outer Edge}} = \frac{b-a}{2a}F_t \int_{\text{One Complete Revolution}} \left(\frac{\partial w}{a \cdot \partial \theta} (a, \alpha + \pi, t) \cdot V(a, \alpha + \pi, t) \right) dt \quad (3.11)$$

The total work can be calculated by:

$$W = W_{F_r \text{ at Outer Edge}} + W_{F_t \text{ at Outer Edge}} + W_{F_r \text{ at Inner Edge}} + W_{\frac{a+b}{2a}F_t \text{ at Outer Edge}} + W_{\frac{b-a}{2a}F_t \text{ at Outer Edge}} \quad (3.7)$$

The terms $F_r \frac{\partial w}{\partial r}$, $F_t \frac{\partial w}{b \cdot \partial \theta}$, $\frac{F_t(a+b)}{2a^2} \frac{\partial w}{\partial \theta}$, and $\frac{F_t(b-a)}{2a^2} \frac{\partial w}{\partial \theta}$ are the transverse components of outer and inner edge loads, and $V(r, \theta, t)$ is the lateral velocity of a point on the disk at time t, at position of (r, θ) . Therefore, P is the rate of work done by the lateral components of the edge loads. If there is no deflection in the disk, then the lateral component of the edge loads are zero and no energy is transferred into the disk. If there is a deflection in the disk, and the lateral components of the loads (including the inner interaction loads) are in phase with $V(r, \theta, t)$ then the work done is positive, and energy will induce into the disk. In this situation, because the disk is spinning at a constant speed, then the positive energy has to be transferred into lateral vibration and instability will occur. If the lateral component of the loads are out of phase with $V(r, \theta, t)$ the work done is negative, and energy will be transferred out the disk. Since the disk is constrained to have constant speed, the disk centers itself and moves to the stable condition.

3.3 Numerical Results of Energy Induced in the Disk by Edge Loads

For the guided splined disk, under investigation, the rate of energy is computed at different speeds. The results are computed for three different speeds: a) At first minor critical speed (42Hz), b) At a super critical speed (e.g. 50Hz), c) At a flutter instability speed (e.g. 53Hz). The disk is subjected to a radial load of $F_r = 3.6 \frac{D}{b} = 1000N$, and a tangential load of $F_t = 3.6 \frac{D}{b} = 1000N$ at $= 45^\circ$, and the inner interaction edge loads.

Figure 3.1 shows the rate of work at the three cases ((a), (b), and (c)). And the disk is subjected to both the radial and tangential forces. The results illustrate that at flutter speed the rate of work done by the in-plane edge loads is positive, therefore, instability is induced at flutter speed.

Figure 3.1 Rate of Work Done by the Edge Loads, at Rotating Speed (a) 42Hz, (b) 50Hz, (c) 53Hz

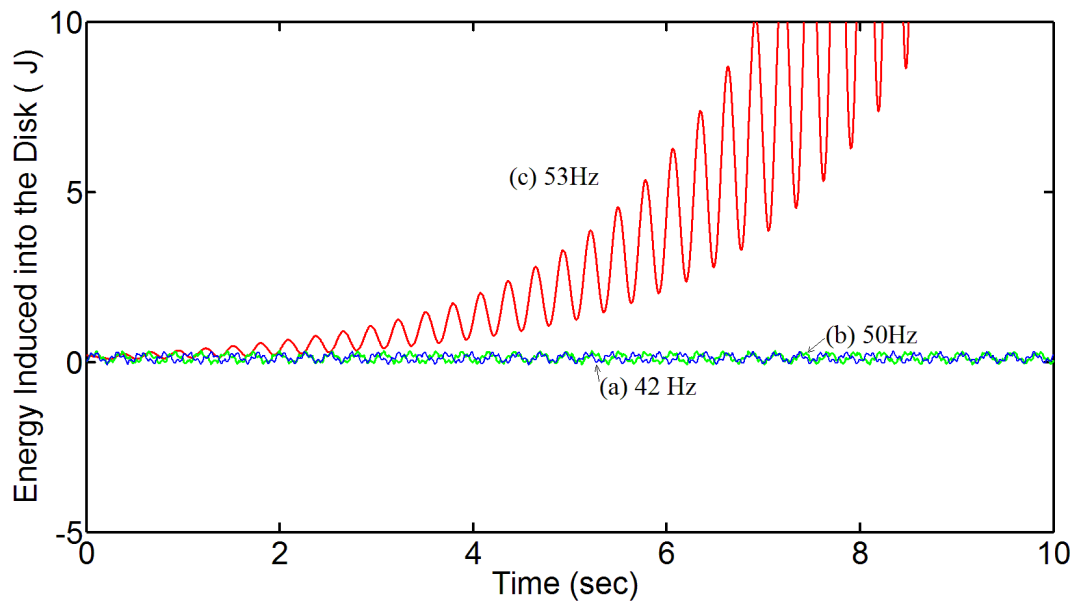
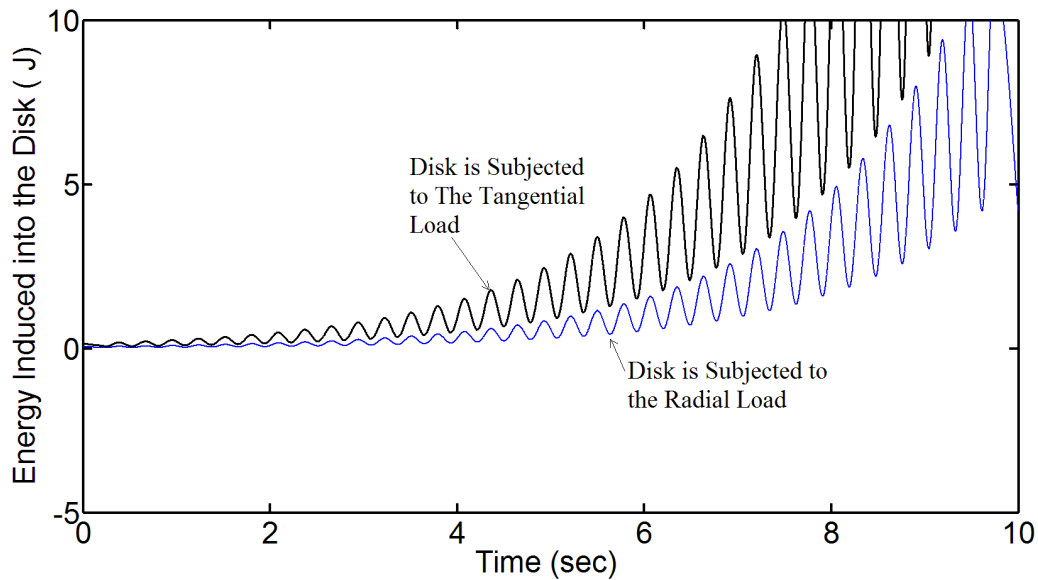


Figure 3.2 shows the rate of work at a flutter instability speed ($\Omega = 53\text{Hz}$), when the disk is subjected to the radial load, and the tangential load, separately. The results indicate that the rate of work done by the tangential load is higher than the rate of work done by the radial load of the same magnitude. It can be concluded that the effect of the in-plane tangential load on the instability of the disk is greater than the effect of the in-plane radial load.

Figure 3.2 Rate of Work Done by the Tangential and Radial Edge Loads, Disk Running at a Flutter Instability Speed ($\Omega = 53\text{Hz}$)



3.4 Summary

In this chapter the rate of work done by the applied loads were formulated and numerically computed. The following main two conclusions were reached:

- The rate of work done by the in-plane edge loads is positive at flutter speeds for guided splined disks, which induces instability into the system.

- The effect of the tangential in-plane edge loads on the instability of guided splined disks is greater than the effect of radial edge loads.

Chapter 4: Experimental Investigations of Idling and Cutting Characteristics of a Splined Guided Saw

4.1 Introduction

This chapter provides further insights into the dynamic behavior of spinning disks by reporting on the results of experimental studies, conducted by the author.

The number of variables that affect cutting performance at high speeds is large and their interaction is complex. Such factors are blade speed, blade geometry, tooth geometry, blade flatness, temperature distribution in the blade, depth of cut, wood characteristics, guide size and location. However, particular interest here is to see how the idling results can be used to predict the stable region of the blade for cutting.

Experimental tests facilities were developed which enable conducting idling and cutting tests. Experimental observations of idling and cutting tests for a guided circular saw blade are used to examine the dynamic characteristics of a guided spline saw.

First, idling tests results are presented for a guided spline saw blade. Then, the results of cutting tests for the same blade are presented. From idling results the minor critical speed and the start of flutter instability were identified. Then, cutting tests were conducted at about critical speed, a super critical speed, and at a flutter instability speed.

The physical properties of the blade under investigation are summarized in Table 4.1:

Table 4.1 Properties of the Blade under Investigation

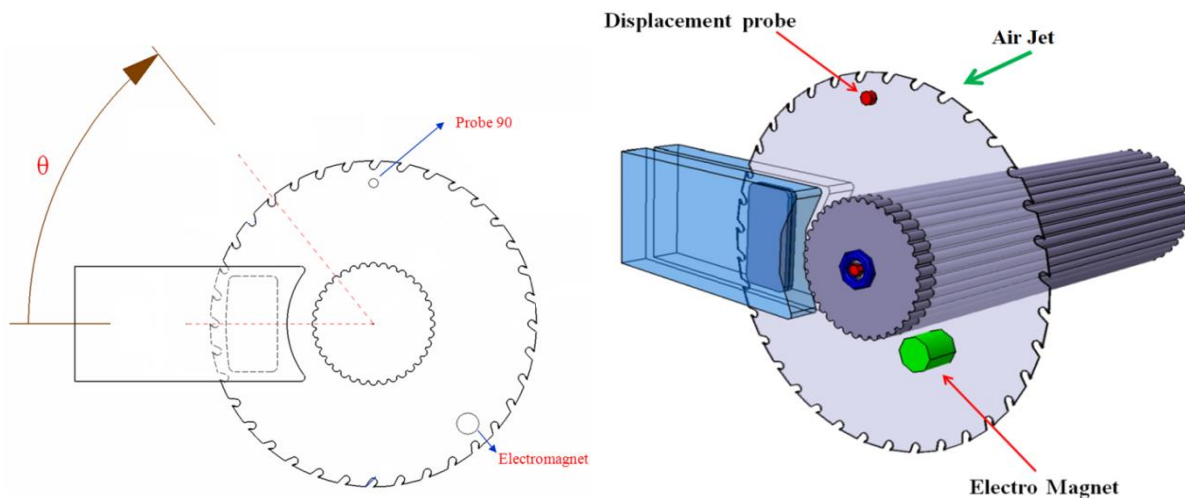
Physical Property	Value
Outer Diameter (Rim)	430mm (17in)
Inner Diameter (Eye)	150mm (6in)
Thickness	1.5mm (0.060in)
Number of teeth	40
Density	7800 ($\frac{\text{Kg}}{\text{m}^3}$)
Young's Modulus	203(G. Pa)
Poisson's ratio	0.3

4.2 Experimental Tests Results

4.2.1 Idling Tests

A schematic of the experimental idling setup is presented in Figure 4.1. In order to measure the blade deflection, a non-contacting inductance probe was used. Electromagnetic excitation was used to provide low level white noise excitation over the frequency range of 0–100 Hz. In order to apply lateral force to the blade during tests an air jet nozzle with a constant pressure were used. Results were obtained by measuring the vibration responses of the blade at the location of the displacement probe as the rotation speed was ramped up from 0 RPM to 4,000 RPM at a constant rate over 600 s.

Figure 4.1 Schematic of the Experimental Setup



Figures 4.2 and 4.3 show the variation of excited frequencies of the disk as a function of rotation speed for a free spinning spline saw blade and a guided spline saw blade respectively. There are imperfections in the balance and interaction of the components of most practical rotating machines. As a result of these imperfections, rotating parts of machines generate vibration. Common sources of such vibrations arise due to mechanical looseness, mass unbalance, eccentricity, misalignments, bent shaft, pulleys, external forces, and rubbing. These faults usually yield vibrations of 1X, 2X, 3X, and higher order harmonics of the rotation. Further sub-harmonic levels of vibration such as $X/2$, $X/3$, ... of rotation speed may occur as illustrated in Figures 4.2 and 4.3.

Figure 4.2 indicates that the frequency of the first two modes reaches to zero at about 2400rpm and 3200rpm.

Figure 4.2. Variation of Excited Frequencies with Rotation Speed for a Saw Blade with no Constraint

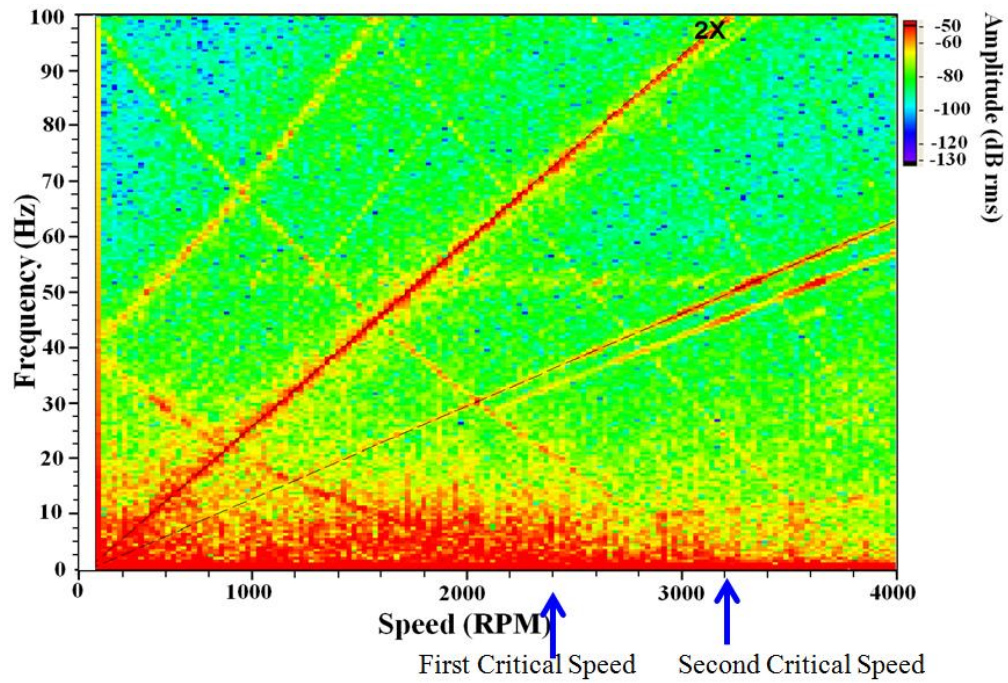
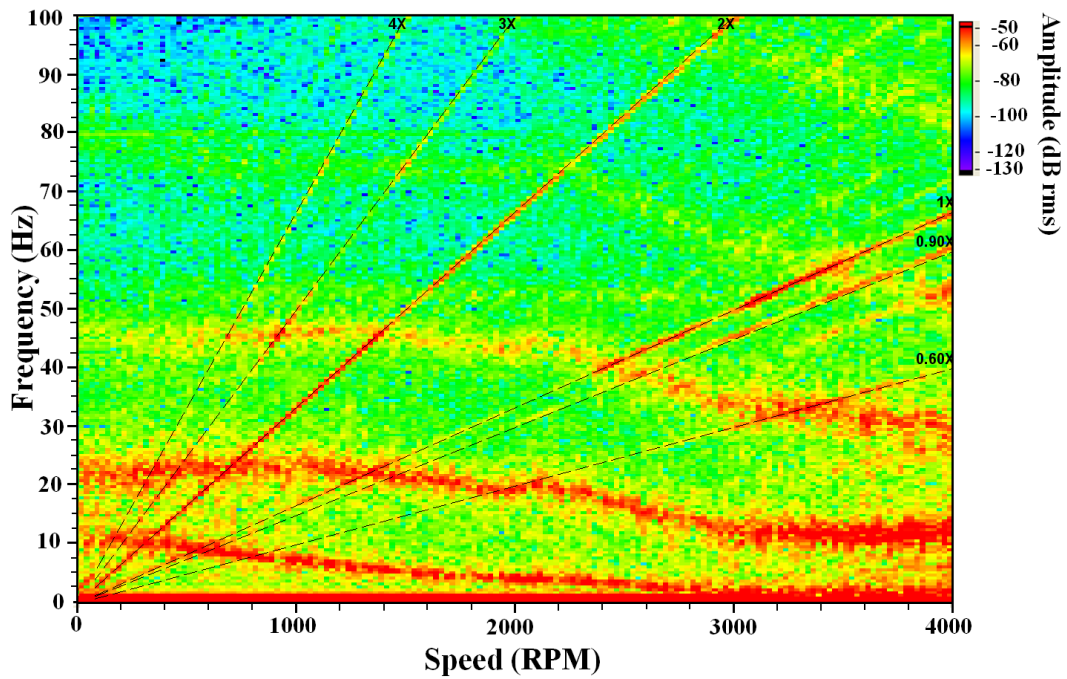


Figure 4.3 Variations of Excited Frequencies as a Function of Rotation Speed, Guided Spline Saw



The experimental idling results of the guided splined saw (Figure 4.3) indicate that the lowest frequency path reaches to zero at about 3200rpm which is identified as the first minor critical speed. The start of flutter for this blade is about 3800rpm.

4.2.2 Cutting Tests

Figure 4.4 shows the schematic of the cutting test setup. Cutting tests were conducted at 3200rpm (about the first minor critical speed), 3600rpm (a super critical speed), and 4000rpm (a post-flutter instability speed). The depth of cut was chosen to be 130mm (stack of 3 Hemlock boards). The feed speeds were chosen to provide the bite per tooth of 1mm with the gullet feed index of $G.F.I. = 0.45$ (See Appendix F for details). After each cut, the cutting profile was obtained by laser scanning the surface of the cut 20mm below the upper edge of the board. Each test was repeated 5 times with 5 different cants. Table 4.2 summarizes the rotation and feed speeds.

Figure 4.4 Schematic of Cutting Test Setup

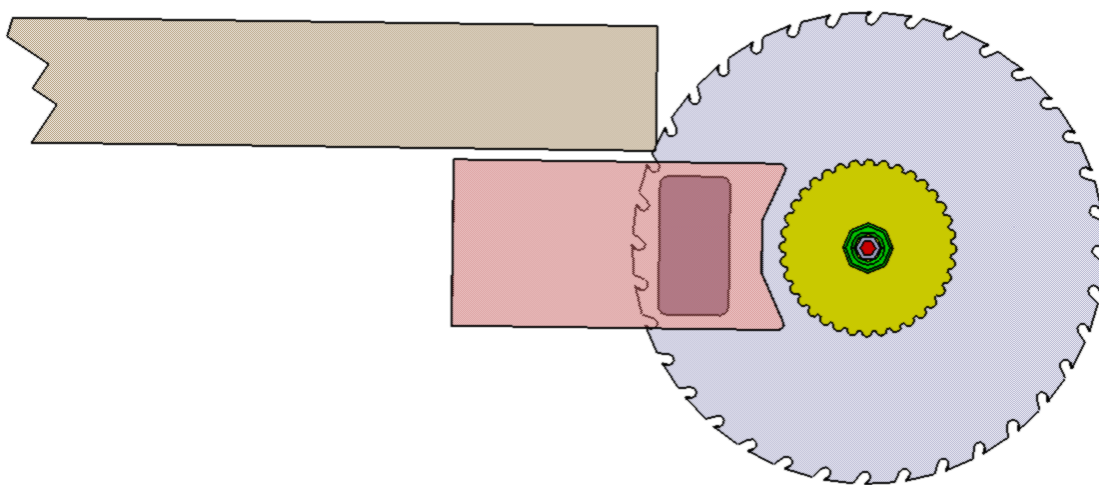


Table 4.2 Cutting Tests Rotation Speed, and Feed Speed

Test No.	Rotation Speed (RPM)	Feed Speed (m/sec)	Idling Condition
1	3200	2.1	First Critical Speed
2	3600	2.4	Super-critical Speed
3	4000	2.6	Flutter Instability

Figures 4.5 - 4.7 show the cutting profiles for the cutting tests #1-3 respectively. The graphs indicate that cutting tests at speeds below the flutter instability speed (Test 1 and 2) resulted in an acceptable cutting performance (deviation less than 2mm). Cutting at a flutter instability speed resulted in large deviations (more than 15mm).

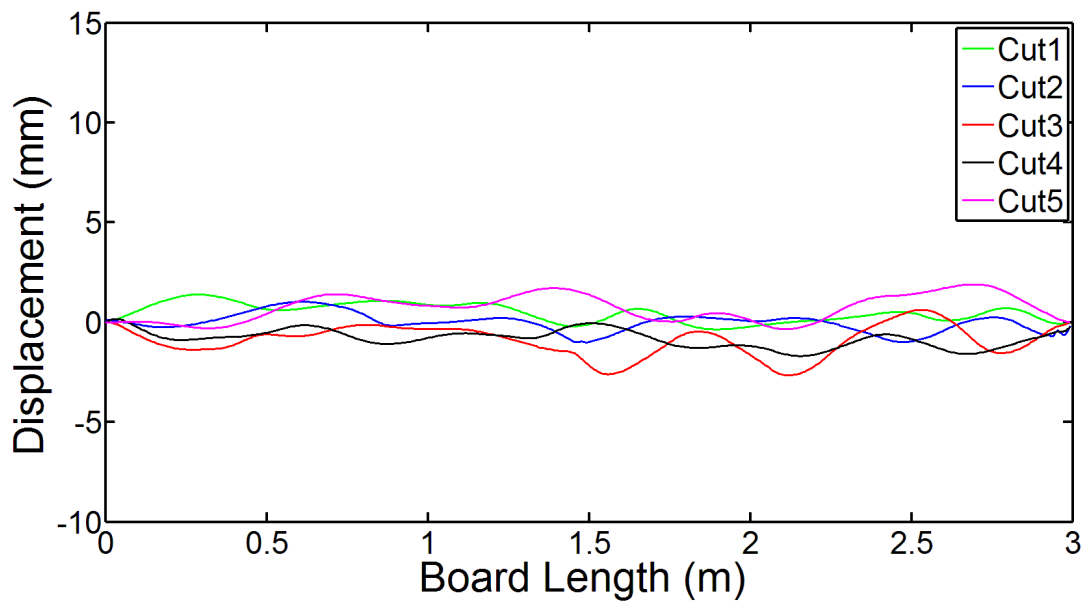
Figure 4.5 Cut Profile for Test 1, Cutting at 3200rpm (Critical Speed)

Figure 4.6 Cut Profile for Test 2, Cutting at 3600rpm (A Super Critical Speed)

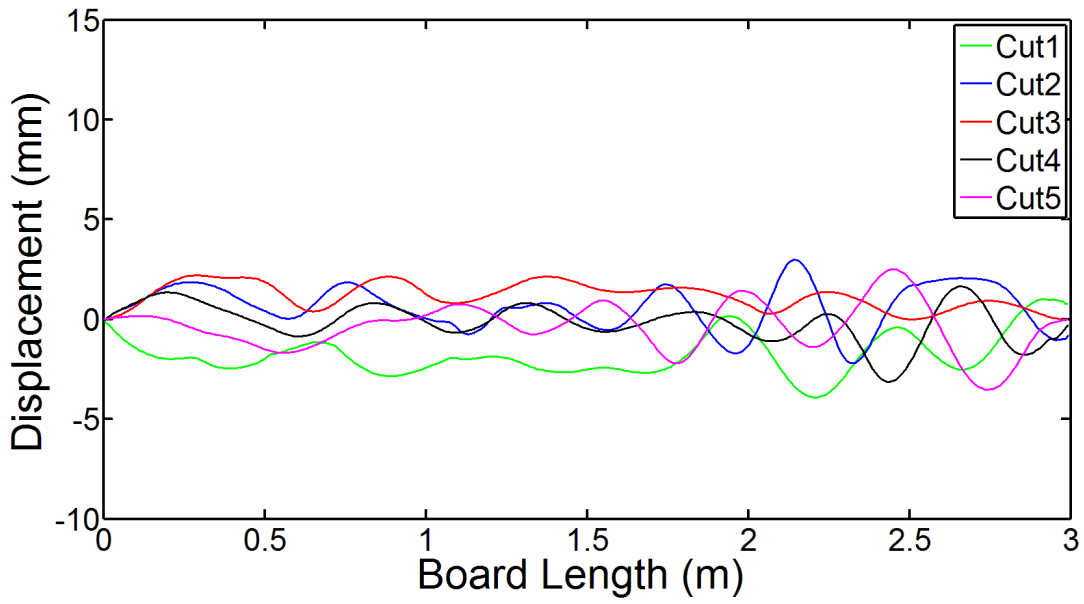
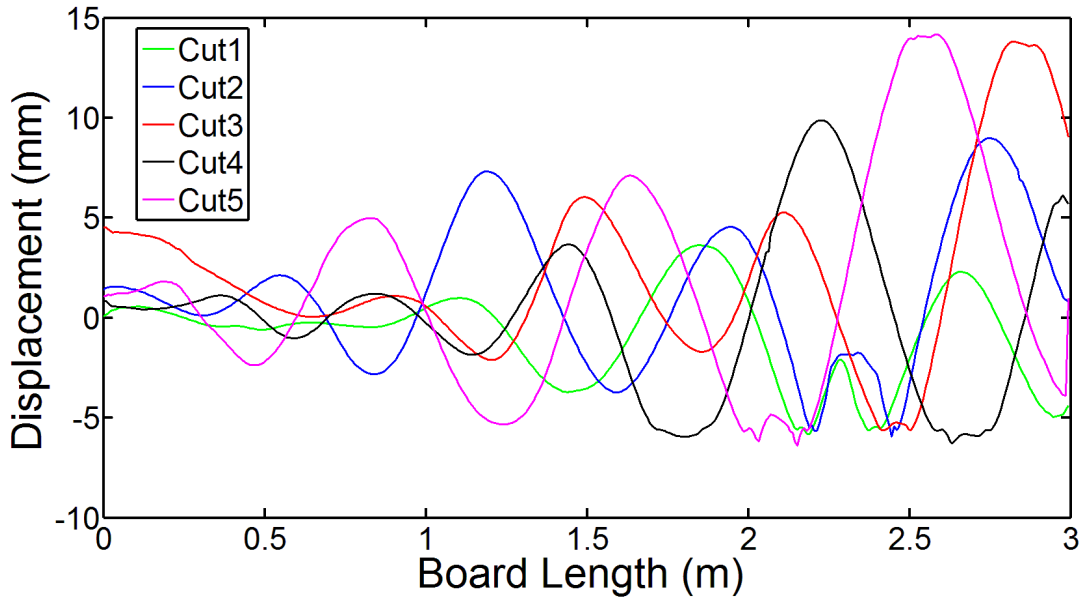


Figure 4.7 Cut Profile for Test 3, Cutting at 4000rpm (A Flutter Speed)



4.4 Summary

Idling and cutting tests were conducted for a guided circular splined saw. From idling results, the first critical speed and the initiation of flutter instability speeds were obtained. Then, cutting tests were conducted at the critical speed, at a super-critical speed, and at a flutter instability speed. The results indicated that cutting at speeds below the flutter instability, even at the critical speed, resulted in stable operation of the saw blade. Cutting at flutter instability resulted in unstable operation of the saw and cuts with large deviation (about 10 times the thickness of the blade).

In conclusion, the idling results can be used to predict the stable operation speeds of a splined saw. Based on the experimental results, obtained in this study the maximum stable operation speed is the flutter speed. This speed may be identified from an idling test.

Chapter 5: Flutter Speed Chart for Guided Splined-Arbor Saws

5.1 Introduction

Choosing an optimum saw blade configuration for primary wood breakdown is a complex problem. There are many interconnected factors which need to be considered. Such factors include: blade diameter, arbour size, blade thickness, teeth number and geometry, gullet area, and a stable operation speed. Blade diameter is constrained by the maximum depth of cut and the arbour size. Two common arbour diameters are 6 inches and 8 inches which correspond to the nominal inner diameter of saw blades. (Also known as “Eye#3” and “Eye#4” respectively). After determining the blade diameter, and eye size, the next step is to choose optimum blade thickness. Choosing a thick blade results in the reduction of transverse vibrations of blade and increases the maximum stable operation speed. However, this is at the expense of increasing the cutting forces and power consumption. Moreover, a thicker blade means bigger kerf and increased saw dust wastage. The main intention of this chapter is to provide primary practical guide lines for sawmills to choose optimum blade diameter, eye size, blade thickness, and a stable rotation speed.

It was shown, both analytically and experimentally, in previous chapters, that cutting at speeds below the flutter instability speed results in stable operation of the saw blade. It was seen that cutting above the flutter instability speed results in unstable operation of the saw and cuts with large deviation.

In this chapter, experimental run-up tests of several guided splined disks and saws of different sizes are presented, and the flutter instability zones are identified. The results indicate

that flutter instability occurs at speeds when a backward travelling wave of a mode meets a reflected wave of a different mode. Sometimes, the system cannot pass a flutter zone, and transverse vibrations of the disk lock into that flutter instability zone. The maximum stable operating speed of the rotating splined disk is defined as the initiation of a flutter which the system cannot pass.

Using the equations of motion for guided splined disks (developed in Chapters 1 and 2), the imaginary and real part of eigenvalues is computed and the flutter instability zones are defined. The results show that the mathematical model can accurately predict the flutter instability zones measured in the experimental tests. However, in the case where, in practice, the system cannot pass a flutter zone, the linear model fails to exhibit such behaviour. In other words, while the model indicates an unstable zone, in practice, it may not be possible to pass through the flutter zone by further increasing rotation speed.

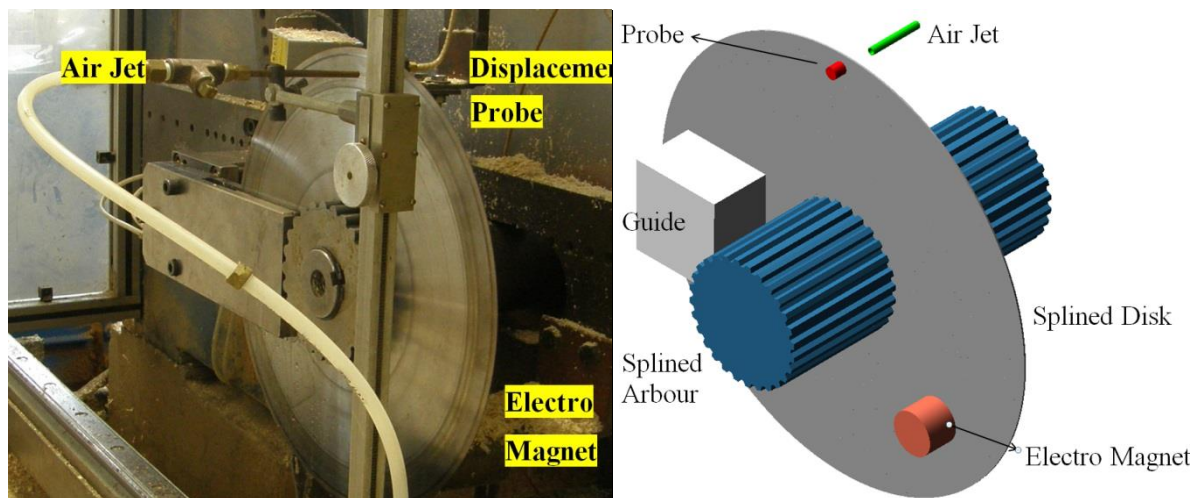
It should be noted that the mathematical model does not incorporate the effect of stress distributions of the type and magnitude that are caused by roll tensioning of the blade (a universal procedure in primary breakdown sawmills [38]). All the calculations are based on non-tensioned blades. The roll tensioning adds approximately 5-10% to the numerical results of the flutter speeds. This difference leaves users with a safe margin for operation.

In this chapter, experimental idling results for several non-tensioned and tensioned blades are presented. Then numerical results of flutter instability speed computation for the same sized blade are presented. The experimental and numerical results are compared and discussed. Then the effect of the geometrical parameters of the blade on the initiation of flutter instability is analyzed.

5.2 Experimental Measurements of Idling Response of Guided Splined-Arbor Saws

Experimental test facilities were developed which enable the measurement of natural frequencies of guided splined saws of various sizes as a function of rotation speed. The experimental setup is presented in Figure 5.1. To measure the disk deflection, a non-contacting inductance probe was used. Electromagnetic excitation was used to provide white noise excitation over frequency range 1-100Hz. To investigate the dynamic characteristics of a rotating disk when subjected to the effect of a stationary lateral constant force, an air jet was used. The magnitude of the air jet force was kept at a constant value by keeping a constant air pressure. Results were obtained by measuring the vibration responses of the disk at the location of the displacement probe as the speed is ramped up from 0 RPM to 4,000 RPM at a constant rate over 600 s.

Figure 5.1 Experimental Idling Tests Setup



Idling tests were conducted for several blades of different sizes. The experimental tests were conducted for non-tensioned and roll tensioned blades of various sizes. Here as an example the results are present for 5 different blades which are listed in Table 5.1.

Table 5.1 List of Blades under Experimental Investigations

No.	Blade Dimension as: “Blade Diameter-Eye Size-Thickness” (in)	Condition
1	17-6-0.040	Non-Tensioned Disk
2	20-6-0.080	Non-Tensioned Disk
3	28-8-0.115	Non-Tensioned Saw Blade
4	30-8-0.125	Roll Tensioned Saw Blade
5	34-8-0.145	Roll Tensioned Saw Blade

Figure 5.2 shows the idling results of the blade 28-8-0.115. (The results for other blades are presented in Appendix H). Figure 5.2 shows the deflection of the disk measured by the displacement probe during run-up from 0-3600rpm at constant acceleration (note that the test had to be stopped at 3600rpm due to very large transverse vibrations of the disk). The variation of the excited frequencies of the disk, as a function of rotation speed, was computed and plotted in a form of frequency-speed color-map (Figure 5.3). Frequency color maps of the power spectrum illustrate the variation of disk frequencies with rotation speed. It illustrates the energy of the signal at each speed and frequency with a color spectrum.

From the time domain and color-map two general characteristics of the system can be observed. As the color map indicates, the frequencies (as measured by a space fixed observer) of each mode decrease as the rotation speed increases. At minor critical speeds the frequency of a mode reaches zero. The experimental results show that the blade suffers two minor critical speeds at about 1500rpm, and 2100rpm. It experiences initiation of lock-in flutter vibrations at about 2500rpm. Flutter occurs at super-critical speeds where a reflected wave frequency coincides with

a backward travelling wave frequency. For example, figure 5.3 illustrates several points where reflected waves of mode 2 and 3 meet the backward waves of mode 2, 3, and 4. The results indicate that by increasing the rotation speed system could pass these flutter zones. But, at a speed about 2500rpm, when the reflected wave of mode 1 reaches the backward wave of mode 4 the system cannot pass the flutter speed zone. We define the term “locked-in flutter instability” where the system cannot pass a flutter zone. After this speed there are several lock-in frequency paths. The maximum stable operation speed of a guided splined disk is defined as the start of a locked-in flutter. One possible reason is that when system reaches to this flutter, the deflection of the system is large so that system behaves non-linearly.

Figure 5.2. Deflection of Blade 28-8-0.115, during Idling Run-up from 0-3600rpm, Measured by Displacement Probe

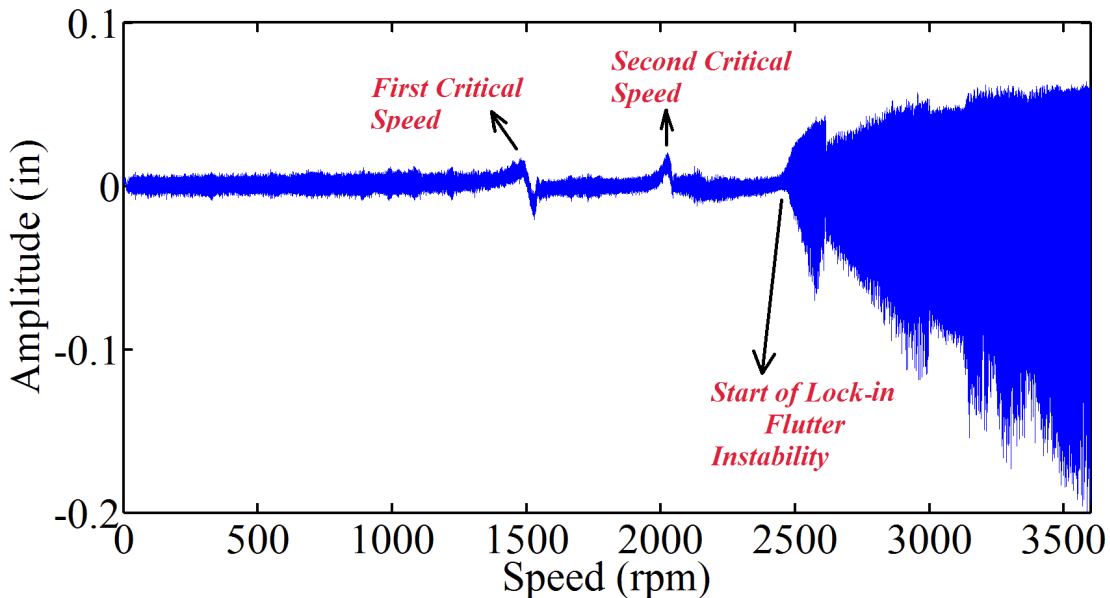
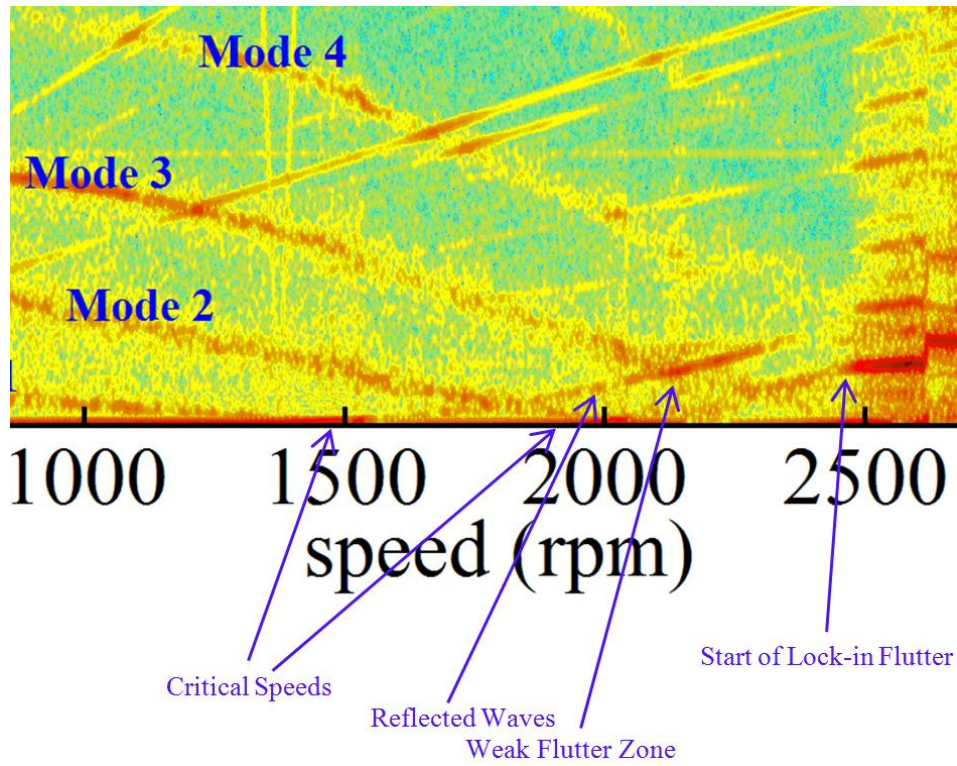
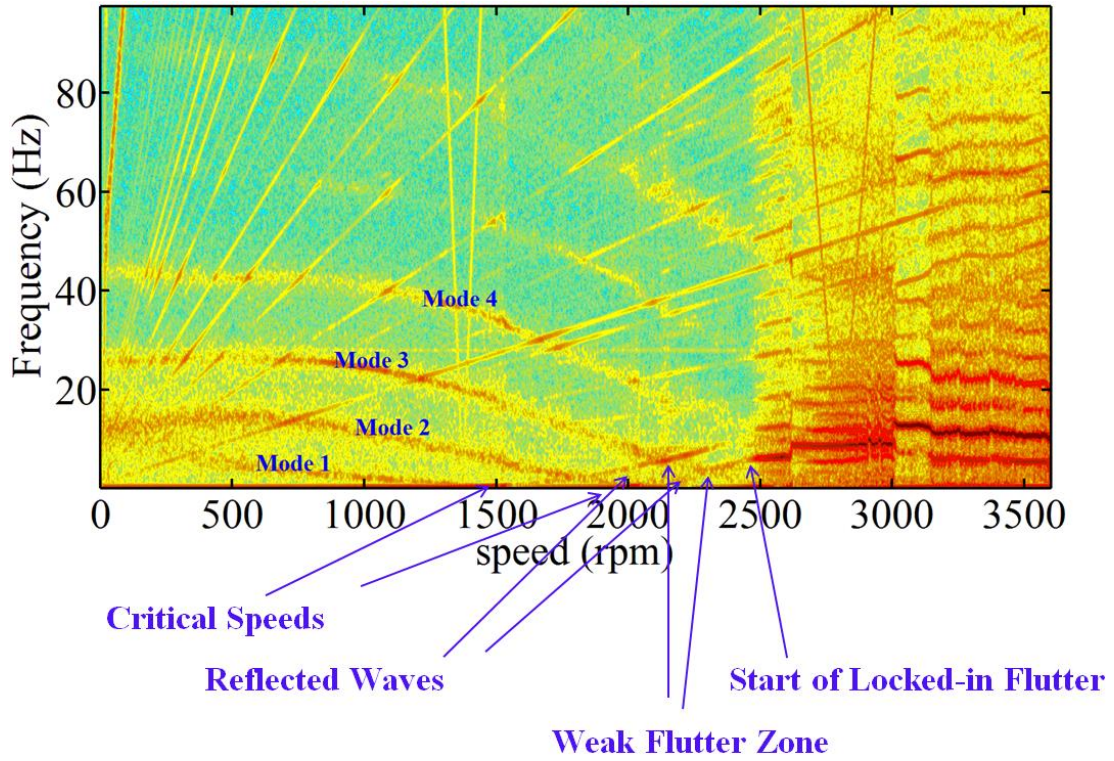


Figure 5.3. Variation of Excited Frequencies of the Disk as a Function of Rotation Speed



5.3 Numerical Computation of Eigenvalues of Guided Splined-Arbor Saws

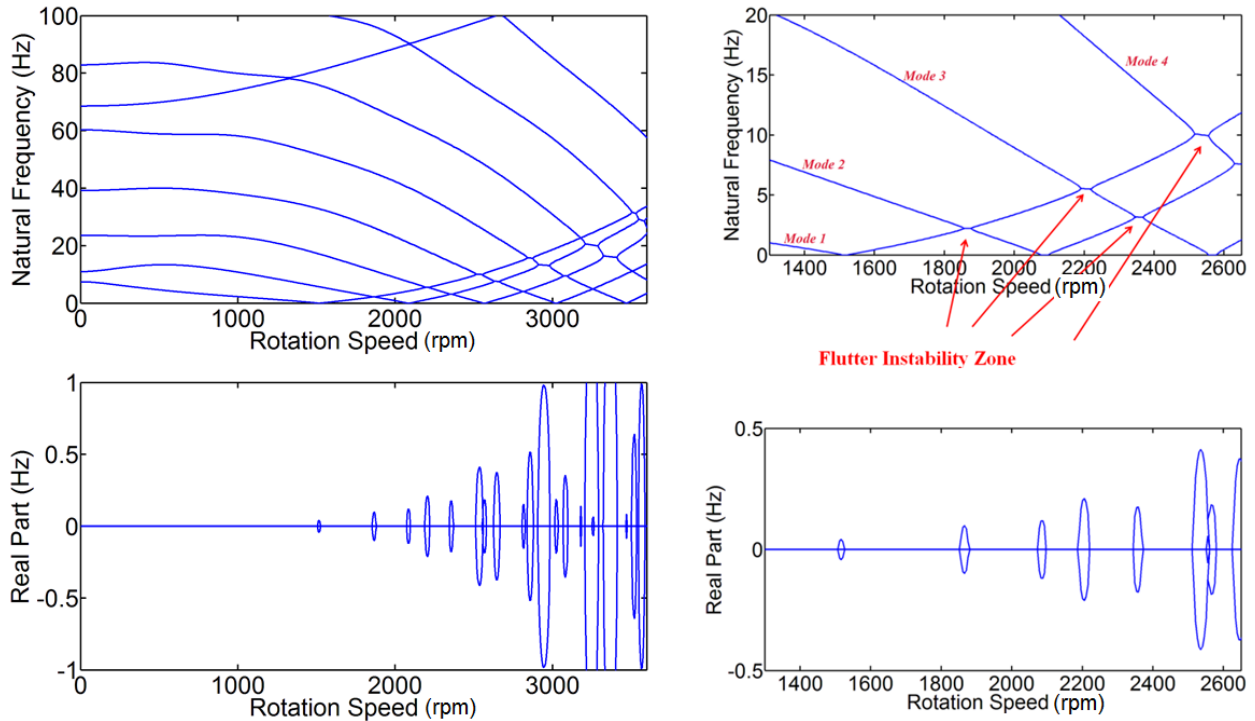
In this section, the imaginary and real parts of the eigenvalues are computed numerically for a disk with physical properties summarized in Table 5.2. The disk is constrained by 16 lateral springs each of stiffness $k = 10^5 \frac{N}{m}$ distributed over a 200×200 mm square area which represents the guides.

Table 5.2 Properties of the disk under Investigation

Physical Property	Value
Outer Diameter (Rim)	710mm (28in)
Inner Diameter (Eye)	203mm (8in)
Thickness	2.9mm (0.115in)
Density	7800 ($\frac{Kg}{m^3}$)
Young's Modulus	203(G. Pa)
Poisson's ratio	0.3

Figure 5.4 shows the eigenvalues of the disk as a function of rotation speed. Comparing the natural frequency graph predicted by the numerical analysis and those obtained from experimental results (the color map Figure 5.3) indicates that there is a good agreement between the numerical results and experimental results. From the numerical results the start of flutter instability which initiates by the interaction between mode 4 and reflected wave of mode 1 is 2510rpm, which is about the start of lock-in flutter speed obtained from the experimental results during run-up tests.

Figure 5.4 Imaginary and Real Parts of Eigenvalues of the Guided Splined Disk



The color map (Figure 5.3) however illustrates other excited frequencies in the system which analysis did not show. This is due to the fact that there are imperfections in the balance and interaction of the components of most practical rotating machines. As a result of these imperfections, rotating parts of machines generate vibration. Common sources of such vibrations arise due to mechanical looseness, mass unbalance, eccentricity, misalignments, bent shaft, pulleys, external forces, and rubbing. These faults usually yield vibration levels with harmonic of 1Ω , 2Ω , 3Ω ,,, and sub-harmonic levels of vibration such as $\Omega/2$, $\Omega/3$, and ... of rotation speed which can be seen in the color map. If the frequency of excitation generated by a rotating part coincides with the natural frequencies of the rotating blade, resonant interaction can be expected.

5.4 Verification of Numerical Results

Table 5.3 compares the results of initiation of the lock-in flutter speed computed numerically with that obtained experimentally.

Table 5.3 Start of Flutter Instability Speeds for the Blades under Investigations

No.	Blade Dimension as: “Blade Diameter-Eye Size-Thickness” (in)	Start of Flutter		Difference (%)
		Measurement (RPM)	Numerical Result (RPM)	
1	17-6-0.040	2750	2650	-3
2	20-6-0.080	3600	3450	-4
3	28-8-0.115	2500	2510	-1
4	30-8-0.125 (Roll Tensioned)	2450	2175	-11
5	34-8-0.145 (Roll Tensioned)	2150	1910	-11

As may be seen from Table 5.3, the predicted flutter instability speeds are less than measured flutter speeds. This may be due to the existence of tensioning in the blades. Even for the nominally non-tensioned blades under investigation there might be little tensioned in the blade due to hammering and leveling of the blades. However, since it is a common practice in a sawmill to roll-tension blades, the numerical prediction of flutter speed leaves us with about 10% safety margin for stable operation speed.

5.5 The Effect of Geometrical Properties of the System on the Start of Flutter Instability Speeds

A non-Dimensionalized analysis of the speed of a spinning disk indicates that the start of flutter has a linear relationship with thickness (for details see Appendix F):

$$\Omega = \sqrt{\frac{D}{\rho h b^4}} \Omega^* \quad (5.1)$$

Whereas D is the flexural rigidity:

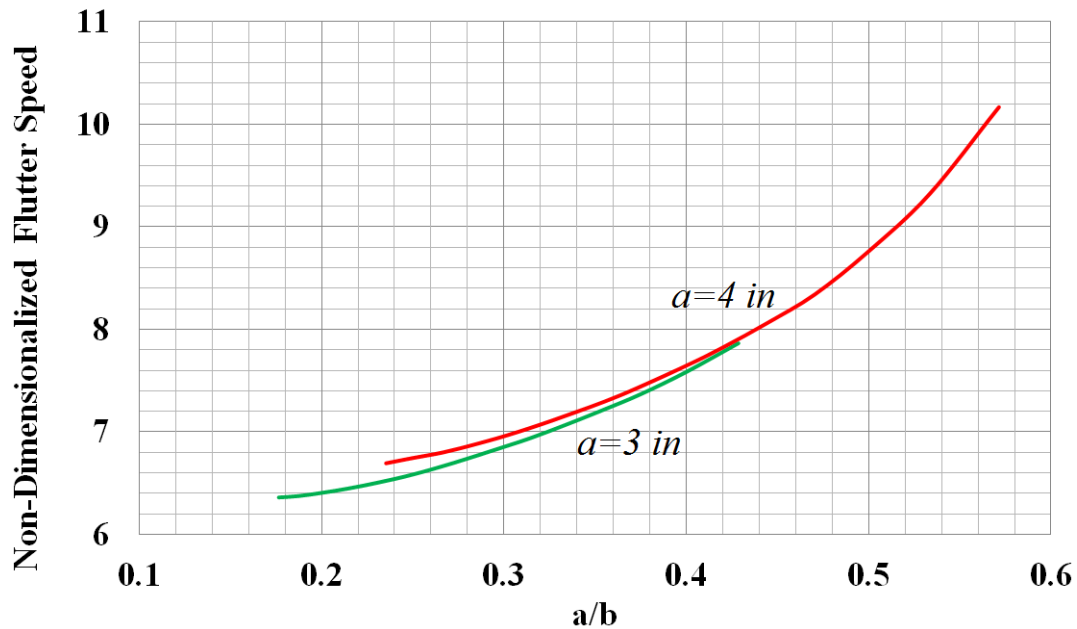
$$D = \frac{E h^3}{12(1-\nu^2)} \quad (5.2)$$

Therefore:

$$\Omega = \sqrt{\frac{E}{12\rho(1-\nu^2)}} \frac{h}{b^2} \Omega^* \quad (5.3)$$

Ω^* is the non-dimensionalized rotation speed. Ω^* is a function of non-dimensional value of a/b (where a is the inner radius and b is the outer radius of the blade).

The Figure 5.5 shows the non-dimensionalized initiation of flutter speed as a function of a/b for $a = 75\text{mm}$ (3 in) and $a = 100\text{mm}$ (4 in) .

Figure 5.5 Non-Dimensionalized Flutter Speeds for $a=3\text{in}$ (Eye#3) and $a=4\text{in}$ (Eye#4)

For larger diameter blades (smaller a/b), the effect of eye size is more pronounced. The graph indicates that using the larger eye size increase the start of flutter instability speeds. It should be noted that increasing the eye size is at the expense of reducing the depth of cut. In addition, smaller eye size results in increasing the splined forces and this can increase the stresses in the blade. Therefore, when designing for optimum size blades, we are constrained by the depth of cut, plate thickness, eye size, and maximum operation speed which is the flutter speed.

5.6 Flutter Instability Speeds Charts

To provide primary practical design guide lines for sawmills the initiation of flutter speeds are computed for different blade diameters. In wood primary breakdown industry blades diameter usually varies from 14-34 inches depend on the depth of cut. The start of flutter instability speeds were computed and tabulated for different blade thickness. The results are also plotted in chart format.

Table 5.4 summarizes the flutter instability speeds for guided splined-arbor saws. Figure 5.5 and Figure 5.6 is the graphical illustration of the same results.

Table 5.4 Flutter Speeds for Guided Splined-Arbor Saws

Plate Thickness	Eye Size	Saw Blade Diameter (in)													
		14	15	16	17	18	19	20	22	24	26	28	30	32	34
0.040 in	#3	4100	3440	2940	2550	2250	2000	1760	1460	1210	1010	875	765	665	595
	#4	5800	4505	3720	3130	2685	2335	2020	1570	1300	1080	935	810	710	625
0.050 in	#3	4960	4160	3560	3090	2720	2410	2120	1740	1450	1210	1045	915	795	710
	#4	6800	5295	4385	3695	3100	2730	2410	1895	1560	1295	1125	980	855	755
0.060 in	#3	5820	4880	4180	3625	3190	2820	2480	2035	1685	1405	1210	1055	920	815
	#4	7780	6130	5080	4280	3625	3190	2815	2220	1820	1510	1310	1135	990	875
0.070 in	#3	6690	5620	4810	4165	3660	3240	2850	2330	1920	1610	1385	1205	1050	930
	#4	8820	7085	5800	4900	4155	3660	3230	2545	2085	1730	1490	1285	1120	990
0.080 in	#3	7575	6360	5440	4710	4140	3660	3230	2620	2165	1820	1560	1355	1180	1045
	#4	9880	7860	6535	5520	4695	4130	3640	2875	2355	1950	1670	1445	1255	1105
0.090 in	#3	8450	7100	6070	5250	4620	4080	3600	2930	2420	2030	1740	1510	1320	1160
	#4	10975	8740	7275	6150	5245	4600	4060	3210	2625	2170	1855	1600	1390	1225
0.100 in	#3	9320	7830	6685	5790	5065	4470	3980	3215	2655	2235	1910	1653	1446	1278
	#4	12050	9620	7950	6705	5780	5040	4440	3530	2885	2405	2040	1755	1530	1345
0.110 in	#3	10180	8550	7320	6340	5570	4920	4350	3540	2920	2450	2100	1820	1590	1400
	#4	13135	10480	8750	7400	6315	5550	4890	3870	3165	2625	2235	1925	1670	1470
0.120 in	#3	11020	9260	7930	6880	6050	5350	4710	3835	3160	2650	2280	1975	1770	1520
	#4	14220	11320	9475	8010	6835	6030	5320	4200	3435	2850	2420	2085	1810	1590

Figure 5.6 Flutter Instability Speeds Charts, Eye#3

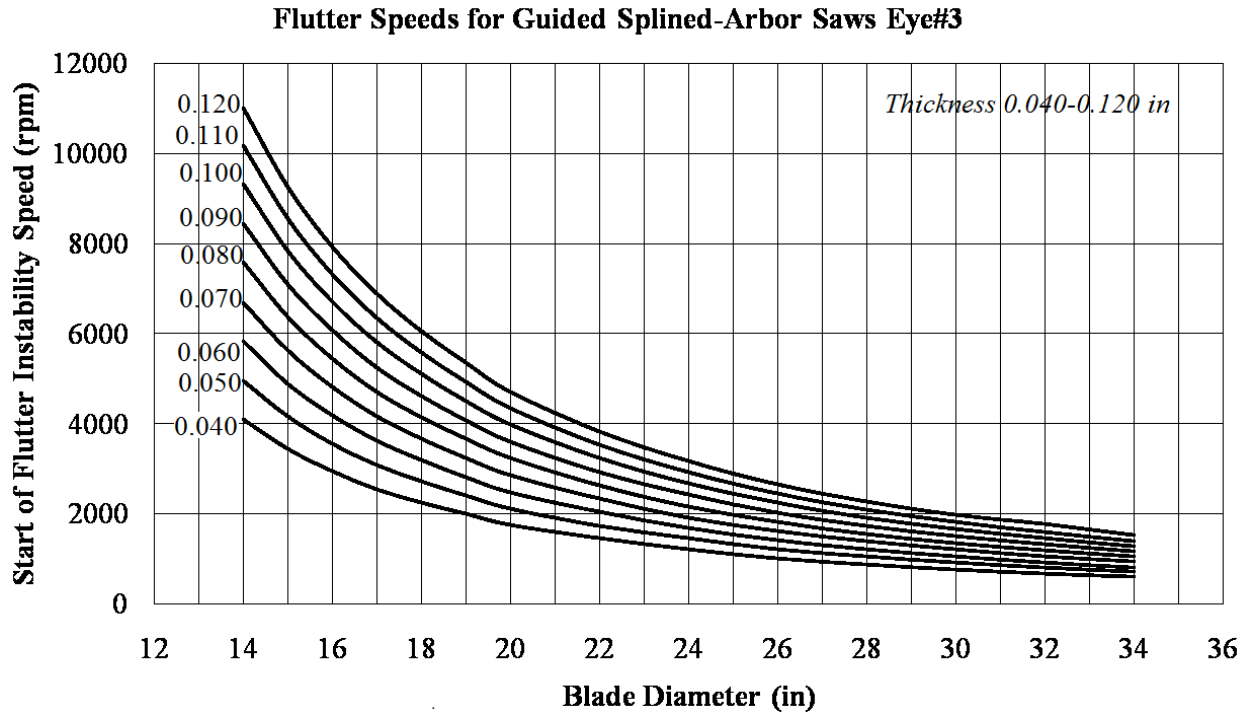
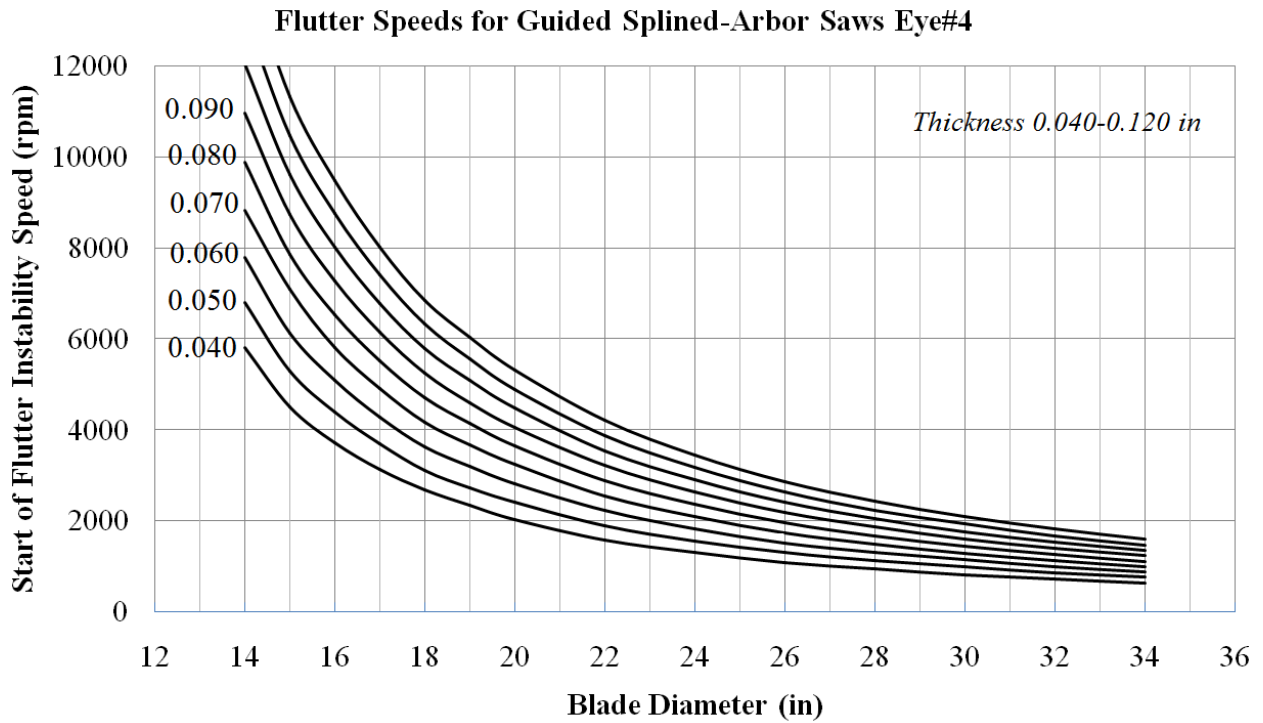


Figure 5.7 Flutter Instability Speeds Charts, Eye#4



5.7 Conclusion

Experimental run-up tests of a guided splined disk indicate that flutter instability happens at speeds when a backward wave of a mode meets a reflected wave of another mode at supercritical speeds. As the rotation speed increase system may be able to pass a flutter zone, but there is a speed where system cannot pass a flutter and transverse vibrations of the disk lock into that flutter instability zone.

The governing linear equations of transverse motion of a spinning disk with a free inner boundary condition and constrained from lateral motion by linear springs can be used to predict the flutter instability zones. However, this mathematical model fails to predict the behaviour of the system when it locks into a flutter speed. One possible explanation is the geometrical non-linearity of the system at post-flutter speeds due to large transverse deflection of the disk. Therefore, for further analyses of the guided splined disk study of non-linear equations of motion should be undertaken.

Flutter speed charts were developed and presented in this chapter. The charts can be used to determine the maximum stable operation speed of a guided splined saw. These results are based upon tests conducted in a laboratory environment. Situations in the mills may not be ideal and this may result in mills not being able to duplicate these results. Therefore, mill trials are necessary in order to see if these results can be duplicated. The results can be used as a measure of how close a mill is to meet optimal conditions.

Chapter 6: Conclusion

6.1 Summary and Conclusion

The main contributions of this thesis can be summarized as:

(i) The effect of in-plane edge loads on the stability and natural frequencies of a spinning disk

The governing non-damped linear equations of transverse motion of a spinning splined disk were derived. Rigid body translational and tilting degrees of freedom were included in the analysis. The disk was subjected to conservative in-plane edge loads at the outer and inner boundaries. The numerical solutions of these equations were used to investigate the effect of the loads and constraints on the natural frequencies, critical speeds, and stability of a spinning disk.

The conclusions may be summarized as:

- 1- In-plane edge loads decrease the natural frequency of forward and backward waves, and increase the natural frequency of reflected waves of a spinning splined disk.
- 2- The effect of in-plane edge loads on the natural frequencies of clamped disks is greater than for splined disks.
- 3- The edge loads do not couple the bending modes of splined disks, unlike clamped disks.
- 4- The edge loads do not induce divergence and flutter instability into a free splined disk, unlike clamped disk.
- 5- The effect of tangential loads on the transverse response of the disk is higher than the effect of radial loads.

(ii) Mechanism of Instability for a Spinning Splined Guided Disk Subjected to In-plane Edge Loads

An expression for the rate of work done by the transverse components of the applied in-plane loads, and their interaction at the inner radius, was derived. Then the work done was computed numerically. The results were used to analyze the mechanism of instability at different rotation speeds. It was concluded that:

- 1- The rate of work done by the in-plane edge loads is positive at flutter speeds for guided splined disks, which induces instability into the system. In other words, application of in-plane edge loads at a flutter instability speed leads to inducing energy to the disk, which transfers to transverse deflection of the disk.
- 2- The effect of the tangential in-plane edge loads on the instability of guided splined disks is greater than the effect of radial edge loads.

(iii) Experimental Investigations of Idling and Cutting Characteristics of Guided Splined Saws

Experimental tests facilities were developed which enables conducting idling and cutting tests. Idling and cutting tests were conducted for a guided splined saw. The conclusions are summarized as follow:

- 1- From idling run up tests of a guided splined saw, the critical speeds, and flutter instability speeds can be obtained.
- 2- Cutting at critical speeds, and super critical speeds is possible. They result in stable operational speeds of the blade.
- 3- Cutting at flutter instability speeds may result in large deviation of the cut.

- 4- Maximum operation speed of a guided splined saw is the initiation of a flutter instability speed.

(iv) Flutter Speed Charts for Guided Splined-Arbor Saws

Experimental run-up tests of several guided splined disks and saws of different sizes were presented, and the flutter instability zones were identified. The results indicated that flutter instability occurs at speeds when a backward travelling wave of a mode meets a reflected wave of a different mode. Sometimes, the system cannot pass a flutter zone, and transverse vibrations of the disk lock into that flutter instability zone. The maximum stable operating speed of the rotating splined disk was defined as the start of a flutter which the system cannot pass. Using the equations of motion for guided splined disks the flutter instability zones were identified. The results showed that the mathematical model can predict accurately the flutter instability zones measured in the experimental tests. The effect of the geometrical parameters of the blade on the start of flutter instability was analyzed. The main conclusions can be summarized as:

- 1- The results show that the mathematical model can predict accurately the flutter instability zones measured in the experimental tests. However, in the case where, in practice, the system cannot pass a flutter zone, the linear model fails to exhibit such behaviour.
- 2- The initiation of flutter instability has a liner relation with the blade thickness. The non-dimensionalized initiation of flutter speed were computed as a function of a non-dimensionalized parameter a/b , where a and b are the inner and outer radius of the blade respectively.
- 3- Flutter instability speeds of splined saws of various sizes were computed and verified experimentally.

4- Flutter speed charts of splined saws were developed to provide primary guide lines for sawmills in choosing of a blade thickness and stable operation speeds. These results are based upon tests conducted in a laboratory environment. Situations in the mills may not be ideal and this may result in mills not being able to duplicate these results. Therefore, mill trials are necessary in order to see if these results can be duplicated. The results can be used as a measure of how close a mill is to meet optimal conditions.

6.2 Suggestions for Further Research

In practice, having a perfect blade with no run-out is impossible. In addition, during cutting, due to friction, heat may induce into the body of the blade. Therefore temperature gradient in the body of the blade is unavoidable.

In current research damping has not been included in the analyses. It is possible that there are damping forces (might be negative or positive) in contact between the saw blade and the wood in cutting zone.

Therefore, theoretical analysis and experimental investigation of the dynamic behaviour of guided splined saw, considering the following effects, is necessary and need to be undertaken:

- The effect of non-flatness
- The effect of temperature distribution in the blade
- The effect of damping (rotating and non-rotating damping force at the cutting zone on the edge of the blade)

References

- [1] Hutton, S.G., Chonan, S., and Lehmann, B.F., 1987, "Dynamic Response of a Guided Circular Saw," *Journal of Sound and Vibration*, 112, pp. 527-539.
- [2] Chen, J.S., and Bogy, D.B., 1993, "Natural Frequencies and Stability of a Flexible Spinning Disk-Stationary Load System With Rigid Body Tilting," *ASME Journal of Applied Mechanics*, 60, pp. 470-477.
- [3] Chen, J.S., and Hsu, C.M. , 1997, "Forced Response of a Spinning Disk Under Space-Fixed Couples," *Journal of Sound and Vibration*, 206(5), pp. 627-639.
- [4] Chen, J.S. and Wong, C.C., 1995, "Divergence Instability of a Spinning Disk with Axial Spindle Displacement in Contact with Evenly Spaced Stationary Springs," *Journal of Applied Mechanics*, 62, pp. 544-547.
- [5] Yang, S.M., 1993, "Vibration of a Spinning annular Disk with Coupled Rigid-body Motion," *ASME Journal of Vibration and Acoustics*, 115, pp. 159-164.
- [6] Mote, C.D., 1977, "Moving Load Stability of a Circular Plate on a Floating Central Collar," *Journal of Acoustical Society of America*, 61, pp. 439-447.
- [7] Price K.B., "Analysis of the Dynamics of Guided Rotating Free Centre Plates", Ph.D. Dissertation, University of California, Berkeley, 1987.
- [8] Khorasany, R.M.H., and Hutton, S.G., 2010, "An Analytical Study on the Effect of Rigid Body Translational Degree of Freedom on the Vibration Characteristics of Elastically

Constrained Rotating Disks,” *International Journal of Mechanical Sciences*, 52, pp. 1186-1192.

[9] Tobias, S.A., and Arnold, R.N., 1957, "The Influence of Dynamical Imperfections on the Vibration of Rotating Disks," *Institution of Mechanical Engineers, Proceedings* 171, pp. 669-690.

[10] Raman, A., and Mote, C.D., 2001, “Experimental Studies on the Non-linear Oscillations of Imperfect Circular Disks Spinning Near Critical Speed,” *International Journal of Non-Linear Mechanics*, 36(2), 2001, pp. 291-305.

[11] Kang, N., and Raman, A., 2006, “Vibrations and Stability of a Flexible Disk Rotating in a Gas-filled Enclosure-Part 2: Experimental Study,” *Journal of Sound and Vibration*, 296(4-5), pp. 676-68.

[12] D’Angelo, C., Mote, C.D., 1993, “Aerodynamically Excited Vibration and Flutter of a Thin Disk Rotating at Supercritical Speed,” *Journal of Sound and Vibration*, 168, pp. 15-30.

[13] Thomas, O., Touze, C., and Chaigne, A., 2003, “Asymmetric Non-linear Forced Vibrations of Free-edge Circular Plates. Part II: Experiments,” *Journal of Sound and Vibration*, 265(5), pp. 1075-1101.

[14] Jana, A., and Raman, A., 2005, “Nonlinear Aeroelastic Flutter Phenomena of a Flexible Disk Rotating in an Unbounded Fluid,” *Journal of Fluids and Structures*, 20(7), pp. 993-1006.

- [15] Khorasany, R.M.H., and Hutton, S.G., June 2011, "Vibration Characteristics of Rotating Thin Disks, Part I: Experimental Results," ASME Journal of Applied Mechanics.
- [16] Khorasany, R.M.H., and Hutton, S.G., June 2011, "Vibration Characteristics of Rotating Thin Disks, Part II: Analytical Predictions," ASME Journal of Applied Mechanics.
- [17] Chen, J.S. and Wong, C.C., 1996, "Modal Interaction in a Spinning Disk on a Floating Central Collar and Restrained by Multiple Springs," Journal of the Chinese Society of Mechanical Engineers, Vol. 17, No.3, pp. 251-259.
- [18] Chen, J. S., and Bogy, D.B., 1992, "Mathematical Structure of Modal Interactions in a Spinning Disk-Stationary Load System," American Society of Mechanical Engineers Journal of Applied mechanics, 59, pp. 390-397.
- [19] Young, T.H., and Lin, C.Y., 2006, "Stability of a Spinning Disk under a Stationary Oscillating Unit," Journal of Sound and Vibration, 298, pp 307-18.
- [20] Schajer, G.S., Wang, S.A., 2002, "Effect of Work Piece Interaction on Circular Saw Cutting Satiability," European Journal of Wood and Wood Products, 02/2002, Volume 60, Number 1, pp.48-54.
- [21] Schajer G., 1984, "Guided Saw Hunting", Forest Products Journal, Vol. 38, No. 4.
- [22] Mohammadpanah. A., "Idling and Cutting Vibration Characteristics of Guided Circular Saws", January 2012, M.A.Sc. Thesis, The University of British Columbia.
- [23] Chen J.S., "Stability Analysis of a Spinning Elastic Disk under a Stationary Concentrated Edge Load", ASME, Vol. 61, Dec. 1994.

- [24] Chen J.S., “Vibration and Stability of a Spinning Disk under Stationary Distributed Edge Loads”, *Journal of Applied Mechanics*, Vol. 63, June 1996.
- [25] Chen J.S., “On the Internal Resonance of a Spinning Disk under Space-Fixed Pulsating Edge Loads”, *ASME*, Vol. 68, November 2001
- [26] Chen J.S., “Parametric Resonance of a Spinning Disk under Space-Fixed Pulsating Edge Loads”, *Journal of Applied Mechanics*, March 1997, Vol. 64/139-143.
- [27] Shen I.Y., Song Y., “Stability and Vibration of a Rotating Circular Plate Subjected to Stationary In-Plane Edge Loads”, *Journal of Applied Mechanics*, March 1996, Vol. 63/121-127.
- [28] Young T.H. and Wu M.Y., “Dynamic Stability of Disks with Periodically Varying Spin Rates Subjected to Stationary In-Plane Edge Loads”, *ASME*, Vol. 71, July 2004.
- [29] Tian, J.F., and Hutton, S.G., 2001, “Cutting Induced Vibration in Circular Saws,” *Journal of Sound and Vibration*, 242(5), pp. 907-922.
- [30] Tian, J.F., and Hutton, S.G., 1999, “Self Excited Vibration in Flexible Rotating Disks Subjected to Transverse Interaction Forces” *ASME Journal of Applied Mechanics*, 66, pp. 800-805.
- [31] Khorasany R.M.H., Mohammadpanah A. and Hutton S.G., 2012, “Vibration Characteristics of Guided Circular Saws: Experimental and Numerical Analyses”, *J. Vib. Acoust.* 134(6), 061004
- [32] Timoshenko S. and Goodier J.N. *Theory of Elasticity*. New York, McGraw-Hill.

- [33] Meirovitch L., 1997, "Principles and Techniques of Vibrations", New Jersey.
- [34] Carlin J.F., Appl F.C., Bridwel H.C., Dubois R.P., "The Effect of Tensioning on Buckling and Vibration of Circular Saw Blades" ASME Journal of Engineering for Industry, Vol. 2, pp. 37-48.
- [35] Dubois R.P., "Buckling Loads of Tensioned Circular Plates Subjected to Concentrate In-Plane Loading" A Master Reports Submitted to the Kansas State University 1970.
- [36] St. Cyr, W.W. "Vibration and Stability of Circular Plates Subjected to Concentrated In-Plane Forces", PhD Dissertation, Kansas State University 1965.
- [37] Stakgold, Ivar, 1998, "Green's Functions and Boundary Value Problems", 2nd Edition.
- [38] Gary S. Schajer, 1983, "Analysis of Roll Tensioning and its Influence on Circular Saw Stability" Wood Science and Technology, 11/1983,17(4):287-302
- [39] Bruce Lehmann, "Saw Tooth Design and Tipping Materials" Sr. Engineer, Thin Kerf Technologies Inc. British Columbia, Canada

Appendix A

Stresses Fields in a Disk due to Centrifugal Acceleration

σ_{rr} and $\sigma_{\theta\theta}$ are axi-symmetric in-plane stresses due to centrifugal acceleration. The close form solution of σ_{rr} and $\sigma_{\theta\theta}$ are [32].

For a disk with free inner boundary condition:

$$\sigma_r = \rho\Omega^2 \left(\frac{3+\nu}{8} (a^2 + b^2) - \frac{3+\nu}{8r^2} a^2 b^2 - \frac{3+\nu}{8} r^2 \right) \quad (\text{A.1})$$

$$\sigma_\theta = \rho\Omega^2 \left(\frac{3+\nu}{8} (a^2 + b^2) + \frac{3+\nu}{8r^2} a^2 b^2 - \frac{1+3\nu}{8} r^2 \right) \quad (\text{A.2})$$

For a disk with clamped inner boundary condition:

$$\sigma_r = \rho\Omega^2 \left(\frac{1+\nu}{8} \frac{(v-1)a^4 - (3+\nu)b^4}{(v-1)a^2 - (1+\nu)b^2} + \frac{1-\nu}{8r^2} a^2 b^2 \frac{(v+1)a^2 - (3+\nu)b^2}{(v-1)a^2 - (1+\nu)b^2} - \frac{3+\nu}{8} r^2 \right) \quad (\text{A.3})$$

$$\sigma_\theta = \rho\Omega^2 \left(\frac{1+\nu}{8} \frac{(v-1)a^4 - (3+\nu)b^4}{(v-1)a^2 - (1+\nu)b^2} - \frac{1-\nu}{8r^2} a^2 b^2 \frac{(v+1)a^2 - (3+\nu)b^2}{(v-1)a^2 - (1+\nu)b^2} - \frac{1+3\nu}{8} r^2 \right) \quad (\text{A.4})$$

Appendix B

Mathematical Equations for Rigid Body Tilting and Translational Motions

Consider a point on the disk with respect to the coordinate attach to the disk (Figure B.1).

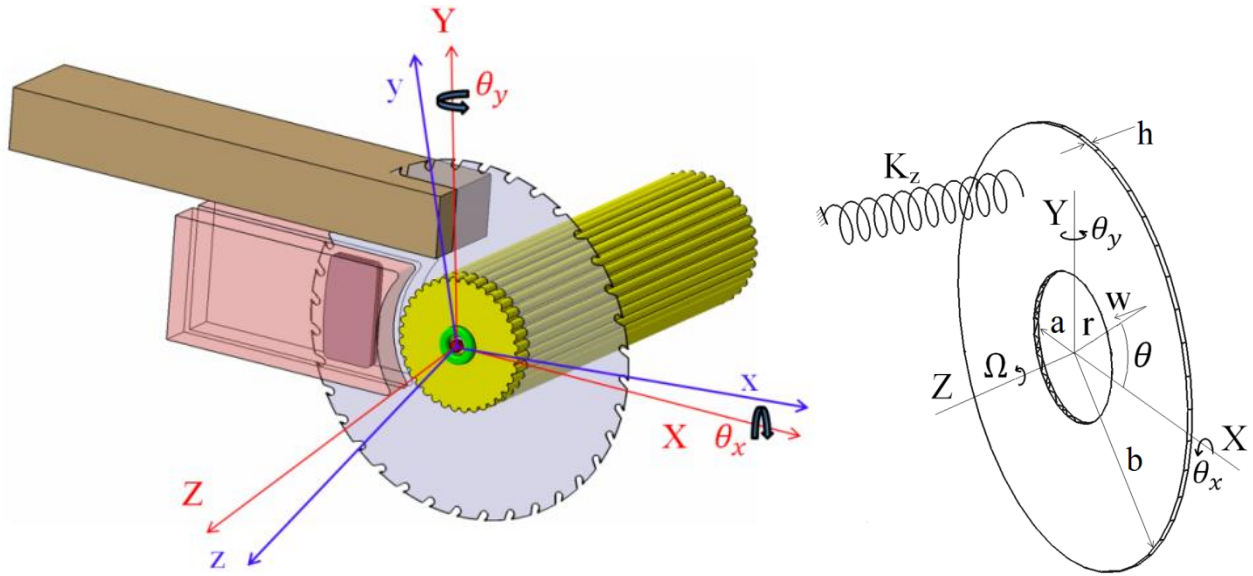


Figure B.1 a) Schematic of Guided Spline Saw, b) Idealizing the Blade as a Spinning Disk

$$\text{Position of a point on the disk with respect to attach frame} = \begin{bmatrix} r \cos \theta \\ r \sin \theta \\ w \end{bmatrix} \quad (\text{B.1})$$

Consider O-XYZ as space fixed coordinate (Figure B.1):

$$\text{Position of a point on the disk with respect to inertial frame is: } R = \begin{bmatrix} X \\ Y \\ Z \end{bmatrix}$$

The following transformation between two coordinates can be used:

$$R = \begin{bmatrix} X \\ Y \\ Z \end{bmatrix} = \begin{bmatrix} \cos \theta_y & 0 & \sin \theta_y \\ 0 & 1 & 0 \\ -\sin \theta_y & 0 & \cos \theta_y \end{bmatrix} \begin{bmatrix} 1 & 0 & 0 \\ 0 & \cos \theta_x & -\sin \theta_x \\ 0 & \sin \theta_x & \cos \theta_x \end{bmatrix} \begin{bmatrix} r \cos \theta \\ r \sin \theta \\ w \end{bmatrix} \quad (\text{B.2})$$

The total angular momentum H of the blade, with respect to the origin of the blade O is:

$$H_O = \rho h \int_0^{2\pi} \int_a^b R \times \dot{R} r dr d\theta \quad (\text{B.3})$$

Substituting the approximation ($\sin \theta_x \cong \theta_x$ and $\cos \theta_x \cong 1 - \frac{\theta_x^2}{2}$ and the same for θ_y) and the moment of inertia for a disk ($I_x = I_y = \frac{\pi}{4} \rho h (b^4 - a^4) = \rho h I$):

$$\dot{H}_{Ox} = \rho h I (\ddot{\theta}_x + 2\Omega \dot{\theta}_y) + \int_0^{2\pi} \int_a^b \rho h \sin \theta (w_{,tt} + 2\Omega w_{,t\theta}) r^2 dr d\theta \quad (\text{B.4})$$

$$\dot{H}_{Oy} = \rho h I (\ddot{\theta}_y - 2\Omega \dot{\theta}_x) + \int_0^{2\pi} \int_a^b \rho h \cos \theta (w_{,tt} + 2\Omega w_{,t\theta}) r^2 dr d\theta \quad (\text{B.5})$$

Consider that the disk has rigid body translational in Z direction. Also, Consider there is a spring (k_z) at position of (r_k, θ_k) , so the force produce by this spring is:

$$f_s = -k_z (w + Z + r_k \sin \theta_k \theta_x - r_k \cos \theta_k \theta_y) \quad (\text{B.6})$$

Also consider there is a force (f_z) at position of (r_f, θ_f) . By writing the balance equation between the angular momentum, and the torque produced by spring and external force:

$$\dot{H}_{Ox} = f_s r_k \sin \theta_k + f_z r_f \sin \theta_f \quad (\text{B.7})$$

$$\dot{H}_{Oy} = -f_s r_k \cos \theta_k - f_z r_f \cos \theta_f \quad (\text{B.8})$$

Substituting from equations (B.4) and (B.5):

$$\rho h I (\ddot{\theta}_x + 2\Omega \dot{\theta}_y) + \int_0^{2\pi} \int_a^b \rho h \sin \theta (w_{,tt} + 2\Omega w_{,t\theta}) r^2 dr d\theta = f_s r_k \sin \theta_k + f_z r_f \sin \theta_f \quad (\text{B.9})$$

$$\rho h I (\ddot{\theta}_y - 2\Omega \dot{\theta}_x) + \int_0^{2\pi} \int_a^b \rho h \cos \theta (w_{,tt} + 2\Omega w_{,t\theta}) r^2 dr d\theta = -f_s r_k \cos \theta_k - f_z r_f \cos \theta_f$$

(B.10)

By adding the translational acceleration term (\ddot{Z}) and angular acceleration ($\ddot{\theta}_x$ and $\ddot{\theta}_y$) to equation (1.1):

$$\begin{aligned}
\rho h(w_{,tt} + 2\Omega w_{,t\theta} + \Omega^2 w_{,\theta\theta}) + D\nabla^4 w - \frac{h}{r}(\sigma_r r w_{,r})_{,r} - \frac{h}{r^2}\sigma_\theta w_{,\theta\theta} + \rho h\ddot{Z} \\
+ \rho h(r\ddot{\theta}_x \sin \theta - r\ddot{\theta}_y \cos \theta) + \rho h(2\Omega r \cos \theta \dot{\theta}_x + 2\Omega r \sin \theta \dot{\theta}_y) \\
= -\frac{k_z}{r}(w + Z + r_k \sin \theta_k \theta_x - r_k \cos \theta_k \theta_y) + \frac{f_z}{r}
\end{aligned} \tag{B.11}$$

And, the rigid body translational equation in Z is:

$$m\ddot{Z} + \int_0^{2\pi} \int_a^b \rho h(w_{,tt}) r dr d\theta = -k_z(w + Z + r_k \sin \theta_k \theta_x - r_k \cos \theta_k \theta_y) + f_z \tag{B.12}$$

Where, $m = \pi(b^2 - a^2)\rho h$ is the total mass of the disk.

Appendix C

Solution of the Equations of Motion

For a circular disk the vibration modes can be described by the number of nodal circles (n) and the number of nodal diameters (m). So, the transverse displacement of the disk may be written by a modal expansion as [22]:

$$W(R, \theta, t) = \sum_{m,n=0}^{\infty} [S_{mn}(\tau) \sin m\theta + C_{mn}(\tau) \cos m\theta] R_m(\lambda_{mn}R) \quad (C.1)$$

First the Non-dimensional parameters are introduced as:

$$R = \frac{r}{b}, \quad W = \frac{w}{b}, \quad \tau = \sqrt{\frac{D}{\rho hb^4}} t, \quad \Omega^* = \sqrt{\frac{\rho hb^4}{D}} \Omega \quad (C.2)$$

Substituting of $W(R, \theta, t)$ into equation (2.8) results in[22]:

$$\ddot{S}_{mn} - 2\Omega^* m \dot{C}_{mn} + (\lambda_{mn}^4 - m^2 \Omega^{*2}) S_{mn} - \frac{\Omega^{*2}}{b^2} \pi \sum_{q=0}^{\infty} S_{mq} \Pi_{mq} = F_{pq} \sin m\theta R_m(\lambda_{mn}R) \quad (C.3)$$

$$\ddot{C}_{mn} - 2\Omega^* m \dot{S}_{mn} + (\lambda_{mn}^4 - m^2 \Omega^{*2}) C_{mn} - \frac{\Omega^{*2}}{b^2} \pi \sum_{q=0}^{\infty} C_{mq} \Pi_{mq} = F_{pq} \cos m\theta R_m(\lambda_{mn}R) \quad (C.4)$$

Where

$$\Pi_{mq} = \int_a^1 (C_{rr} \frac{d^2 R_m(\lambda_{mq}R)}{dR^2} + C_r \frac{dR_m(\lambda_{mq}R)}{dR} - m^2 C_{\theta\theta} R_m(\lambda_{mq}R)) R_m(\lambda_{mn}R) R dR = 0 \quad (C.5)$$

And

$$F_{pq} = -\frac{b^3}{D} \sum_{p,q=0}^{\infty} [(kS_{pq}(\tau) + c\dot{S}_{pq}(\tau)) \sin p\theta + (kC_{pq}(\tau) + c\dot{C}_{pq}(\tau)) \cos p\theta] R_p(\lambda_{pq}R) \quad (\text{C.6})$$

The non dimensionalized stationary equation of motion for a plate in polar coordinate system is:

$$\nabla^4 W = \lambda^4 W \quad (\text{C.7})$$

Using the boundary conditions we can obtain the eigenvalues λ_{mn} associated with the eigenfunctions as: [33]

$$\Phi_{mn} = \begin{cases} \sin m\theta \\ \cos m\theta \end{cases} R_m(\lambda_{mn}R) \quad (\text{C.8})$$

$$R_m(\lambda_{mn}R) = (e_{1m}J_m(\lambda_{mn}R) + e_{2m}Y_m(\lambda_{mn}R) + e_{3m}I_m(\lambda_{mn}R) + e_{4m}K_m(\lambda_{mn}R)) \quad (\text{C.9})$$

Where $J_m, Y_m, I_m,$ and K_m are m th order Bessel functions and modified Bessel functions; and $e_{1m}, e_{2m}, e_{3m},$ and e_{4m} are constants.

Appendix D

Stresses Fields in a Disk due to In-Plane Edge Loads

Following the [34], [35], and [36] procedure the stresses due to the edge loads are calculated (for outer and inner edge):

Stress due to the Radial Force (F_r):

Consider ϕ as a stress field in a polar coordinates. The resulting stresses are [35]:

$$\sigma_r = \frac{1}{r} \frac{\partial \phi}{\partial r} + \frac{1}{r^2} \frac{\partial^2 \phi}{\partial \theta^2} \quad (1.D)$$

$$\sigma_\theta = \frac{\partial^2 \phi}{\partial r^2}$$

$$\tau_{r\theta} = -\frac{\partial}{\partial r} \left(\frac{1}{r} \frac{\partial \phi}{\partial \theta} \right)$$

In order to satisfy the compatibility equations $\nabla^4 \phi = 0$. To satisfy this equation, the general solution is [35]:

$$\begin{aligned} \phi = & a_0 \ln(r) + b_0 r^2 + c_0 r^2 \ln(r) + d_0 r^2 \theta + a'_0 \theta + b'_0 r^2 \theta \ln(r) + c'_0 \theta \ln(r) - \frac{1}{2} c_1 r \theta \cos \theta + \\ & f_1 r \theta \ln(r) \cos \theta + f'_1 r \theta \ln(r) \sin \theta + \frac{1}{2} a_1 r \theta \sin \theta + (b_1 r^3 + c'_1 r^{-1} + b'_1 r \ln(r)) \cos \theta + \\ & (d_1 r^3 + c'_1 r^{-1} + d'_1 r \ln(r)) \sin \theta + \sum_{n=2}^{\infty} (a_n r^n + b_n r^{n+2} + c'_n r^{-n} + d'_n r^{-n+2}) \cos n\theta + \\ & \sum_{n=2}^{\infty} (c_n r^n + d_n r^{n+2} + c'_n r^{-n} + d'_n r^{-n+2}) \sin n\theta \end{aligned} \quad (2.D)$$

Using this function the stresses can be calculated as:

$$\begin{aligned} \sigma_r = & \frac{1}{r} \frac{\partial \phi}{\partial r} + \frac{1}{r^2} \frac{\partial^2 \phi}{\partial \theta^2} = a_0 r^{-2} + 2b_0 + c_0 + 2d_0 \theta + 2c_0 \ln(r) + 2b'_0 \theta \ln(r) + b'_0 \theta + c'_0 \theta r^{-2} + \\ & f_1 \theta r^{-1} \cos \theta + f'_1 \theta r^{-1} \sin \theta - 2f_1 r^{-1} \ln(r) \sin \theta + 2f'_1 r^{-1} \ln(r) \cos \theta + [a_1 r^{-1} + 2b_1 r - \end{aligned}$$

$$\begin{aligned}
& 2a'_1r^{-3} + b'_1r^{-1}] \cos\theta + [c_1r^{-1} + 2d_1r - 2c'_1r^{-3} + d'_1r^{-1}] \sin\theta + \sum_{n=2}^{\infty} (n(1-n)a_nr^{n-2} + \\
& (n+2-n^2)b_nr^n - n(1+n)a'_nr^{-n-2} + (2-n-n^2)b'_nr^{-n}) \cos n\theta + \sum_{n=2}^{\infty} (n(1- \\
& n)c_nr^{n-2} + (n+2-n^2)d_nr^n - n(1+n)c'_nr^{-n-2} + (2-n-n^2)d'_nr^{-n}) \sin n\theta \quad (3.D)
\end{aligned}$$

since σ_r is an even function due to symmetry about the point of application of the in-plane load, then $c_n = d_n = c'_n = d'_n = 0$ for $n=1,2,3,\dots$. Since σ_r is a single-valued function of θ , then $d_0 = b'_0 = c'_0 = f_1 = f'_1 = 0$.

Substituting these coefficient for σ_r :

$$\begin{aligned}
\sigma_r = & a_0r^{-2} + 2b_0 + c_0 + 2c_0 \ln(r) + [a_1r^{-1} + 2b_1r - 2a'_1r^{-3} + b'_1r^{-1}] \cos\theta + \\
& \sum_{n=2}^{\infty} (n(1-n)a_nr^{n-2} + (n+2-n^2)b_nr^n - n(1+n)a'_nr^{-n-2} + \\
& (2-n-n^2)b'_nr^{-n}) \cos n\theta \quad (4.D)
\end{aligned}$$

$$\begin{aligned}
\sigma_\theta = \frac{\partial^2 \phi}{\partial r^2} = & -a_0r^{-2} + 2b_0 + 3c_0 + 2c_0 \ln(r) + [6b_1r + 2a'_1r^{-3} + b'_1r^{-1}] \cos\theta + \\
& \sum_{n=2}^{\infty} (n(n-1)a_nr^{n-2} + (n+2)(n+1)b_nr^n + n(1+n)a'_nr^{-n-2} + (n-2)(n- \\
& 1)b'_nr^{-n}) \cos n\theta \quad (5.D)
\end{aligned}$$

$$\begin{aligned}
\tau_{r\theta} = -\frac{\partial}{\partial r} \left(\frac{1}{r} \frac{\partial \phi}{\partial \theta} \right) = & -a'_0r^{-2} + [2b_1r - 2a'_1r^{-3} + b'_1r^{-1}] \sin\theta + \sum_{n=2}^{\infty} (n(n-1)a_nr^{n-2} + \\
& n(n+1)b_nr^n - n(1+n)a'_nr^{-n-2} - n(n-1)b'_nr^{-n}) \sin n\theta \quad (6.D)
\end{aligned}$$

Now, the boundary conditions need to be defined:

The stress distribution at the edge of the disk can be found by first considering the Fourier series expansion of a uniformly distributed loading over an arc of length 2ε and intensity such that the total load is F_r ; then letting ε goes to 0. The result of the stress at the outer edge is:

$$\sigma_r(b) = \frac{-F_r}{\pi b h} \left[\frac{1}{2} + \sum_{n=1}^{\infty} \cos n\theta \right] \quad (7.D)$$

and similarly for the inner edge:

$$\sigma_r(a) = \frac{-F_r}{\pi a h} \left[\frac{1}{2} + \sum_{n=1}^{\infty} \cos n\theta \right] \quad (8.D)$$

At the outer and inner edge the shear stress is zero: $\tau_{r\theta}(b, \theta) = \tau_{r\theta}(a, \theta) = 0$.

So the resulting stress distribution is:

$$\sigma_r = \frac{-F_r}{\pi b h} \sum_{n=0}^{\infty} \left[a^1_n \left(\frac{r}{b}\right)^{n-2} + a^2_n \left(\frac{r}{b}\right)^n + a^3_n \left(\frac{r}{b}\right)^{-n-2} + a^4_n \left(\frac{r}{b}\right)^{-n} \right] \cos n\theta \quad (9.D)$$

$$\sigma_\theta = \frac{-F_r}{\pi b h} \sum_{n=0}^{\infty} \left[b^1_n \left(\frac{r}{b}\right)^{n-2} + b^2_n \left(\frac{r}{b}\right)^n + b^3_n \left(\frac{r}{b}\right)^{-n-2} + b^4_n \left(\frac{r}{b}\right)^{-n} \right] \cos n\theta \quad (10.D)$$

$$\sigma_{r\theta} = \frac{-F_r}{\pi b h} \sum_{n=0}^{\infty} \left[c^1_n \left(\frac{r}{b}\right)^{n-2} + c^2_n \left(\frac{r}{b}\right)^n + c^3_n \left(\frac{r}{b}\right)^{-n-2} + c^4_n \left(\frac{r}{b}\right)^{-n} \right] \cos n\theta \quad (11.D)$$

And the coefficients are:

For $n=0$, and $n=1$, the coefficients are:

$$\text{Consider: } R = \frac{a}{b}, \quad \alpha = \frac{1+\nu}{1-\nu}, \quad \beta = \frac{3-\nu}{\nu+1},$$

$$a^1_0 = -b^1_0 = \frac{1}{2} R^2 \left(\frac{1}{\alpha} + R^2 \right)$$

$$a^2_0 = b^2_0 = \frac{1}{2} \alpha \left(\frac{1}{\alpha} + R^2 \right)$$

$$a^3_0 = a^4_0 = b^3_0 = b^4_0 = 0$$

$$c^1_0 = c^2_0 = c^3_0 = c^4_0 = 0$$

$$a^1_1 = 1$$

$$b^1_1 = c^1_1 = 0$$

$$a^2_1 = b^2_1 = c^2_1 = \frac{3(1-\nu)(\alpha R^2+1)}{4(1+\beta R^4)}$$

$$a^3_1 = b^3_1 = c^3_1 = \frac{R^2(1-\nu)(\alpha-\beta R^2)}{4(1+\beta R^4)}$$

$$a^4_1 = b^4_1 = c^4_1 = \frac{1}{2}(1 - \nu)$$

which numerical results show we can get sufficient approximation just using the $n=0$, and $n=1$.

However if we want more accurate results for $n=2,3,4,\dots$; the coefficients are:

$$a^1_n = b^1_n = c^1_n = \frac{-n\beta R^{-2n} + (n^2 - 1 + \beta^2)R^2 + n(n-1)}{(n^2 - 1)(R - R^{-1})^2 + (\beta R - R^{-1})^2}$$

$$a^2_n = \frac{(n-2)(\beta R^{-2n} - nR^{-2} + n+1)}{(n^2 + 1)(R - R^{-1})^2 + (\beta R - R^{-1})^2}$$

$$b^2_n = \frac{(n+2)(\beta R^{-2n} - nR^{-2} + n)}{4(\beta(R^n + R^{-n}))^2}$$

$$c^2_n = \frac{n(\beta R^{-2n} + n)}{(n^2 - 1)(R - R^{-1})^2 + (\beta R - R^{-1})^2}$$

$$a^3_n = b^3_n = c^3_n = \frac{-(n^2-1+\beta^2)R^2-n(n+1)+n\beta R^{2n}}{3\beta R^{2n}+(n^2-1)(R-R^{-1})^2+(\beta R-R^{-1})^2}$$

$$a^4_n = \frac{(n)(\beta R^{2n}-nR^{-2}-n+1)}{(n^2-1)(R-R^{-1})^2+(\beta R-R^{-1})^2}$$

$$b^4_n = \frac{(n)(\beta R^{2n}-nR^{-2}-n+1)}{3(\beta(R^n)^2+(n^2-1)(R-R^{-1})^2+(\beta R-R^{-1})^2)}$$

$$c^4_n = \frac{n(\beta R^{2n}-nR^{-2}-n)}{2(\beta(R^n)^2+(n^2-1)(R-R^{-1})^2+(\beta R-R^{-1})^2)}$$

Stress due to the Tangential Force (F_t):

Using the same procedure by Song [27] the stresses due to tangential loads are:

$$\sigma_r = \left[-\frac{2e_1}{r^3} + 2f_1r + \frac{g_1}{r} - \frac{F_t b}{\pi h}\right] \sin\theta + \sum_{n=2}^{\infty} ((n-n^2)d_n r^{n-2} - (n+n^2)e_n r^{-n-2} - (2+n-n^2)f_n r^n + (2-n-n^2)g_n r^{-n}) \sin n\theta \quad (12.D)$$

$$\sigma_\theta = \left[\frac{2e_1}{r^3} + 6f_1r + \frac{g_1}{r}\right] \sin\theta + \sum_{n=2}^{\infty} ((n^2-n)d_n r^{n-2} + (n+n^2)e_n r^{-n-2} + (2+3n+n^2)f_n r^n + (2-3n+n^2)g_n r^{-n}) \sin n\theta \quad (13.D)$$

$$\tau_{r\theta} = \frac{F_t b}{2\pi h r^2} + \left[\frac{2e_1}{r^3} - 2f_1r - \frac{g_1}{r}\right] \cos\theta - \sum_{n=2}^{\infty} ((n^2-n)d_n r^{n-2} - (n+n^2)e_n r^{-n-2} - (n+n^2)f_n r^n + (n-n^2)g_n r^{-n}) \sin n\theta \quad (14.D)$$

and the coefficients are:

$$e_1 = K(1+\nu)b^4 + (3+\nu)b^2$$

$$f_1 = K(1 + \nu)$$

$$g_1 = -\frac{F_t(1-\nu)}{4\pi h}$$

whereas

$$K = \frac{F_t(1+\nu)a^2 - (3+\nu)b^2}{8\pi h(1+\nu)b^4 + (3-\nu)a^4}$$

And for $n=2$

$$d_2 = e_2 = \frac{6F_t}{\pi b h}$$

$$f_2 = g_2 = \frac{-6F_t}{\pi a^3 b h}$$

Numerical results show we can get sufficient accuracy just by using the $n=0$, and $n=1$. However if we want more accurate results, we can compute the coefficients for $n=2,3,4,\dots$

Appendix E

The Governing Equations of a Rigid disk, Subjected to In-plane Edge Loads

Consider a rigid splined disk, subjected to the radial and tangential forces according to the Figure 2.3 configuration. The parameters which govern the motion of the disk are just the rigid body tilting and translational motion θ_x, θ_y and z . Since the applied forces F_r and F_t are in balance with the inner interaction forces, and the disk is rigid the boundary equations vanish. Consider a rigid disk ($w = 0$), the equations of motion are:

$$\rho h l (\ddot{\theta}_x + 2\Omega \dot{\theta}_y) = -F_r (b - a) \sin \alpha \sin(\theta_x) + (F_t \sin(\theta_x) (b) - \frac{b-a}{2a} F_t \sin(\theta_x) a - \frac{a+b}{2a} F_t \sin(\theta_x) a) \sin \alpha \quad (\text{E.1})$$

$$\rho h l (\ddot{\theta}_y - 2\Omega \dot{\theta}_x) = -F_r (b - a) \cos \alpha \sin(\theta_y) + (F_t \sin(\theta_y) (b) - \frac{b-a}{2a} F_t \sin(\theta_y) a - \frac{a+b}{2a} F_t \sin(\theta_y) a) \cos \alpha \quad (\text{E.2})$$

Simplifying the equations F_t vanishes from the equations. Also, for small oscillation we assume $\sin(\theta_x) \cong \theta_x$ and $\sin(\theta_y) \cong \theta_y$. The equations become:

$$\rho h l (\ddot{\theta}_x + 2\Omega \dot{\theta}_y) = -F_r (b - a) \sin \alpha \theta_x \quad (\text{E.3})$$

$$\rho h l (\ddot{\theta}_y - 2\Omega \dot{\theta}_x) = -F_r (b - a) \cos \alpha \theta_y \quad (\text{E.4})$$

Rearranging the equations:

$$\ddot{\theta}_x + 2\Omega \dot{\theta}_y + \frac{(b-a) \sin \alpha F_r}{\rho h l} \theta_x = 0 \quad (\text{E.3})$$

$$\ddot{\theta}_y - 2\Omega \dot{\theta}_x + \frac{(b-a) \cos \alpha F_r}{\rho h l} \theta_y = 0 \quad (\text{E.4})$$

The solution of this system of second order differential equations is:

$$\theta_x = \theta e^{i\omega_n t}, \theta_y = i\theta e^{i\omega_n t} \quad (\text{E.5})$$

Whereas θ is a constant, and ω_n can be obtained from the following equation:

$$\omega_n = \frac{2\Omega + \sqrt{4\Omega^2 - 2\gamma}}{2} \quad (\text{E.6})$$

Whereas

$$\gamma = \frac{(b-a)}{\rho h l} F_r \quad (\text{E.7})$$

In order for the equations to hold:

$$4\Omega^2 - 2 \frac{(b-a)}{\rho h l} F_r \geq 0 \quad (\text{E.8})$$

$$\text{Therefore: } F_r \leq \frac{2\rho h l \Omega^2}{(b-a)} \quad (\text{E.9})$$

$$\frac{\partial \omega_n}{\partial F_r} = -\frac{1}{2} (4\Omega^2 - 2\gamma)^{-\frac{1}{2}} \left(2 \left(\frac{b-a}{\rho h l} \right) \right) = -\frac{b-a}{\rho h l \sqrt{4\Omega^2 - 2\gamma}} \quad (\text{E.10})$$

Appendix F

Gullet Feed Index and Feed Speed

Gullet Feed Index (GFI) is percentage of tooth blade gullet filled and usually is a number between 0.3 to 0.7 [39].

The maximum feed speed for a given depth of cut might be calculated as [39]:

$$\text{Maximum Feed Speed} = \frac{GFI \cdot c \cdot A}{P \cdot D}$$

$$\text{Bite/Tooth} = \frac{1}{N} (\text{Feed Speed}) \cdot \frac{60}{RPM}$$

c = blade rim speed

A = Gullet area

P=Tooth pitch

D= depth of cut

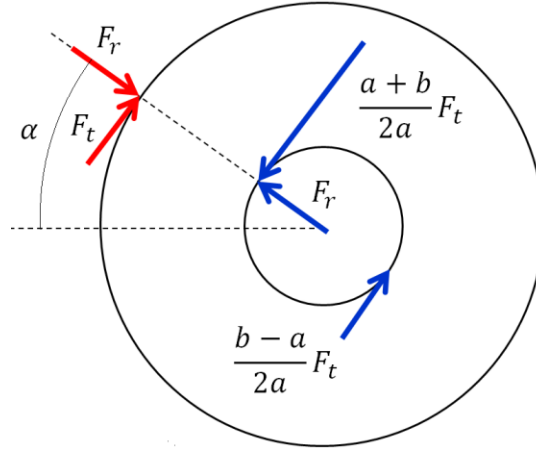
N= Number of Teeth

Appendix G

Derivative of Eigenvalues of Spinning Disk with Respect to In-plane Edge Loads

To analyze the sensitivity of eigenvalues of the spinning disk to in-plane edge loads, the derivative of eigenvalues of the system with respect to the in-plane edge loads is calculated.

Figure H.1 Schematic of a Splined Disk Subjected to In-Plane Edge Loads, and Their Inner Interaction Loads



The equation of motion of spinning disk, without considering the membrane stress, can be written as:

$$\rho h(w_{,tt} + 2\Omega w_{,t\theta} + \Omega^2 w_{,\theta\theta}) + D\nabla^4 w = 0 \quad (\text{G.1})$$

And the boundary conditions are:

$$\frac{F_r \delta(\theta - \alpha)}{bD} w_{,r} + \frac{F_t \delta(\theta - \alpha)}{b^2 D} w_{,\theta} + (w_{,rr} + \frac{1}{r} w_{,r} + \frac{1}{r^2} w_{,\theta\theta})_{,r} + \frac{1-\nu}{r^2} \left((w_{,\theta\theta})_{,r} - \frac{1}{r} w_{,\theta\theta} \right) = 0$$

($r = b$)

$$\begin{aligned}
& -\frac{F_t(a+b)\delta(\theta-\alpha)}{2a^3D}W_{,\theta} + \frac{F_t(b-a)\delta(\pi+\theta-\alpha)}{2a^3D}W_{,\theta} + (W_{,rr} + \frac{1}{r}W_{,r} + \frac{1}{r^2}W_{,\theta\theta})_{,r} + \frac{1-\nu}{r^2}((W_{,\theta\theta})_{,r} - \\
& \frac{1}{r}W_{,\theta\theta}) - \frac{F_r\delta(\theta-\alpha)}{aD}W_{,r} = 0 \\
& \hspace{25em} (r = a)
\end{aligned}$$

Defining the operators:

$$M = \rho h$$

$$G = 2\Omega \frac{\partial}{\partial \theta}$$

$$K = \Omega^2 \frac{\partial^2}{\partial \theta^2} + D\nabla^4$$

$$\nabla^4 = \nabla^2 \nabla^2 = \left(\frac{\partial^2}{\partial r^2} + \frac{1}{r} \frac{\partial}{\partial r} + \frac{1}{r^2} \frac{\partial^2}{\partial \theta^2} \right) \left(\frac{\partial^2}{\partial r^2} + \frac{1}{r} \frac{\partial}{\partial r} + \frac{1}{r^2} \frac{\partial^2}{\partial \theta^2} \right)$$

$$L_1 = \frac{\partial}{\partial r} \left(\frac{\partial^2}{\partial r^2} + \frac{\partial}{r\partial r} + \frac{\partial^2}{r^2\partial \theta^2} \right) + \frac{1-\nu}{r^2} \left(\frac{\partial^3}{\partial r\partial \theta^2} - \frac{\partial^2}{r\partial \theta^2} \right)$$

$$L_2 = \frac{\delta(\theta-\alpha)}{D} \frac{\partial}{\partial r}$$

$$L_3 = \frac{\delta(\theta-\alpha)}{D} \frac{\partial}{\partial \theta}$$

$$L_4 = \frac{\delta(\pi+\theta-\alpha)}{D} \frac{\partial}{\partial \theta}$$

The equation and the boundary conditions become:

$$M\ddot{w} + G\dot{w} + Kw = 0 \tag{G.2}$$

$$b^2L_1w + bF_rL_2w + F_tL_3w = 0 \quad \text{at } r = b$$

$$2a^3L_1w - 2a^2F_rL_2w - (a+b)F_tL_3w + (b-a)F_tL_4w = 0 \quad \text{at } r = a$$

For simplicity we analyze the effect of the radial and tangential loads separately.

Effect of Radial Load

Boundary equations become:

$$bL_1w + F_rL_2w = 0 \quad \text{at } r = b$$

$$aL_1w - F_rL_2w = 0 \quad \text{at } r = a$$

Assume a solution by separation of variable method as:

$$w = w_{mn}(r, \theta)e^{\lambda_{mn}t} \quad (\text{G.3})$$

And assume a separable function for $w_{mn}(r, \theta)$ as:

$$w_{mn}(r, \theta) = R_m(r)e^{\pm in\theta} \quad (\text{G.4})$$

Where $R_m(r)$ is a real value, and can be a function of Bessel functions as:

$$R_m(r) = e_{1m}J_m(r) + e_{2m}I_m(r) \quad (\text{G.5})$$

Where J_m , and I_m are m^{th} order Bessel functions and modified Bessel functions, and e_{1m} and e_{2m} are constant.

Substituting the solution (G.3) into the equation (G.2) [23]:

$$\lambda_{mn}^2 M w_{mn} + \lambda_{mn} G w_{mn} + K w_{mn} = 0 \quad (\text{G.6})$$

Consider λ_{mn}^0 as the eigenvalues of free spinning disk. ($F_r = 0$) and the shape functions are w_{mn}^0 [23]:

$$(\lambda_{mn}^0)^2 M w_{mn}^0 + \lambda_{mn}^0 G w_{mn}^0 + K w_{mn}^0 = 0 \quad (\text{G.7})$$

The boundary equations become (substitute $F_r = 0$ in the boundary equations)

$$L_1 w_{mn}^0 = 0 \quad \text{at } r = a \text{ and } r = b$$

Taking the derivative of equation (G.6) with respect to F_r (prove can be found in [37]):

$$2\lambda_{mn}^0 \frac{\partial \lambda_{mn}}{\partial F_r} M w_{mn}^0 + (\lambda_{mn}^0)^2 M \frac{\partial w_{mn}}{\partial F_r} + \frac{\partial \lambda_{mn}}{\partial F_r} G w_{mn}^0 + \lambda_{mn}^0 G \frac{\partial w_{mn}}{\partial F_r} + K \frac{\partial w_{mn}}{\partial F_r} = 0 \quad (\text{G.8})$$

And the boundary equations become:

$$bL_1 \frac{\partial w_{mn}}{\partial F_r} + L_2 w_{mn}^0 = 0 \quad \text{at } r = b$$

$$aL_1 \frac{\partial w_{mn}}{\partial F_r} - L_2 w_{mn}^0 = 0 \quad \text{at } r = a$$

The conjugate of equation (G.7) is:

$$(\bar{\lambda}_{mn}^0)^2 M \bar{w}_{mn}^0 + \bar{\lambda}_{mn}^0 G \bar{w}_{mn}^0 + K \bar{w}_{mn}^0 = 0 \quad (\text{G.9})$$

Multiplying the equation (G.9) by $\frac{\partial w_{mn}}{\partial F_r}$:

$$(\bar{\lambda}_{mn}^0)^2 \frac{\partial w_{mn}}{\partial F_r} M \bar{w}_{mn}^0 + \bar{\lambda}_{mn}^0 \frac{\partial w_{mn}}{\partial F_r} G \bar{w}_{mn}^0 + \frac{\partial w_{mn}}{\partial F_r} K \bar{w}_{mn}^0 = 0 \quad (\text{G.10})$$

Multiplying equation (G.8) by \bar{w}_{mn}^0 :

$$2\lambda_{mn}^0 \frac{\partial \lambda_{mn}}{\partial F_r} M \bar{w}_{mn}^0 w_{mn}^0 + (\lambda_{mn}^0)^2 \bar{w}_{mn}^0 M \frac{\partial w_{mn}}{\partial F_r} + \frac{\partial \lambda_{mn}}{\partial F_r} \bar{w}_{mn}^0 G w_{mn}^0 + \lambda_{mn}^0 \bar{w}_{mn}^0 G \frac{\partial w_{mn}}{\partial F_r} + \bar{w}_{mn}^0 K \frac{\partial w_{mn}}{\partial F_r} = 0 \quad (\text{G.11})$$

Subtracting (G.10) from (G.11):

$$\begin{aligned}
& 2\lambda_{mn}^0 \frac{\partial \lambda_{mn}}{\partial F_r} M \bar{w}_{mn}^0 w_{mn}^0 + (\lambda_{mn}^0)^2 \bar{w}_{mn}^0 M \frac{\partial w_{mn}}{\partial F_r} + \frac{\partial \lambda_{mn}}{\partial F_r} \bar{w}_{mn}^0 G w_{mn}^0 + \lambda_{mn}^0 \bar{w}_{mn}^0 G \frac{\partial w_{mn}}{\partial F_r} + \\
& \bar{w}_{mn}^0 K \frac{\partial w_{mn}}{\partial F_r} - (\bar{\lambda}_{mn}^0)^2 \frac{\partial w_{mn}}{\partial F_r} M \bar{w}_{mn}^0 - \bar{\lambda}_{mn}^0 \frac{\partial w_{mn}}{\partial F_r} G \bar{w}_{mn}^0 - \frac{\partial w_{mn}}{\partial F_r} K \bar{w}_{mn}^0 = 0
\end{aligned} \tag{G.12}$$

It is recognizable that:

$$\frac{\partial w_{mn}}{\partial F_r} M \bar{w}_{mn}^0 = \bar{w}_{mn}^0 M \frac{\partial w_{mn}}{\partial F_r}$$

And

$$(\bar{\lambda}_{mn}^0)^2 = (\lambda_{mn}^0)^2$$

Therefore, equation (G.12) becomes:

$$\begin{aligned}
& 2\lambda_{mn}^0 \frac{\partial \lambda_{mn}}{\partial F_r} M \bar{w}_{mn}^0 w_{mn}^0 + \frac{\partial \lambda_{mn}}{\partial F_r} \bar{w}_{mn}^0 G w_{mn}^0 + \lambda_{mn}^0 \bar{w}_{mn}^0 G \frac{\partial w_{mn}}{\partial F_r} + \bar{w}_{mn}^0 K \frac{\partial w_{mn}}{\partial F_r} - \\
& - \bar{\lambda}_{mn}^0 \frac{\partial w_{mn}}{\partial F_r} G \bar{w}_{mn}^0 - \frac{\partial w_{mn}}{\partial F_r} K \bar{w}_{mn}^0 = 0
\end{aligned} \tag{H.13}$$

And the boundary equations are:

$$bL_1 \frac{\partial w_{mn}}{\partial F_r} + L_2 w_{mn}^0 = 0 \quad \text{and} \quad L_1 w_{mn}^0 = 0 \quad \text{at} \quad r = b$$

$$aL_1 \frac{\partial w_{mn}}{\partial F_r} - L_2 w_{mn}^0 \quad \text{and} \quad L_1 w_{mn}^0 = 0 \quad \text{at} \quad r = a$$

Integrating the equation (G.13) over an area of a circular plate ($[0, 2\pi]$ and $[a, b]$), and considering the boundary equations result in:

$$4\pi i \omega_{mn} \rho h (\omega_{mn} \pm n\Omega) \frac{\partial \lambda_{mn}}{\partial F_r} \int_a^b R_m^2(r) r dr - \omega_{mn} \left(R_m(b) \frac{\partial R_m(b)}{\partial r} - R_m(a) \frac{\partial R_m(a)}{\partial r} \right) = 0 \quad (\text{G.14})$$

Note that $\lambda_{mn} = \sigma_{mn} + i\omega_{mn}$. For a free spinning disk, the real part of eigenvalues is zero, therefore, $\lambda_{mn}^0 = i\omega_{mn}$

Rearranging the equation (G.14):

$$\frac{\partial \lambda_{mn}}{\partial F_r} = - \frac{i \left(R_m(b) \frac{\partial R_m(b)}{\partial r} - R_m(a) \frac{\partial R_m(a)}{\partial r} \right)}{4\pi \omega_{mn} \rho h (\omega_{mn} \pm n\Omega) \int_a^b R_m^2(r) r dr} \quad (\text{H.15})$$

Considering always $a < b$, then for $R_m(r)$ which is a combination of Bessel functions $J_m(r)$ and $I_m(r)$ (equation G.5), the following expression is hold:

$$R_m(b) \frac{\partial R_m(b)}{\partial r} > R_m(a) \frac{\partial R_m(a)}{\partial r} \quad (\text{G.16})$$

$$\text{And } \int_a^b R_m^2(r) r dr > 0$$

For forward waves and backward waves ($\omega_{mn} \pm n\Omega > 0$), equation (G.15) is negative, therefore the change in λ_{mn} is negative. It means that the application of F_r decreases the eigenvalues of forward and backward waves. For reflected waves ($\omega_{mn} \pm n\Omega < 0$), equation (G.15) is positive, therefore the change in λ_{mn} is positive. It means that the application of F_r increases the eigenvalues of reflected waves. The expression (G.15) does not hold when $\omega_{mn} \pm n\Omega = 0$. In other word the equation (G.15) is not true at critical speeds.

Effect of Tangential Load

The boundary equations change to:

$$b^2 L_1 w + F_t L_3 w = 0 \quad \text{at } r = b$$

$$2a^3 L_1 w - (a + b) F_t L_3 w + (b - a) F_t L_4 w = 0 \quad \text{at } r = a$$

Using the same procedure as for the radial loads, for a free spinning disk ($F_t = 0$)[23]

$$(\lambda_{mn}^0)^2 M w_{mn}^0 + \lambda_{mn}^0 G w_{mn}^0 + K w_{mn}^0 = 0 \quad (\text{G.17})$$

The boundary equations become (substitute $F_r = 0$ in the boundary equations)

$$L_1 w_{mn}^0 = 0 \quad \text{at } r = a \text{ and } r = b$$

Taking the derivative of equation (G.17) with respect to F_t [23]:

$$2\lambda_{mn}^0 \frac{\partial \lambda_{mn}}{\partial F_t} M w_{mn}^0 + (\lambda_{mn}^0)^2 M \frac{\partial w_{mn}}{\partial F_t} + \frac{\partial \lambda_{mn}}{\partial F_t} G w_{mn}^0 + \lambda_{mn}^0 G \frac{\partial w_{mn}}{\partial F_t} + K \frac{\partial w_{mn}}{\partial F_t} = 0 \quad (\text{G.18})$$

And the boundary equations become:

$$b^2 L_1 \frac{\partial w_{mn}}{\partial F_t} + L_3 w_{mn}^0 = 0 \quad \text{at } r = b$$

$$2a^3 L_1 \frac{\partial w_{mn}}{\partial F_t} - (a + b) L_3 w_{mn}^0 + (b - a) L_4 w_{mn}^0 = 0 \quad \text{at } r = a$$

Multiplying the conjugate of equation (G.17) by the $\frac{\partial w_{mn}}{\partial F_t}$:

$$(\bar{\lambda}_{mn}^0)^2 \frac{\partial w_{mn}}{\partial F_t} M \bar{w}_{mn}^0 + \bar{\lambda}_{mn}^0 \frac{\partial w_{mn}}{\partial F_t} G \bar{w}_{mn}^0 + \frac{\partial w_{mn}}{\partial F_t} K \bar{w}_{mn}^0 = 0 \quad (\text{G.19})$$

Multiplying equation (G.18) by \bar{w}_{mn}^0 :

$$2\lambda_{mn}^0 \frac{\partial \lambda_{mn}}{\partial F_t} \bar{w}_{mn}^0 M w_{mn}^0 + (\lambda_{mn}^0)^2 \bar{w}_{mn}^0 M \frac{\partial w_{mn}}{\partial F_t} + \frac{\partial \lambda_{mn}}{\partial F_t} \bar{w}_{mn}^0 G w_{mn}^0 + \lambda_{mn}^0 \bar{w}_{mn}^0 G \frac{\partial w_{mn}}{\partial F_t} + \bar{w}_{mn}^0 K \frac{\partial w_{mn}}{\partial F_t} = 0 \quad (\text{G.20})$$

Subtract Equation (G.19) from Equation (G.20), results in:

$$2\lambda_{mn}^0 \frac{\partial \lambda_{mn}}{\partial F_t} \bar{w}_{mn}^0 M w_{mn}^0 + \frac{\partial \lambda_{mn}}{\partial F_t} \bar{w}_{mn}^0 G w_{mn}^0 + \lambda_{mn}^0 \bar{w}_{mn}^0 G \frac{\partial w_{mn}}{\partial F_t} + \bar{w}_{mn}^0 K \frac{\partial w_{mn}}{\partial F_t} - \bar{\lambda}_{mn}^0 \frac{\partial w_{mn}}{\partial F_t} G \bar{w}_{mn}^0 - \frac{\partial w_{mn}}{\partial F_t} K \bar{w}_{mn}^0 = 0 \quad (\text{G.21})$$

Note that

$$(\lambda_{mn}^0)^2 \bar{w}_{mn}^0 M \frac{\partial w_{mn}}{\partial F_t} = (\bar{\lambda}_{mn}^0)^2 \frac{\partial w_{mn}}{\partial F_t} M \bar{w}_{mn}^0$$

Integration of Equation (G.21) over an area of a disk, and considering the boundary equations, result in:

$$4\pi i \omega_{mn} \rho h (\omega_{mn} \pm n\Omega) \frac{\partial \lambda_{mn}}{\partial F_t} \int_a^b R_m^2(r) r dr - n \omega_{mn} (bR_m(b) - aR_m(a)) = 0 \quad (\text{G.22})$$

Rearranging the equation (G.22):

$$\frac{\partial \lambda_{mn}}{\partial F_t} = - \frac{ni(bR_m(b) - aR_m(a))}{4\pi \rho h (\omega_{mn} \pm n\Omega) \int_a^b R_m^2(r) r dr} \quad (\text{G.23})$$

We can assume that for $a < b$:

$$bR_m(b) - aR_m(a) > 0 \quad (\text{G.24})$$

And $\int_a^b R_m^2(r)rdr > 0$

Then for forward waves and backward waves ($\omega_{mn} \pm n\Omega > 0$), equation (G.23) is negative, therefore the change in λ_{mn} is negative. It means that the application of F_t decreases the eigenvalues of forward and backward waves. For reflected waves ($\omega_{mn} \pm n\Omega < 0$), equation (G.23) is positive, therefore the change in λ_{mn} is positive. It means that the application of F_t increases the eigenvalues of reflected waves. The expression (G.23) does not hold when $\omega_{mn} \pm n\Omega = 0$. In other word the equation (G.23) is not true at critical speeds.

In addition, for $n = 0$ (modes with no nodal diameter), equation (G.23) becomes:

$$\frac{\partial \lambda_{mn}}{\partial F_t} = 0 \quad (G.25)$$

Therefore, tangential loads do not have effect on modes with no nodal diameter.

Equations (G.15) and (G.23) indicate that, for a free spinning splined disk, the derivative of eigenvalues with respect to the radial and tangential loads is purely imaginary. Therefore, in-plane edge loads only affect the imaginary part of eigenvalues. In other word, the effect of in-plane edge loads on the real part of eigenvalues is zero. Since the real part of eigenvalues for a splined disk, subjected to in-plane loads is zero, it can be concluded that in-plane edge loads, do not induce any instability to the disk.

Appendix H

Idling Response of Different Blade Sizes

Figure H.1 Idling Response of Disk 17-6-0.040

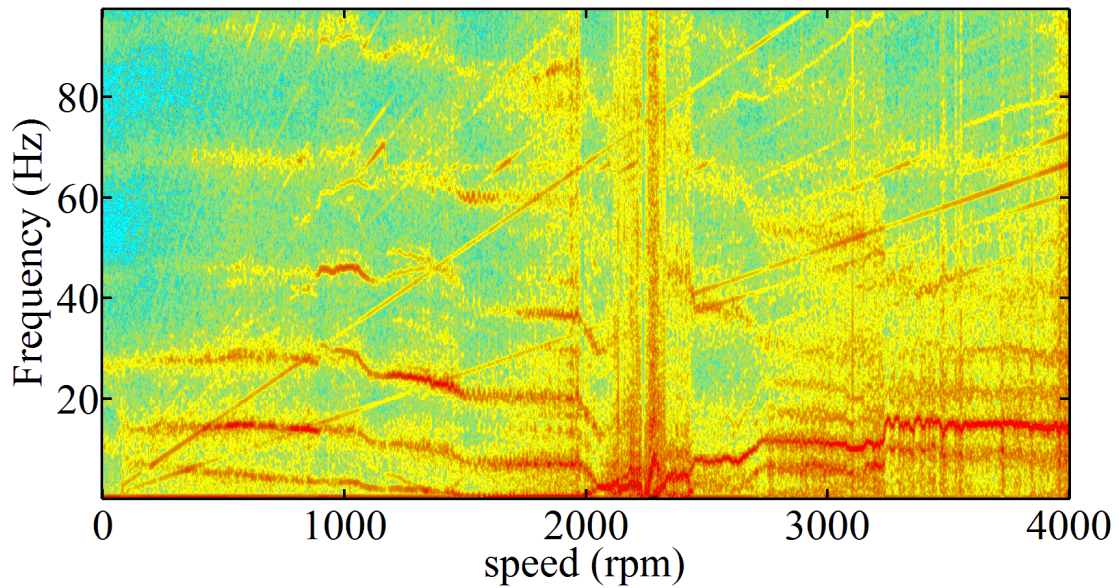
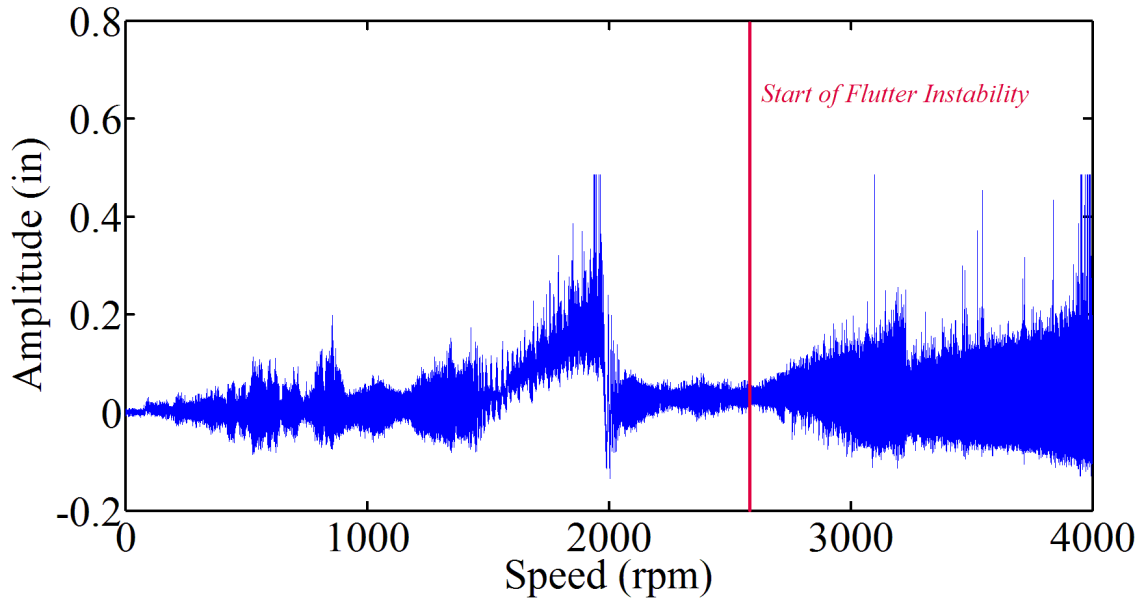


Figure H.2 Idling Response of Disk 20-6-0.080

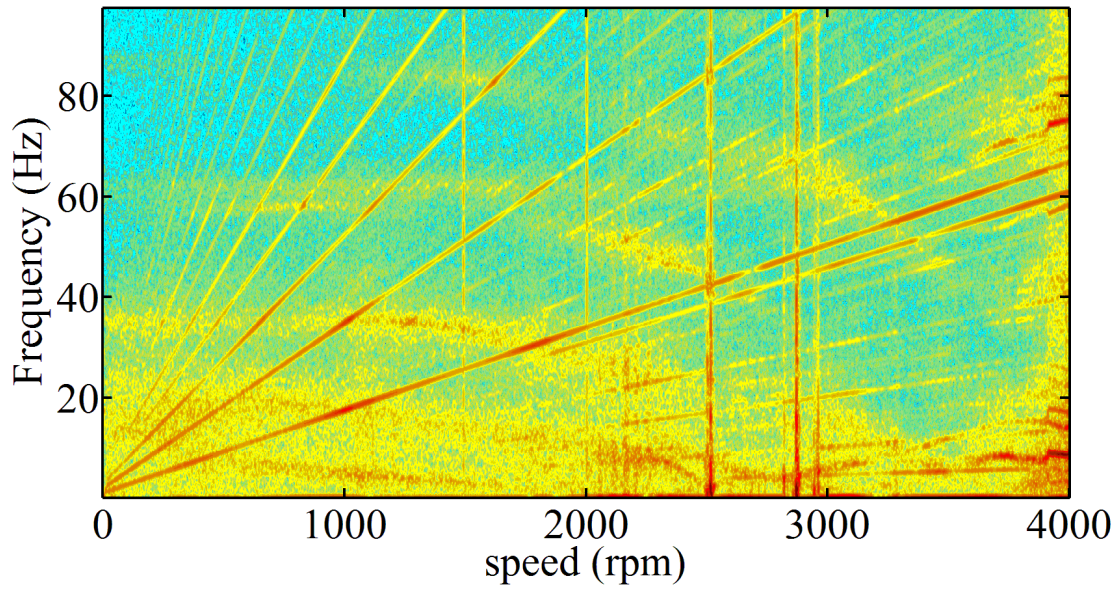
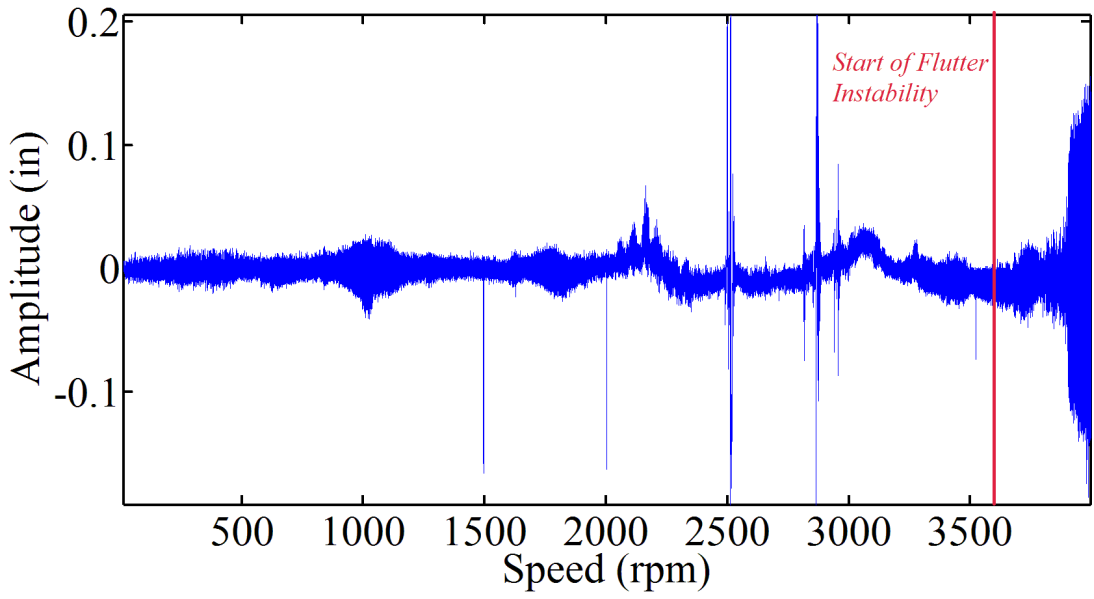


Figure H.3 Idling Response of Blade 30-8-0.125

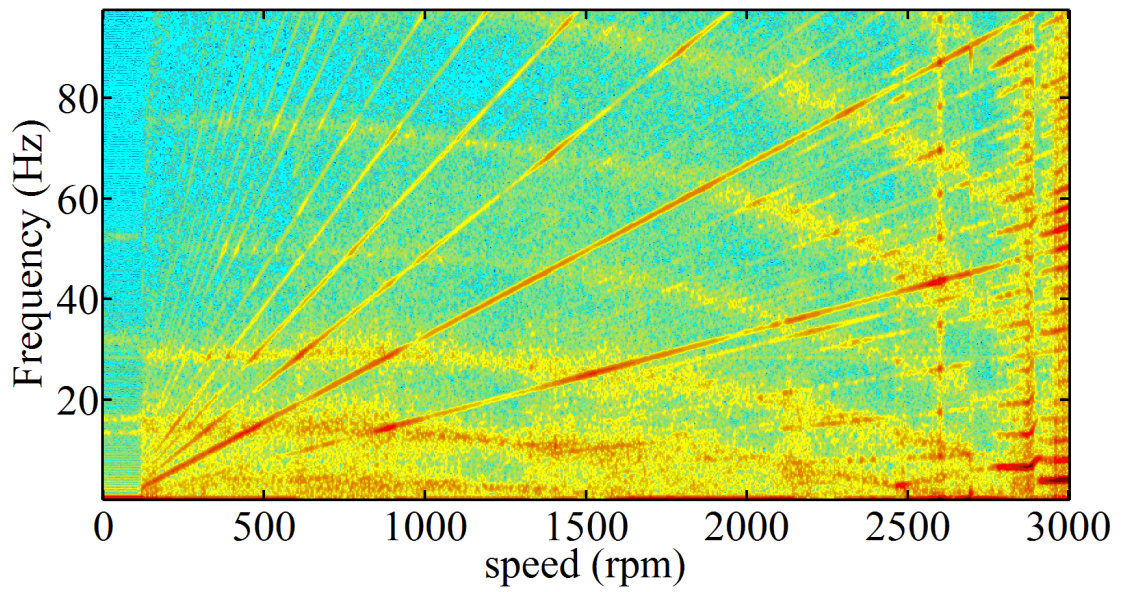
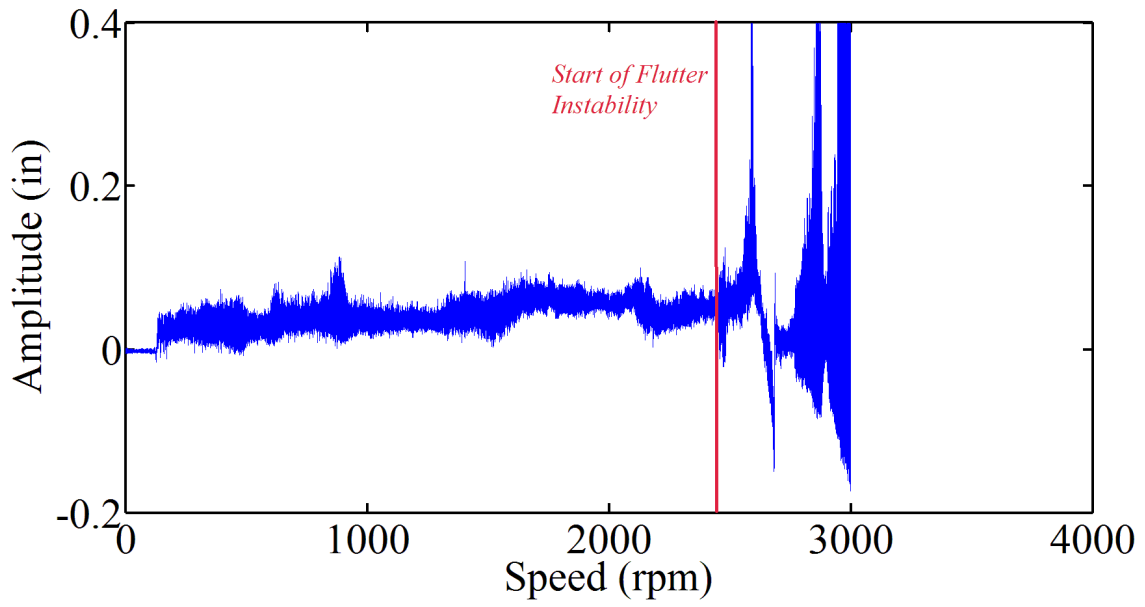
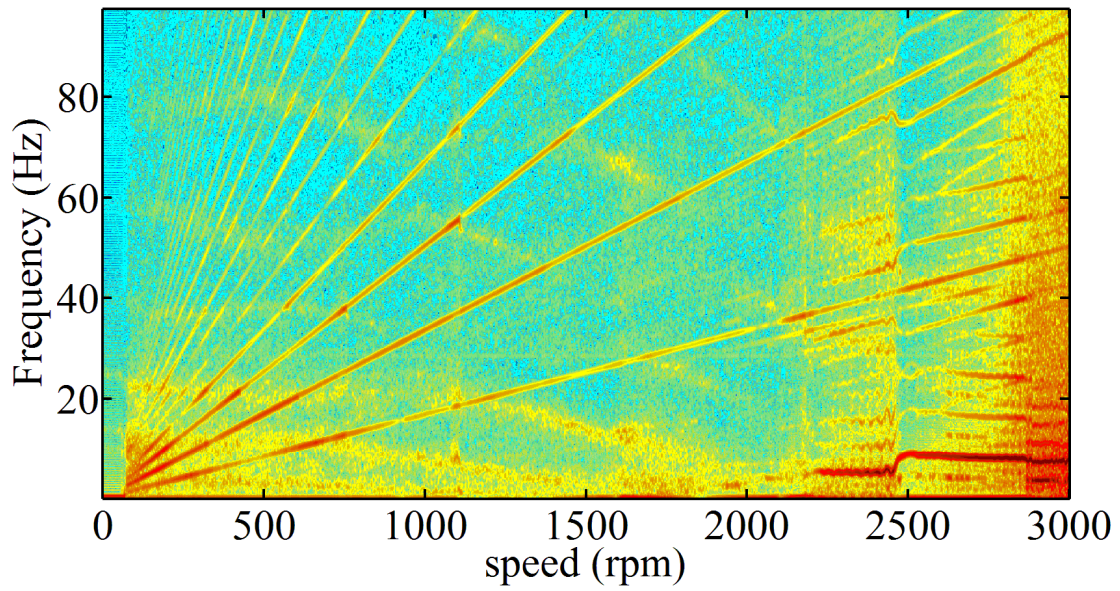
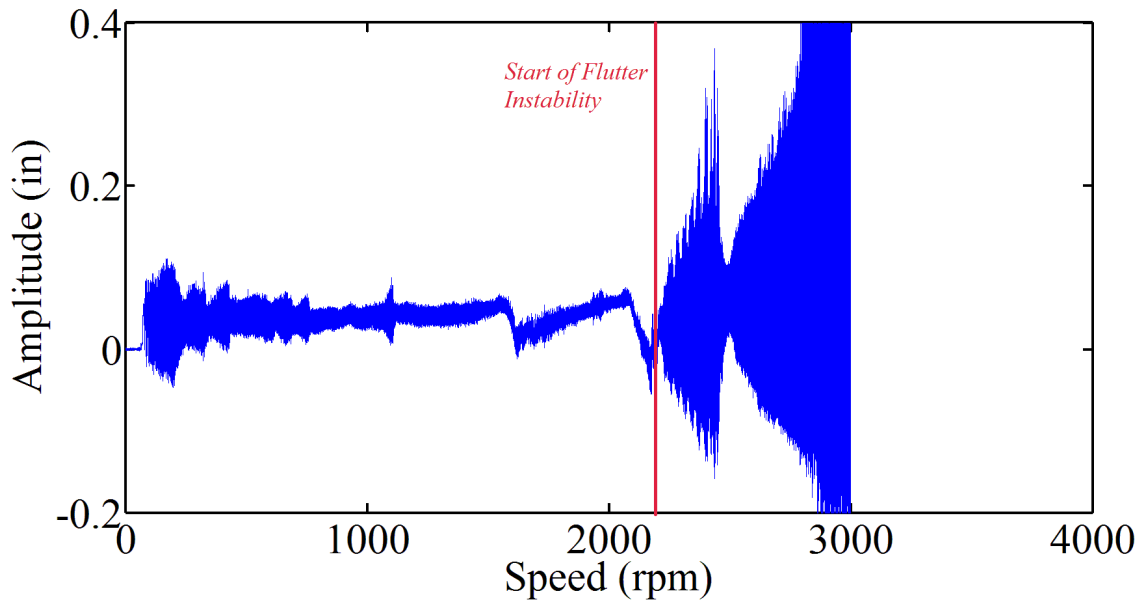


Figure H.4 Idling Response of Blade 34-8-0.145



Appendix I

Mathematical Calculation of Non-Dimensional Equation of Motion

Non-dimensional parameters are introduced as [22]:

$$R = \frac{r}{b}, \quad W = \frac{w}{b}, \quad \tau = Tt$$

$$\text{Where } T = \sqrt{\frac{D}{\rho hb^4}}$$

Based on the introduced parameters:

$$\Omega^* = \frac{\Omega}{T}$$

$$\frac{\partial w}{\partial t} = \frac{\partial(bW)}{\partial(\tau/T)} = Tb \frac{\partial W}{\partial \tau}, \quad \frac{\partial^2 w}{\partial t^2} = T^2 b \frac{\partial^2 W}{\partial \tau^2}, \quad \frac{\partial^2 w}{\partial t \partial \theta} = Tb \frac{\partial^2 W}{\partial \tau \partial \theta}, \quad \nabla^4 w = \frac{1}{b^3} \nabla^4 W$$

$$\frac{\partial^2 w}{\partial \theta^2} = b \frac{\partial^2 W}{\partial \theta^2}, \quad \frac{\partial w}{\partial r} = \frac{\partial(bW)}{\partial(bR)} = \frac{\partial W}{\partial R}, \quad \frac{\partial^2 w}{\partial r^2} = \frac{\partial}{\partial(bR)} \frac{\partial w}{\partial r} = \frac{1}{b} \frac{\partial^2 W}{\partial R^2}$$

By substitution of, σ_r and σ_θ into equation of motion, we get:

$$\rho h (w_{,tt} + 2\Omega w_{,t\theta} + \Omega^2 w_{,\theta\theta}) + D \nabla^4 w - \frac{h}{r} \rho \Omega^2 (w_{,r} (C_1 r + \frac{C_2}{r} + C_3 r^3))_{,r} - h \rho \Omega^2 \left(\frac{C_1}{r^2} - \frac{C_2}{r^4} + C_4 \right) w_{,\theta\theta} = f \quad (\text{I.1})$$

By simplification of equation (I.1) the equation can be written in the form of:

$$\rho h (w_{,tt} + 2\Omega w_{,t\theta} + \Omega^2 w_{,\theta\theta}) + D \nabla^4 w - h \rho \Omega^2 \left(w_{,rr} \left(C_1 + \frac{C_2}{r^2} + C_3 r^2 \right) + w_{,r} \left(\frac{C_1}{r} - \frac{C_2}{r^3} + 3C_3 r \right) \right) - h \rho \Omega^2 \left(\frac{C_1}{r^2} - \frac{C_2}{r^4} + C_4 \right) w_{,\theta\theta} = f \quad (\text{I.2})$$

Here we substitute the non-dimensional parameters into equation (I.2):

$$\rho h T^2 b (W_{,\tau\tau} + 2\Omega^* W_{,\tau\theta} + \Omega^{*2} W_{,\theta\theta}) + \frac{D}{b^3} \nabla^4 W -$$

$$\rho h T^2 \Omega^{*2} \left[\frac{W_{,RR}}{b} \left(C_1 + \frac{C_2}{R^2 b^2} + C_3 R^2 b^2 \right) + W_{,R} \left(\frac{C_1}{Rb} - \frac{C_2}{R^3 b^3} + 3C_3 Rb \right) \right] - \rho h T^2 \Omega^{*2} b \left(\frac{C_1}{R^2 b^2} - \frac{C_2}{R^4 b^4} + C_4 \right) W_{,\theta\theta} = f \quad (I.3)$$

By dividing both side of equation (I.3), the equation may be written as

$$\begin{aligned} & (W_{,\tau\tau} + 2\Omega^{*2} W_{,\tau\theta} + \Omega^{*2} W_{,\theta\theta}) + \frac{D}{\rho h T^2 b^4} \nabla^4 W - \\ & \frac{\rho \Omega^{*2}}{\rho b} \left[\frac{W_{,RR}}{b} \left(C_1 + \frac{C_2}{R^2 b^2} + C_3 R^2 b^2 \right) + W_{,R} \left(\frac{C_1}{Rb} - \frac{C_2}{R^3 b^3} + 3C_3 Rb \right) \right] - \\ & \frac{\rho \Omega^{*2}}{\rho} \left(\frac{C_1}{R^2 b^2} - \frac{C_2}{R^4 b^4} + C_4 \right) W_{,\theta\theta} = \frac{f}{\rho h T^2 b} \end{aligned} \quad (I.4)$$

If we put $\frac{D}{\rho h T^2 b^4} = 1$ we get:

$$T = \sqrt{\frac{D}{\rho h b^4}} \quad (I.5)$$

By substituting T in equation (I.4) the equation can be written as

$$\begin{aligned} & W_{,\tau\tau} + 2\Omega^{*2} W_{,\tau\theta} + \Omega^{*2} W_{,\theta\theta} + \nabla^4 W - \frac{\Omega^{*2}}{b^2} \left(C_1 + \frac{C_2}{R^2 b^2} + C_3 R^2 b^2 \right) W_{,RR} - \frac{\Omega^{*2}}{b} \left(\frac{C_1}{Rb} - \frac{C_2}{R^3 b^3} + \right. \\ & \left. 3C_3 Rb \right) W_{,R} - \frac{\Omega^{*2}}{1} \left(\frac{C_1}{R^2 b^2} - \frac{C_2}{R^4 b^4} + C_4 \right) W_{,\theta\theta} = \frac{fb^3}{D} \end{aligned} \quad (I.6)$$

This equation may be written in the form of:

$$W_{,\tau\tau} + 2\Omega^{*2} W_{,\tau\theta} + \Omega^{*2} W_{,\theta\theta} + \nabla^4 W - \frac{\Omega^{*2}}{b^2} (C_{rr} W_{,RR} + C_r W_{,R} + C_{\theta\theta} W_{,\theta\theta}) = \frac{fb^3}{D} \quad (I.7)$$

Where

$$\begin{aligned} C_{rr} &= C_1 + \frac{C_2}{R^2 b^2} + C_3 R^2 b^2 \\ C_r &= b \left(\frac{C_1}{Rb} - \frac{C_2}{R^3 b^3} + 3C_3 Rb \right) \\ C_{\theta\theta} &= b^2 \left(\frac{C_1}{R^2 b^2} - \frac{C_2}{R^4 b^4} + C_4 \right) \end{aligned}$$